

UNIVERSIDADE FEDERAL DO RIO GRANDE DO NORTE

Programa de Pós-Graduação em Neurociências



**THE INFLUENCE OF INTERHEMISPHERIC CONNECTIONS ON  
SPIKING, ASSEMBLY AND LFP ACTIVITIES, AND THEIR PHASE  
RELATIONSHIP DURING FIGURE-GROUND STIMULATION IN  
PRIMARY VISUAL CORTEX.**

**SERGIO ANDRÉS CONDE OCAZIONEZ**

**Natal, 2014**

UNIVERSIDADE FEDERAL DO RIO GRANDE DO NORTE

**Programa de Pós-Graduação em Neurociências**

**THE INFLUENCE OF INTERHEMISPHERIC CONNECTIONS ON SPIKING,  
ASSEMBLY AND LFP ACTIVITIES, AND THEIR PHASE RELATIONSHIP  
DURING FIGURE-GROUND STIMULATION IN PRIMARY VISUAL CORTEX.**

**SERGIO ANDRÉS CONDE OCAZIONEZ**

Trabalho apresentado ao programa de Pós-Graduação em Neurociências da Universidade Federal do Rio Grande do Norte como requisito para a obtenção do grau de

**DOUTOR EM NEUROSCIÊNCIAS**

**Aprovada em: 31.03.2014**

**Banca examinadora:**

ADRIANO BRETANHA LOPES TORT

JEAN CHRISTOPHE HOUZEL – UFRJ

JEROME PAUL ARMAND LAURENT BARON – UFMG

KERSTIN ERIKA SCHMIDT

SERGIO TULIO NEUENSCHWANDER MACIEL

**Natal, 2014**

## **Acknowledgments**

This work would be impossible without the enormous support of my entire family. Thank you for always be there!

To Prof. Kerstin Schmidt, thank you for the lessons, patience and for having embraced and care this project as her own.

To Beatriz Couto, thank you for coming into this crazy boat with me.

To all my friends, especially to Vitor Santos and Rodrigo Pavão, thank you for all coffees and beers trying to put the puzzle pieces in their place.

Thank you all!

## **Summary**

Abbreviation List.....	4
Resumo.....	5
Abstract.....	7
1. Introduction.....	9
1.1. The Primary Visual Cortex.....	12
1.1.1. Lateral Intrinsic Connections.....	15
1.1.2. Visual Callosal Connections .....	17
1.2. Contextual Stimulation.....	19
2. Working Hypothesis.....	24
3. Objectives .....	25
4. Materials and Methods.....	26
4.1. Anesthesia and Physiological Monitoring.....	26
4.2. Recording Area Identification.....	26
4.3. Electrode Implantation .....	27
4.4. Stimuli.....	28
4.5. Cooling Procedure .....	29
4.6. Data Recording .....	30
4.7. Data Analysis .....	31
4.7.1. Orientation and Direction Tuning of Multiunit Activity .....	31
4.7.2. Firing Rates and Power Spectral Density .....	32
4.7.3. Assembly Detection .....	34
4.7.4. Phase Locking.....	38
5. Results.....	41
5.1. Recording Site Characterization .....	41
5.2. Raw Responses.....	44
5.3. Segmentation and Cooling Indices for Firing rates and LFPs.....	48
5.4. Assembly Detection and Characterization.....	53
5.5. Segmentation and Cooling Indices for Assemblies.....	56
5.6. Phase Locking .....	59
5.6.1. Single Cell and Assembly Phase Locking with Grating Stimulation .....	59

5.6.2. Single Cell and Assembly Phase Locking with Natural Scene Stimulation.....	60
5.7. Coherence Variation during the Deactivation of IHCs .....	63
5.8. Summary of Results.....	66
5.8.1. From Individual Recording Sites .....	66
5.8.2. From Population Level.....	67
6. Discussion.....	68
6.1. Methodological discussion.....	68
6.1.1. About Visual Stimulation .....	68
6.1.2. About the cooling technique.....	69
6.2. About Figure-Ground Segmentation.....	70
6.3. About the Influence of Interhemispheric Connections on Raw Responses .....	71
6.4. About the Influence of Interhemispheric Connections on Figure-Ground Segmentation .....	72
6.4.1. Spike rates .....	72
6.4.2. LFP power.....	73
6.4.3. Assemblies and Phase Locking .....	76
7. Summary and Conclusion.....	80
8. Supplementary.....	82
9. References.....	83

## **Abbreviation List**

**CI:** Cooling Index

**CRF:** Classical Receptive Field

**DI:** Direction Index

**HG:** High Gamma

**IHCs:** Interhemispheric Connections

**JRF:** Joint Receptive Field

**LFP:** Local Field Potential

**LG:** Low Gamma

**OI:** Orientation Index

**PSD:** Power Spectrum Density

**RS:** Recording Sites

**SI:** Segmentation Index

**WF:** Whole-Field

# **A influência das conexões inter-hemisféricas nas atividades de disparo, de assembleias e de potencial de campo, e sua relação de fase durante a estimulação figura-fundo do córtex visual primário.**

## **Resumo**

Desde os descobrimentos pioneiros de Hubel e Wiesel acumulou-se uma vasta literatura descrevendo as respostas neurais do córtex visual primário (V1) a diferentes estímulos visuais. Estes estímulos consistem principalmente em barras em movimento, pontos ou grades, que são úteis para explorar as respostas dentro do campo receptivo clássico (CRF do inglês *classical receptive field*) a características básicas dos estímulos visuais como a orientação, direção de movimento, contraste, entre outras. Entretanto, nas últimas duas décadas, tornou-se cada vez mais evidente que a atividade de neurônios em V1 pode ser modulada por estímulos fora do CRF. Desta forma, áreas visuais primárias poderiam estar envolvidas em funções visuais mais complexas como, por exemplo, a separação de um objeto ou figura do seu fundo (segregação figura-fundo) e assume-se que as conexões intrínsecas de longo alcance em V1, assim como as conexões de áreas visuais superiores, estão ativamente envolvidas neste processo. Sua possível função foi inferida a partir da análise das variações das respostas induzidas por um estímulo localizado fora do CRF de neurônios individuais. Mesmo sendo muito provável que estas conexões tenham também um impacto tanto na atividade conjunta de neurônios envolvidos no processamento da figura quanto no potencial de campo, estas questões permanecem pouco estudadas.

Visando examinar a modulação do contexto visual nessas atividades, coletamos potenciais de ação e potenciais de campo em paralelo de até 48 eletrodos implantados na área visual primária de gatos anestesiados. Estimulamos com grades compostas e cenas naturais, focando-nos na atividade de neurônios cujo CRF estava situado na figura. Da mesma forma, visando examinar a influência das conexões laterais, o sinal proveniente da área visual isotópica e contralateral foi removido através da desativação reversível por resfriamento. Fizemos isso devido a: *i*) as conexões laterais intrínsecas não podem ser facilmente manipuladas sem afetar diretamente os sinais que estão sendo medidos, *ii*) as conexões inter-hemisféricas compartilham as principais características anatômicas com a rede lateral intrínseca e podem ser vistas como uma continuação funcional das mesmas entre os dois hemisférios e *iii*) o resfriamento desativa as conexões de forma causal e reversível, silenciando temporariamente seu sinal, permitindo conclusões diretas a respeito da sua contribuição. Nossos resultados demonstram que o mecanismo de segmentação figura-fundo se reflete nas taxas de disparo de neurônios individuais, assim como na potência do potencial de campo e na relação entre sua fase e os padrões de disparo produzidos pela população. Além disso, as conexões “laterais” inter-hemisféricas modulam estas variáveis dependendo da estimulação feita fora do CRF. Observamos também uma influência deste

círculo lateral na coerência entre potenciais de campo entre eletrodos distantes. Em conclusão, nossos resultados dão suporte à ideia de um mecanismo complexo de segmentação figura-fundo atuando desde as áreas visuais primárias em diferentes escalas de frequência. Esse mecanismo parece envolver grupos de neurônios ativos sincronicamente e dependentes da fase do potencial de campo. Nossos resultados também são compatíveis com a hipótese que conexões laterais de longo alcance também fazem parte deste mecanismo.

# **The influence of interhemispheric connections on spiking, assembly and LFP activities, and their phase relationship during figure-ground segmentation in primary visual cortex.**

## **Abstract**

Since Hubel and Wiesel's pioneer finding a vast body of literature has accumulated describing neuronal responses in the primary visual cortex (V1) to different visual stimuli. These stimuli mainly consisted of moving bars, dots or gratings which served to explore the responses to basic visual features such as orientation, direction of motion or contrast, among others, within a classical receptive field (CRF). However, in the last two decades it became increasingly evident that the activity of V1 neurons can be modulated by stimulation outside their CRF. Thus, early visual areas might be already involved in more complex visual tasks like, for example, the segmentation of an object or a figure from its (back)-ground. It is assumed that intrinsic long-range horizontal connections within V1 as well as feedback connections from higher visual areas are actively involved in the figure-ground segmentation process. Their possible role has been inferred from the analysis of the spike rate variations induced by stimuli placed outside the CRF of single neurons. Although it is very likely that those connections also have an impact on the joined activity of neurons involved in processing the figure and on their local field potentials (LFP), these issues remain understudied.

In order to examine the context-dependent modulation of those activities, we recorded spikes and LFPs in parallel from up to 48 electrodes in the primary visual cortex of anesthetized cats. We stimulated with composite grating and natural scene stimuli focusing on populations of neurons whose CRFs were situated on the foreground figure. In addition, in order to examine the influence of horizontal connections we removed the interhemispheric input of the isotopic contralateral visual areas by means of reversible cooling deactivation. We did so because i) the intrinsic horizontal connections cannot be easily manipulated without directly affecting the measured signals, ii) because interhemispheric connections share the major anatomical features with the intrinsic lateral network and can be seen as a functional continuation of the latter across the two hemispheres and iii) because cooling causally and reversibly deactivates input connections by temporarily silencing the sending neurons and thus enables direct conclusions on their contribution. Our results demonstrate that the figure-ground segmentation mechanism is reflected in the spike rate of single neurons, as well as in their LFP power and its phase-relationship to the spike patterns produced by the population. In addition "lateral" interhemispheric connections modulate spike rates and LFP power depending on the stimulation of the neurons' CRF surround. Further, we observe an influence of this lateral circuit on field-field coherences between remote recording sites. In conclusion, our findings

support the idea of complex figure-ground segmentation mechanism acting already in early visual areas on different time scales. This mechanism seems to involve groups of neurons firing synchronously and dependent on the LFP's phase. Our results are also compatible with the hypothesis that long-range lateral connections contribute to that mechanism.

## 1. Introduction

The visual system is a complex processing center within the central nervous system. It has to encode information about many image features such as shape, size, color or movement. This remarkable capability arises from a mixture of structured anatomy and complex signal processing.

All signal processing starts in the retina, the only peripheral part of the central nervous system and neural portion of the eye. Here, an orderly neural network formed by different kinds of cells (i.e. photoreceptors, bipolar cells, ganglion cells, horizontal cells and amacrine cells) converts the electrical signals generated by photoreceptors into action potentials that will be conducted through ganglion cells axons to the brain (Purves, 2004). The intraretinal circuitry is, by itself, already a highly efficient processing center, sending to the brain encoded information about color, contrast and light changes among many other features. After the signal has left the retina, it travels to the optic chiasm by the ganglion cells axons forming the optic nerve; there, a part of these axons (about 60% in cats and primates) cross the chiasm to the contralateral side of the brain and the remaining part continues ipsilaterally.

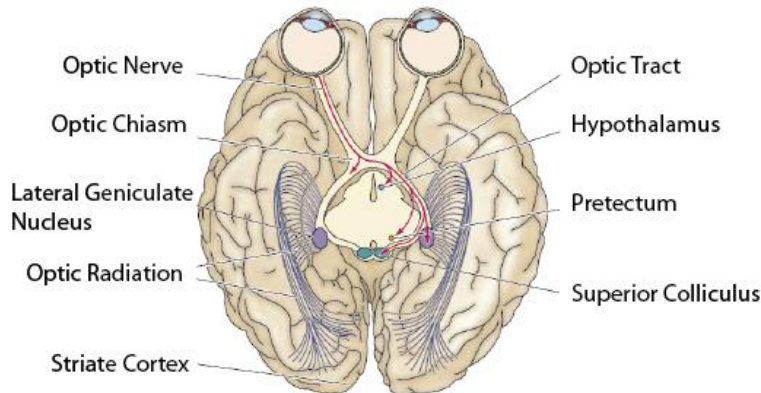


**Figure 1. Basic connectivity of the visual system from retina to primary visual cortex.**  
[Modified from (Purves, 2004)]

Once the optic nerve is divided, the new set of ganglion cells axons (at this point, axons from both eyes) form a new structure called the optic tract. This tract projects to many other subcortical structures like the pretectum, the Edinger-Westphal nucleus, suprachiasmatic nucleus or the superior colliculus where information involved in functions like the pupillary light reflex, oculomotor functions, night/day cycle and movement of eyes and head, are respectively processed. However, the major part of the optic tract projects to

## 1. Introduction

the dorsal lateral geniculate nucleus (LGN) of the thalamus, which executes relay functions between the optic tract and the primary visual cortex (Figure 1).

Neurons in primary visual cortex (striate cortex or V1) form a well-organized network and are activated according to basic features of simple stimuli (i.e. moving bars with a certain orientation and direction of motion. For details see Section 1.1). These architectural and functional characteristics led researchers to propose that V1 participates in what is considered as low level processing which includes border detection or contour grouping. However whether V1 contributes in more complex visual processing is still an open debate. The brain's ability to perceptually separate an object from its background, for example, is a manifold studied mechanism (figure-ground segmentation) where the role of V1 is still not clear. Some features of the connectivity, like the intrinsic long-range horizontal connections, or feedback connections from higher visual areas point out that indeed V1 could play an important role on figure-ground segmentation (see Section 1.2).

In order to experimentally address the figure-ground segmentation paradigm, researchers train animals (mainly cats and monkeys) to direct the gaze to a specific area on the monitor. The visual stimulus on this area is intentionally designed to perceptually pop out, configuring what is called *figure*. The remaining area of the monitor is considered as *background* (Figure 2). During this task, electrophysiological signals (from single cells activity to population activity) are collected with the intent of better-understand the neuronal correlates of this type of visual processing.

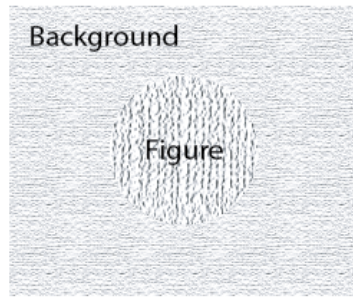


**Figure 2. Example of a figure-ground stimulus.** The texture of the central circle (figure) was modified to stand out from the background.

Moreover, the visual pathway architecture from the retina to V1 evidences a brain lateralization of visual processing. This implies that each brain hemisphere processes the contralateral part of the visual field (hemifields). Despite this lateralization, we perceive the world as a single integrated image rather than two separated ones.

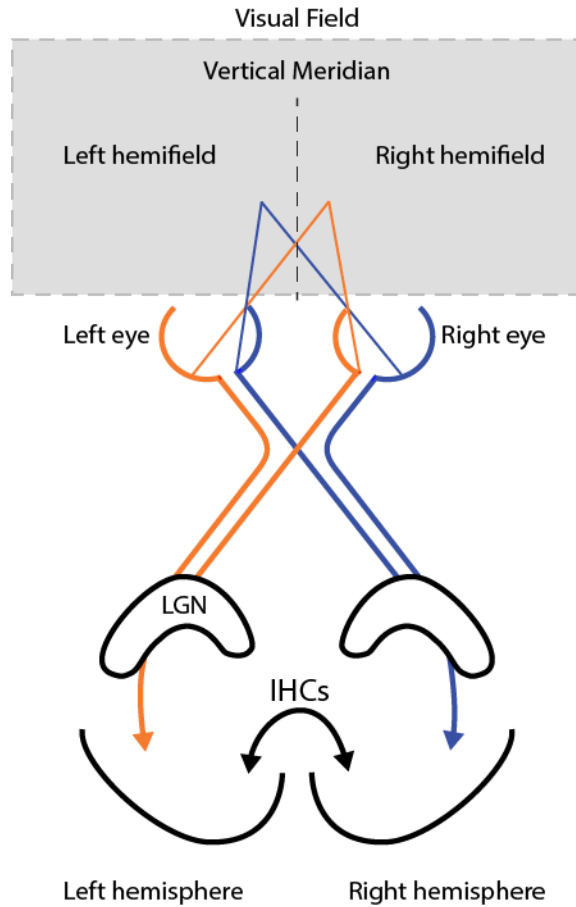


**Figure 3. Lateralization of visual pathways.** The visual field is divided in two hemifields. The lateral geniculate nucleus (LGN) receives visual input from the contralateral hemifield and transmit it to the primary visual cortex in the ipsilateral brain hemisphere. The interhemispheric connections (IHCs) integrate the information in both hemispheres.

A special kind of connections: the interhemispheric connections, process the visual stimulus located near the vertical meridian (Figure 3) and allows the integration of the hemifields, synchronize the hemispheres, between other important functions. These connections link mainly areas at V1 level, and have a strong functional and anatomical similarity with horizontal intrinsic network. (For details see Sections 1.1.1 and for review Schmidt, 2013).

Intuitively, most situations in which the brain deals with figure-ground segmentation imply to direct the gaze straight to the figure, positioning it at least near the vertical meridian. This fact, added to the similarities between interhemispheric and intrinsic horizontal connections, raise the question of what is the role of interhemispheric connections in the figure-ground segmentation.

In this work we delineate a description of anatomical and functional features of primary visual cortex and its connectivity architecture. We focus on interhemispheric connections and discuss their contribution in visual processing on a figure-ground segmentation paradigm based on spiking and local field potential activity collected from primary visual cortex of anesthetized cats. We frame the discussion in a parallel between long-range horizontal and interhemispheric connections showing that our results are in concordance with the role of horizontal connectivity suggested in the literature, thus strengthening the similarity between the two kinds of connections.

### 1.1. The Primary Visual Cortex

The primary visual cortex corresponds to Brodman's area 17 (and 18 in the cat). It is located in the posterior pole of the occipital cortex and constitutes the first cortical stage in visual processing.

The activation of a V1 neuron by direct stimulation is the result of stimulating a spatially restricted area of the visual field. Light changes in different such areas activate different neurons across V1. This portion of the visual field is defined as a classical receptive field of a neuron (CRF) and its main features were well-described by an extensive work of Hubel and Wiesel in the middle of the last century (see Hubel and Wiesel (1959; 1960; 1962; 1963; 1965; 1968)).

One of the main functional features of V1 neurons, described by the same authors, is their preference for distinct stimulus moieties. For example, in an experiment stimulating a CRF of a given neuron using moving contrast borders, i.e. bars, there is a specific bar orientation, size and/or movement direction (preferred parameters) that produces the optimal response from that neuron.

Topographically, V1 neurons are arranged in a columnar manner where neurons of the same column share the same properties. Different columns can be defined regarding different response preferences, i.e. neurons in ocular dominance columns receive predominantly input from the same eye. In cat's area 17, the distance between such columns is around 900 $\mu$ m (Schmidt and Löwel, 2002). Another parameter to define columnar organization is orientation selectivity. In this case, neurons in the same column share similar orientation preferences. The transition between columns occurs in a gradual manner around a central point (pinwheel center). Applying optical imaging techniques and color-coding of the responses to each orientation it is possible to construct an orientation map of a given superficial area (Figure 4).

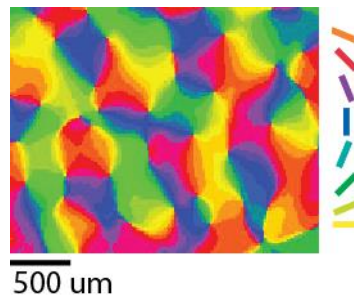


**Figure 4. Orientation column map resulting from intrinsic signal optical imaging in cat's V1.** Preferred orientation is color-coded according to the scheme on the right. [Courtesy of Dr. Kerstin Schmidt]

As a part of the neocortex, the primary visual cortex is divided in six layers defined by different cell morphology and connectivity. It exhibits three major pathways: The feed-forward connections proceeding from lateral geniculate nucleus to the layer IV, the feedback connections coming from higher visual areas and the intrinsic circuitry, which includes vertical connections from layer IV to II-III and from there to layer V; and also lateral (horizontal) connections within layers, mainly in layers II/III and V (See Section 1.1.1 and Figure 5).

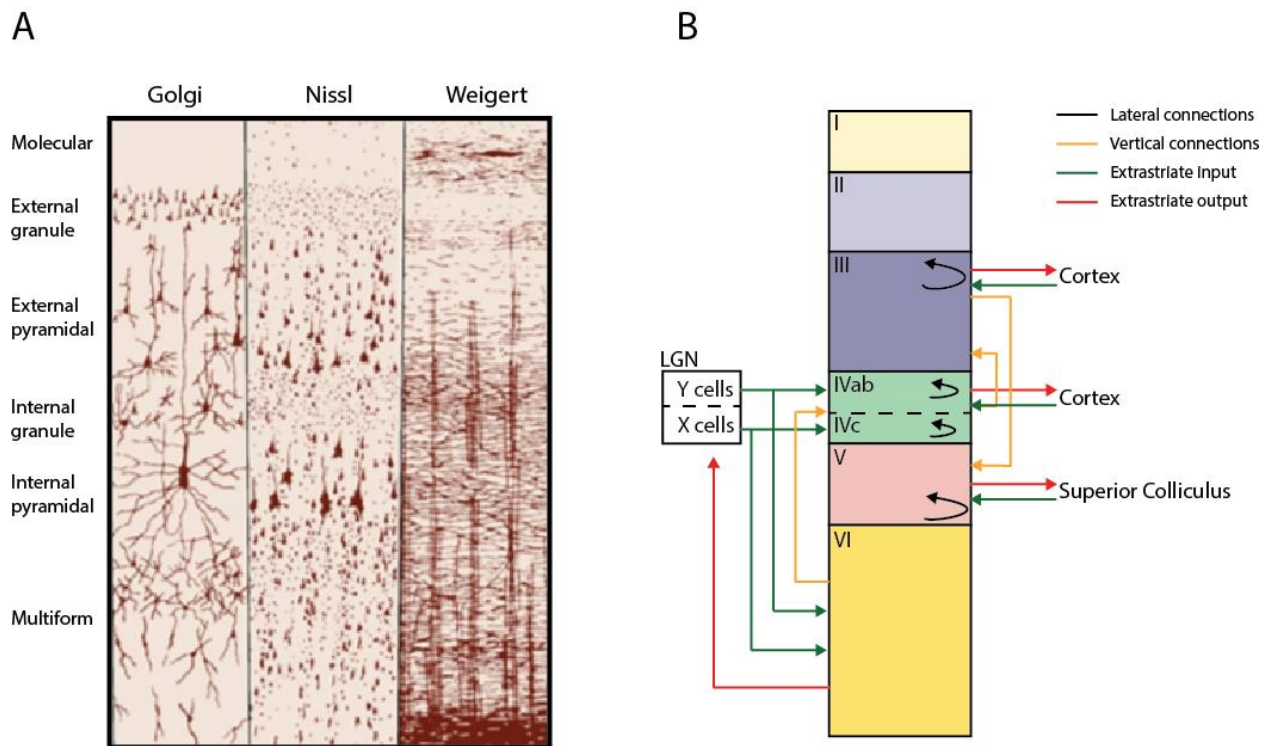


**Figure 5. Primary visual cortex.** (A) Layer configuration stained by three different techniques emphasizing either cell bodies (Nissl) or fibers (Weigert) or both (Golgi). [Modified from Kandel

(2000)]. (B) Simplified primary visual cortex connectivity scheme. Layers III and V have a higher concentration of lateral connections (black curved arrows). Extrastriate input (green arrows) arriving from LGN and higher visual areas of the cortex. Extrastriate outputs (red arrows) connecting back to the LGN and to higher visual areas. Vertical circuits (orange arrows) making interlayer connections.

According to Gilbert and Wiesel (1985) the feed-forward connection is responsible for only about 5% of the excitatory input of V1, leaving the most of excitation to feedback and intrinsic connections. Pyramidal projection cells lead the striate output to extrastriate visual areas and basal structures through glutamatergic connections. Neurons from layer VI project back to LGN. Also, layers III and IV project to higher visual areas such as MT, V2 and V5, and layer V projects to the superior colliculus.

Intrinsically, the primary visual cortex makes excitatory connections between (vertical connections) and within layers (horizontal connections) through pyramidal and spiny stellates cells. There is also an intrinsic inhibition network formed mainly by GABAergic basket cells, however, their connection extent is reduced when compared with excitatory connections (Gilbert, 1992).

As a particular group of intrinsic connections in V1 there exist also interhemispheric connections (IHCs), which link topographically corresponding parts of early visual areas on a similar hierarchical level (V1-V1, V2-V2, and V2-V1) in the two brain hemispheres (Schmidt and Lowel, 2002). Based on its anatomical and functional properties, several authors proposed that these connections can be viewed as a continuation of the horizontal intrinsic network (Rochefort et al., 2009; Schmidt, 2013; Schmidt et al., 1997).

Due to the connectivity and response properties of V1 neurons, the functional role, which was initially attributed to this area, was limited to the extraction of basic stimulus features for higher visual areas in which perceptual processing would take place. Currently, this strictly hierarchical conception of visual processing is considered inaccurate since there is evidence that responses of V1 neurons can be modulated by paradigms involving perceptual grouping of segments (Kapadia et al., 1995) and figure-ground segmentation (Biederlack et al., 2006; Ichida et al., 2007; Kastner et al., 1997; Knierim and van Essen, 1992; Lamme, 1995; Levitt and Lund, 1997; Shushruth et al., 2012; Zipser et al., 1996) or brightness perception (Biederlack et al., 2006; Rossi et al., 1996).

The primary visual cortex's ability to participate in such complex processes is likely to result from horizontal and feedback connections (Angelucci and Bressloff, 2006). In the next two sections we describe the horizontal connections and the IHCs in more detail, aiming to give a theoretical substrate that reflects the role of horizontal connections in

contextual modulation (particularly in figure-ground segmentation) and their functional and anatomical similarities with IHCs.

### 1.1.1. Lateral Intrinsic Connections

Historically, the vertical connections have kept a substantial part of the attention of researchers studying intra-area neural processing. However, many studies indicated the involvement of lateral intracortical connectivity in these processes. A recent study revealed that around 80% of the synapses in a 800 $\mu\text{m}$  diameter column stem from long-range axons of neurons located outside that column (Stepanyants et al., 2009) assigning more emphasis to lateral (and feedback) input from outside the classical receptive field. Excitatory long-range intrinsic connections are formed by myelinated collaterals that leave the vertically descending axon trunk before it enters the white matter and can reach up to 8 mm (long-range horizontal connections) (Schmidt and Löwel, 2002). They terminate in a patchy manner, forming clusters of boutons. These terminations cover areas of about 300 $\mu\text{m}$  to 600 $\mu\text{m}$  in diameter - depending on the labeling technique - and preferentially link columns of similar orientation preference (+/-0 to 30 deg), although columns with oblique (+/-30 to 60 deg) or even orthogonal (+/- 60 to 90deg) preferences can also be connected with decreasing probability (Buzás et al., 1998; Kisvárday et al., 1997; Schmidt et al., 1997). This functional selectivity gives continuity to the network which is likely to contribute to the emergent functional architecture. The modular horizontal network is more prominent in layers II-III and V. Layer IV has shorter and less selective lateral connections, supporting the notion of a different type of processing for that layer (Karube and Kisvárday, 2011; Yousef et al., 1999).

The inhibitory lateral network is about one third to one half of the excitatory network in extent and most of it does not extend farther than 1mm (Schmidt and Löwel, 2002). Its main substrate in the cat's visual cortex is the large basket cells. Only about 5% of the intrinsic connections are inhibitory, yet their influence cannot be measured by this quantitative view since the GABA dynamics are faster than glutamate, leading to higher inhibition than expected from the number of synapses (Gilbert, 1992). Inhibitory connections are less functionally selective than excitatory ones, i.e. they are more equally distributed between iso-oriented, oblique and orthogonal columns (Buzás et al., 2001)

Several functions have been attributed to long-range intrinsic connections like e.g. their contribution to *i*) adaptive long-term changes in cortical topography after peripheral and central lesions, to *ii*) dynamical receptive field properties and to *iii*) contextual influences on classical neuronal responses in V1 (Gilbert and Wiesel, 1992).

Gilbert and colleagues (Das and Gilbert, 1995; Gilbert and Wiesel, 1992) investigated adaptive cortical changes after retinal lesions. The visual cortex contains an orderly retinotopic map of the receptive field's positions. After a retinal (peripheral) lesion the

corresponding cortical area remained initially silenced but its function was altered over time, and was recruited to process a different part of the retina. This process implies not only a topographical reorganization but also changes in the receptive field size as well as its preferences. Therefore, this kind of reorganization was ascribed to the horizontal intrinsic network. Indeed, recently, axonal sprouting of long-range axons has been observed by using 2-photon microscopy in the lesion projection zone (Yamahachi et al., 2009).

Further, despite some controversy, inhibitory lateral connections have been identified as an important part of the orientation tuning mechanism (Crook et al., 1998; Eysel et al., 1990; Sompolinsky and Shapley, 1997; Wörgötter and Holt, 1991). According to this idea, connections from neurons of nearby columns with other orientation preferences inhibit the response of a given cell to a stimulus with an orientation different from its preferred (see Figure 6). On the other hand, long-range excitatory connections were interpreted to create large composite receptive fields by connecting neurons with similar orientation preferences and synchronizing their responses (Gray et al., 1989; König et al., 1993).

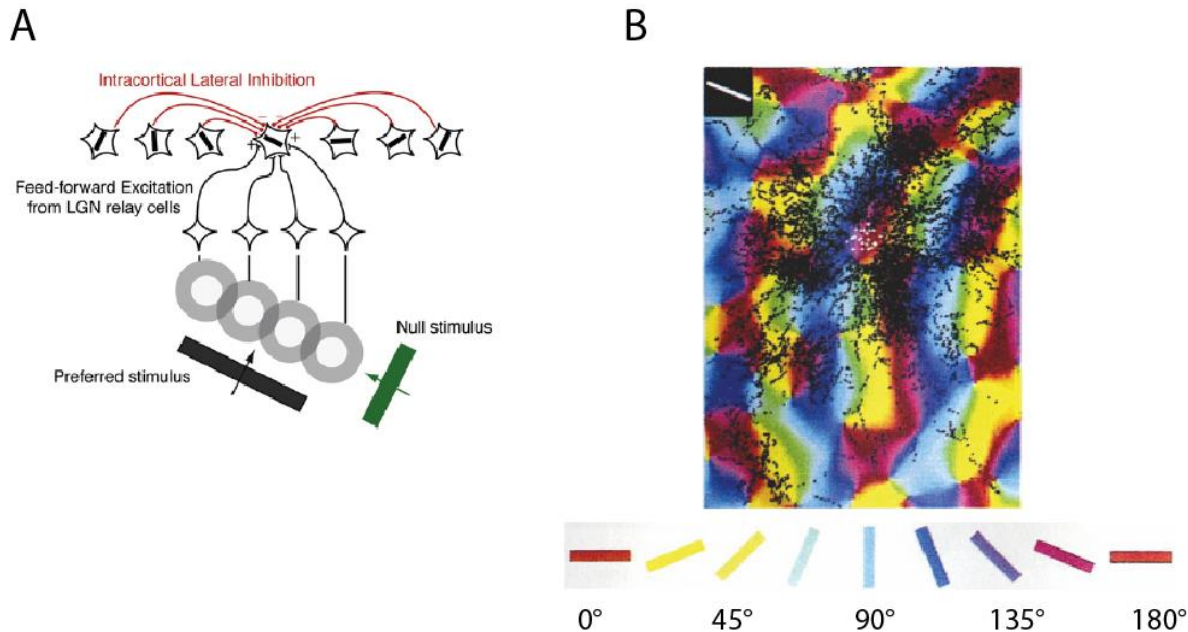


**Figure 6. Lateral connectivity of primary visual cortex.** (A) Simple model of lateral inhibition between cells with different orientation preferences. [Taken from Priebe & Ferster (2008)] (B) Optical image showing columns of similar orientation preferences coded by colors. The black traces indicate axonal boutons made by cells marked as white dots. Note the connections between columns with similar orientation preferences. [Modified from Bosking et al (1997)]

Considering the above mentioned features (e.g. creating large composite receptive fields, giving continuity to the network, orientation selectivity, part of the tuning mechanism) one would expect that the activity of a given cell is not only determined by stimulation of its CRF (feed forward input) but also by influences from other cells processing different areas of the visual field through the lateral connections. The existence of these influences can be concluded from numerous psychophysical experiments demonstrating that some stimulus' features presented in the receptive field depend on the context. Figure 7 depicts, how context can alter the perception of the orientation of lines by the presence of nearby lines with different orientation, or also create illusory contours. It was hypothesized that the physiological basis of these phenomena is the input delivered by orientation-selective lateral connections from beyond the CRF (Gilbert, 1992)

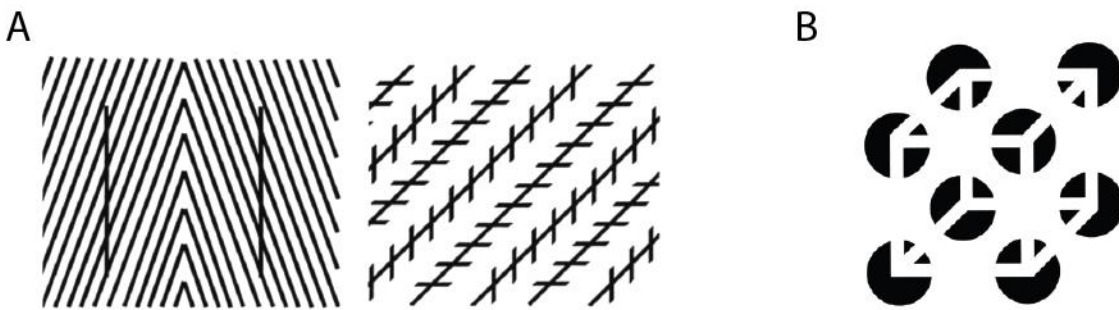


**Figure 7. Perceptual changes.** (A) Apparent orientation changes. [Modified from (Gilbert, 1992)]  
(B) Illusory contours.

### 1.1.2. Visual Callosal Connections

Almost all cortical areas of each brain hemisphere are interconnected through the corpus callosum. The excitatory or inhibitory nature of these connections is still on debate, but their exact functional role as well as some of their anatomical features seems to depend on the area they link. Many authors defend that these connections are mainly excitatory (Galaburda, 1984; Geschwind and Galaburda, 1985; Lassonde, 1986; Watson et al., 1984; Yazgan et al., 1995), supporting the idea of integration of cerebral processing between hemispheres (Bloom and Hynd, 2005). Other researchers postulate that callosal connections inhibit the activity between hemispheres (Cook, 1984; Denenberg et al., 1986; Dennis, 1976; Hubel and Wiesel, 1967) contributing to the functional asymmetry (i.e. one hemisphere dominates a given function) present in processes as language and hand dominance.

In the case of primary visual cortex the callosal connections were assumed to integrate the separate representations of the two hemifields (Hubel and Wiesel, 1967). This is strengthened by anatomical evidence showing that these connections are more prominent at the border between areas 17 and 18, which is the cortical area where the vertical

meridian (VM) of the visual field is represented (Berlucchi and Rizzolatti, 1968; Lepore and Guillemot, 1982; Ptito et al., 2003). In cats, callosal neurons are mainly pyramidal cells and connect similar classes of cells in supragranular layers (mainly layer III) (Innocenti et al., 1986), however, there is also a limited number of GABAergic projection neurons (Buhl and Singer, 1989; Elberger, 1989).

It is still an open question whether callosal connections are a special kind of long-range horizontal connection or whether they have specific properties related to their positioning within the binocular central visual field, or both. In the primary visual cortex, they were proposed to integrate the cortical representation of the two visual hemifields (Choudhury et al., 1965; HUBEL and WIESEL, 1962) and to synchronize the responses to a visual stimulus across (Engel et al., 1991) and also within the two hemispheres (Carmeli et al., 2007).

Callosal connections share important structural features with intracortical horizontal connections like patchy terminal arbors (Houzel et al., 1994) and linking clusters of neurons sharing similar orientation preferences (Rochefort et al., 2009; Schmidt et al., 1997). The split-chiasm preparation confirmed that indirect input from the callosum matches the direct, ipsilateral responses in orientation and CRF position (Berlucchi and Rizzolatti, 1968; Lepore and Guillemot, 1982; Rochefort et al., 2007).

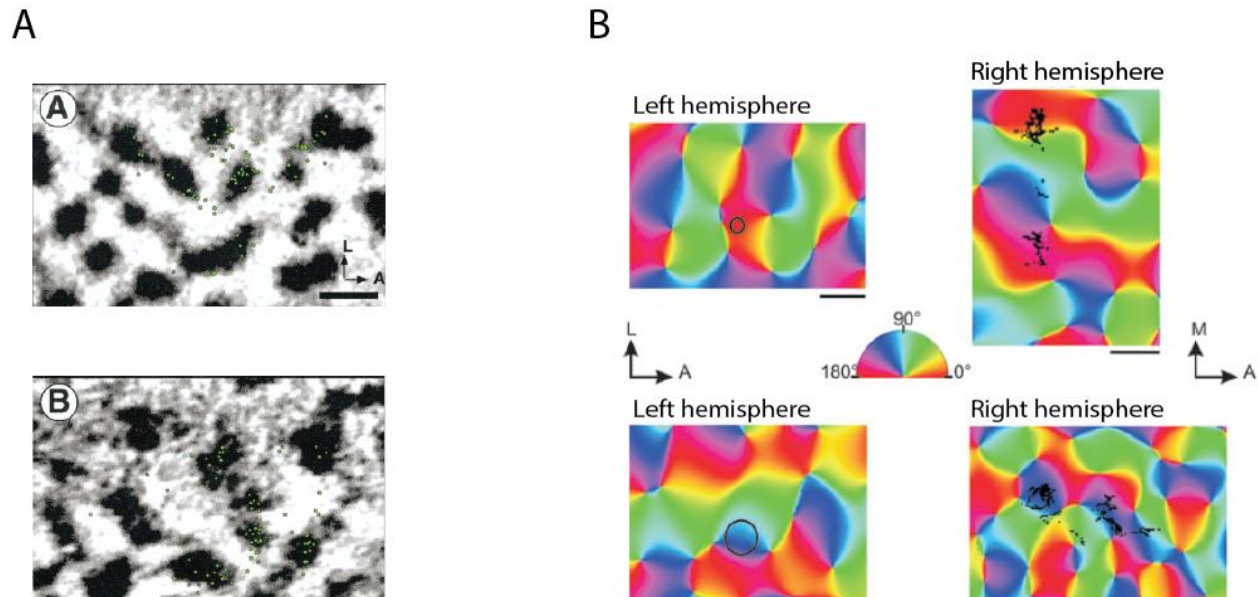


**Figure 8. Orientation specificity of callosal connections.** (A) Two examples of superposition of retrogradely labeled neurons with horizontal preferences (green dots) and maps evoked by horizontal monocular stimulation of the ipsilateral eye. Bar, 1mm. [Modified from (Schmidt et al., 1997)] (B) Two examples of orientation maps from both hemispheres. A dextran amine injection

was performed in the left hemisphere (black circle) and the corresponding marked synaptic boutons in the right hemisphere (black dots). [Modified from (Rochefort et al., 2009)]

Recent evidence from studies using reversible deactivation of the contralateral hemisphere and thus leaving the visual system intact – in contrast to earlier split chiasm approaches – indicates that the callosal connections indeed have a predominantly excitatory integrating function (Makarov et al., 2008; Peiker et al., 2013; Schmidt et al., 1997; Wunderle et al., 2013). Callosal input amplifies responses to ipsilateral CRF stimulation in a multiplicative and stimulus-dependent manner. Inhibitory drives occur highly stimulus-dependent and much less frequent (Wunderle et al., 2013) and the overall balance between inhibitory and excitatory drives matches largely the anatomical numbers given by the intracortical ratio of short and long-range inhibitory/excitatory connections in the primary visual cortex (Kisvárday and Eysel, 1993; Schmidt et al., 2010).

Other functions of visual callosal connections like binocular fusion might arise from their specific localization at the vertical midline of the central visual field but newer studies (Peiker et al., 2011 SFN abstract) confirm that in front-eyed mammals with a large binocular visual field they do not contribute significantly to the ocularity of the interconnected neurons (Minciucchi and Antonini, 1984). Rather, binocular neurons – in contrast to small rodents (Cerri et al., 2010) – seem to be established by the thalamocortical input like anywhere else in the visual field.

A comparison between visual callosal connections and the lateral intrinsic connections (Section 1.1.1) reveals an evident topographical similarity, supporting a strong functional similarity. As opposed to the lateral intrinsic connections the projection through the corpus callosum exhibits the large advantage that its manipulation does not affect directly the recorded neurons (Crook et al., 1998; Girardin and Martin, 2009).

## 1.2. Contextual Stimulation

The work of Hubel and Wiesel on visual receptive field properties allowed the description of neuronal responses to feed-forward stimulation. Today, it is clear that these responses can be modulated by inputs arising from the surround stimulation (i.e. outside the CRF). In general, the nature of the influences mediated by surround stimulation varies. A contrast between center (i.e. inside the CRF) and surround, depending on how that contrast is defined (i.e. orientation, motion, luminance), may increase (facilitation) or decrease (suppression) the neural responses (see Figure 10 for stimulus examples). Lamme and colleagues (1995) showed that neurons in the primary visual cortex of macaque monkeys increased their firing rates when their receptive fields were located in a

square patch embedded by a surround. The patch was made to perceptually pop out as a circumscribed figure by setting differences in the lines' orientation or their direction of motion between figure and surrounding background (Figure 9).

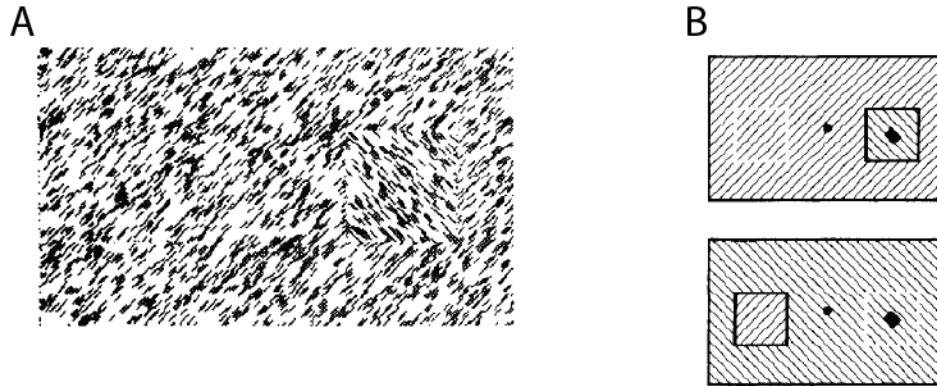


**Figure 9. Contextual stimulus.** [Modified from Lamme (1995)]. (A) Texture stimulus. A square area was defined to perceptually pop out inside the rectangle's right half. This is achieved by differences in the line orientations or direction of motion. (B) The small solid square represents the CRF position of a given cell. Upper figure: The CRF is inside the pop-out figure. In this case response facilitation occurred in comparison to the bottom configuration where the CRF was outside de figure.

In the study of Lamme, the facilitation of firing rate occurred only when the CRF was inside the patch and regardless of the orientation preference of the neuron. This finding raised the idea of a perception related processing mechanism (figure-ground segmentation) already at the level of V1 evidenced as response facilitation. Early on, an iso-oriented “inhibitory” surround was described when stimulating center and surround with iso-oriented stimuli (Allman et al., 1985; Blakemore et al., 1972; Cavanaugh et al., 2002a; DeAngelis et al., 1994; Knierim and van Essen, 1992; Levitt and Lund, 1997; Sengpiel et al., 1997; Toth et al., 1996). However, under different conditions, a facilitation of the center response by iso-oriented surround stimulation had also been observed (Nelson and Frost, 1985; Sillito et al., 1995), although much less frequently.

In humans, Joo and colleagues (2012) measured neural responses of primary visual areas to Gabor stimulation using fMRI and demonstrated that a context configured by orthogonally oriented flankers evoked higher responses than iso-oriented flankers (see Figure 10E). These studies introduced the notion that the surround influence is orientation-specific. Thus, the mechanism computing surround modulation in V1 could be based on the orientation-selective horizontal network and /or feedback circuits (Angelucci and Bressloff, 2006).

Whereas the earlier studies were compatible with the view that the bias for iso- versus cross-oriented suppression or facilitation is not fixed but depends on the stimulus orientation presented to the center, newer studies came to a different conclusion. A maximal suppression is gained when the receptive field and surround are stimulated with the same orientation, and less suppression or facilitation by the orthogonal orientation, independent of whether the center is optimally or non-optimally stimulated (Cavanaugh et al., 2002b; Shushruth et al., 2012; Sillito et al., 1995). As this result cannot be explained by fixed orientation-specific excitatory long-range horizontal or feedback connections, a newer theoretical framework proposed a combination of tuned lateral inhibition and weakly tuned local recurrent excitation (Shushruth et al., 2012). Long-range lateral and feedback circuits would have a context dependent and modulating role on this local recurrent circuit which enables the neurons in the center/foreground of the stimulus to flexibly adapt to the changing feed-forward input.

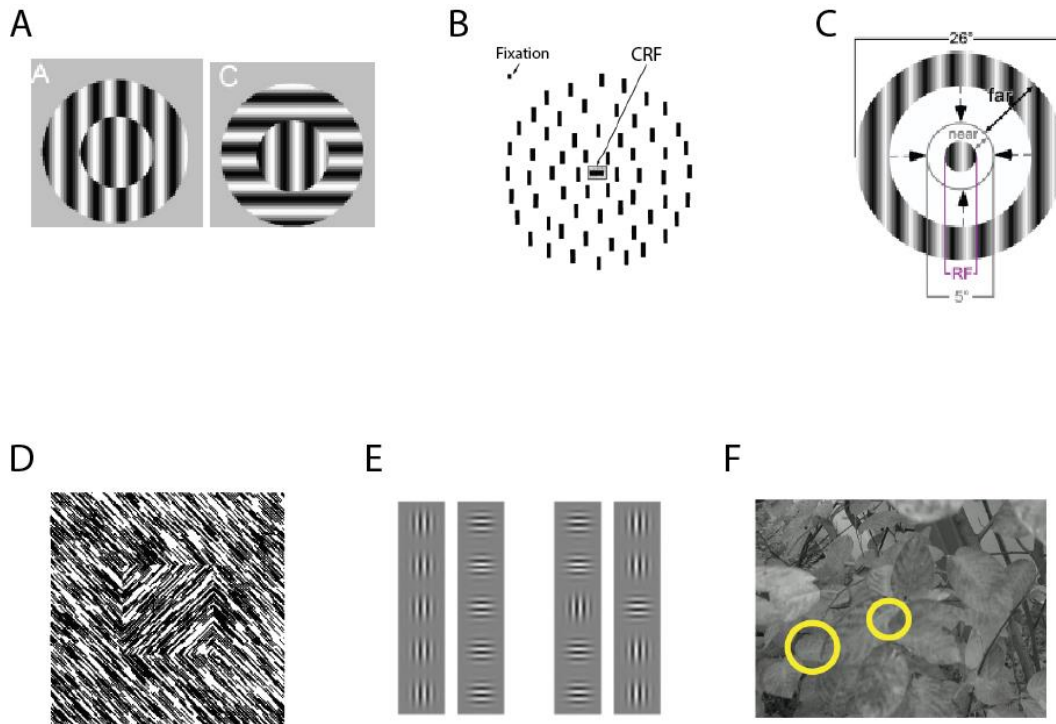


**Figure 10. Context stimulation examples.** (A) Gratings with phase contrast (left) and orientation contrast (right) [Modified from (Biederlack et al., 2006)] (B) Bars with orientation contrast. [Modified from (Knierim and van Essen, 1992)] (C) Oriented grating with a blank gap between center and surround. [Modified from (Shushruth et al., 2012)] (D) Oriented texture contrast. [Modified from (Lamme and Spekreijse, 1998)] (E) Four different conditions using Gabors. The figure was defined as the middle Gabor in each column. [Modified from (Joo et al., 2012)] (F) Natural stimulus. The yellow circles define the figure areas. [Modified from (Haslinger et al., 2012)]

The debate of whether contextual modulation depends or not on a neuron's preferences is based on the activity of single cells. However, since the cortex is a complex network of interconnected neurons, there is growing evidence of stimulus processing at the population level. It was postulated for example that neurons in V1 representing the same object fire in synchrony (Singer, 1993). This proposal is based on the idea of neuronal assemblies introduced by Donald Hebb in 1949 and considers groups of neurons firing together as the elementary unit of information processing, in contrast to the idea of having a single cell to represent each object (Barlow, 1972). In this case, the neuronal representation of a given object is a group of cells firing synchronously, with each cell having the possibility of representing a different basic object feature. This is the base of the binding-by-synchrony theory which considers ensemble synchronization as an effective way of cortical information (Von der Malsburg and Shneider, 1986; Singer, 1994; Hopfield, 1995; Vaadia et al., 1995). Nevertheless, the network mechanism to synchronize the responses of different neurons is still not clear. One hypothesis is that the key of this synchrony could be at the local field potential level, since this signal is the result of the summation of the activity of a neuronal population. More specifically, a group of neurons fire together if they share preferences to discharge, for example, at a particular phase of a local field potential (LFP) wave (Siapas et al., 2005).

However, there is also evidence against this binding-by-synchrony theory showing that simultaneously recorded neurons, with receptive fields stimulated by the same object, fail to synchronize their responses (Lamme and Spekreijse, 1998; Roelfsema et al., 2004). Instead, Roelfsema and colleagues gave experimental support to a binding-by-rate enhancement hypothesis where the neurons encoding features of the same object jointly enhance their responses.

There is also evidence that different coding strategies might exist in parallel. Biederlack and colleagues (2006) used sinusoidal gratings stimulation on anesthetized cats. Whereas orientation contrast led to an increment of firing rate, phase contrast produced an increase in synchrony, suggesting that, depending on certain stimulus features, the figure-ground segmentation could have different electrophysiological correlates.

Taken together, these studies agree with the notion that figure-ground segmentation takes place already at early visual areas, yet the electrophysiological correlates and relations between those and specific stimulus features remain controversial.

In the current thesis, we explore changes in neuronal responses (i.e. spiking activity and LFP's power) to a figure-ground stimulus configuration ("pop-out") while deactivating and reactivating the callosal connections between the primary visual areas. We do so by means of cooling the contralateral hemisphere. In the following we will thus refer to callosal connections as interhemispheric connections (IHCs) because the cooling procedure in

principle deactivates all connections between the two visual cortices, not only the callosal ones though the callosal projection is likely to be the dominant interhemispheric link for the visual system.

The figure-ground stimulus is constructed by presenting an orientation -or motion-contrast to the receptive field surround of the recorded population of neurons. This experimental model enables us to quantitatively and qualitatively characterize the direct contribution of IHCs to the surround effects (contextual modulation) induced by a changing feedforward input (by maintaining the center stimulus constant and introducing an orientation or motion contrast in the surround). We also directly examine the influence of IHCs on the formation of local intrahemispheric neuronal assemblies firing in synchrony and in phase-locking.

## 2. Working Hypothesis

- I. Since there is evidence of figure-ground segmentation in population activity, we thus also expect evidence of that process in LFPs and assembly activity.
- II. Since lateral (and feedback) connectivity have been proposed to have an active role in figure-ground segmentation, we expect that reversible deactivation (cooling) of interhemispheric connections results in a modulation of LFPs and assembly activity.

### 3. Objectives

- Evaluate LFPs evoked by uniform whole-field stimulus in comparison with a stimulus which creates a perceptual pop-out by means of an orientation contrast (gratings) or a motion contrast (natural scene)
- Evaluate coordinated activity of groups of neurons, i.e. assembly activity.
- Evaluate synchronization between LFPs and single unit or assembly activity reflected in phase-locked events.
- Evaluate the contribution of interhemispheric connections resulting from the reversible deactivation of the contra-lateral hemisphere to activity differences caused by figure-ground segmentation

## 4. Materials and Methods

Nine adult cats (labeled as Ca07, Ca10, C11, C12, C15, C27 and C28, C29 and C31, 4 males and 5 females) were prepared and maintained under anesthesia and artificially ventilated during the experiments. Experiments Ca07-C15 were performed at the Max Planck Institute for Brain Research in Frankfurt, Germany, the remaining four experiments were performed at the Brain Institute of the UFRN in Natal. All procedures were approved by the local animal right's authority at the Regierungspräsidium Darmstadt in the state of Hessen, or by the ethic committee of the Federal University of Rio Grande do Norte in Natal (UFRN).

### 4.1. Anesthesia and Physiological Monitoring

Initially, all animals were anesthetized by intramuscular injection of 10 mg/kg ketamine hydrochloride and 1 mg/kg xylazine hydrochloride. Subsequently, they were artificially ventilated with a mixture of 0.6/1.1 % halothane (for recording/surgery respectively) and N<sub>2</sub>O/O<sub>2</sub> (70/30%). After completion of surgical procedures and during the entire experiment, the animals were maintained paralyzed by continuous intravenous infusion of pancuronium bromide (0.15 mg/kg/h). The physiological stability of the animals during anesthesia was evaluated by continuously monitoring the electrocardiogram and CO<sub>2</sub> levels in the expiration air. During all experiments we aimed to keep the heart rate between 100 bpm and 170 bpm and the CO<sub>2</sub> output between 2.5 and 3.7 %mmHg.

### 4.2. Recording Area Identification

Two craniotomies were performed (one in each hemisphere according to Horsley–Clarke coordinates AP 0 to -2, ML +2), exposing a portion of areas 17 and 18 and the border between. The bone bridge above the sagittal sinus was left intact to maintain a natural barrier between the two hemispheres. A recording chamber was implanted over the left hemisphere for optical imaging of intrinsic signals during grating stimulation with different orientations. Intrinsic signal imaging measures the absorption of red light by superficial cortical regions consuming more oxygen during visual stimulation (Grinvald, 1996). We stimulated with two different spatial frequencies in order to get the optimal response from areas 17 (0.5 cyc/deg at 4 deg/sec) and 18 (0.15 cyc/deg at 16 deg/sec). This kind of stimulation served to identify the portion of each of the two areas exposed in the craniotomy and their orientation column pattern. As a result, a map was obtained where orientation columns and area limits are defined (Wunderle et al., 2013). This map was taken as a reference for electrode implantation (Figure 11)

## 4. Materials and Methods

### 4.2 Recording Area Identification

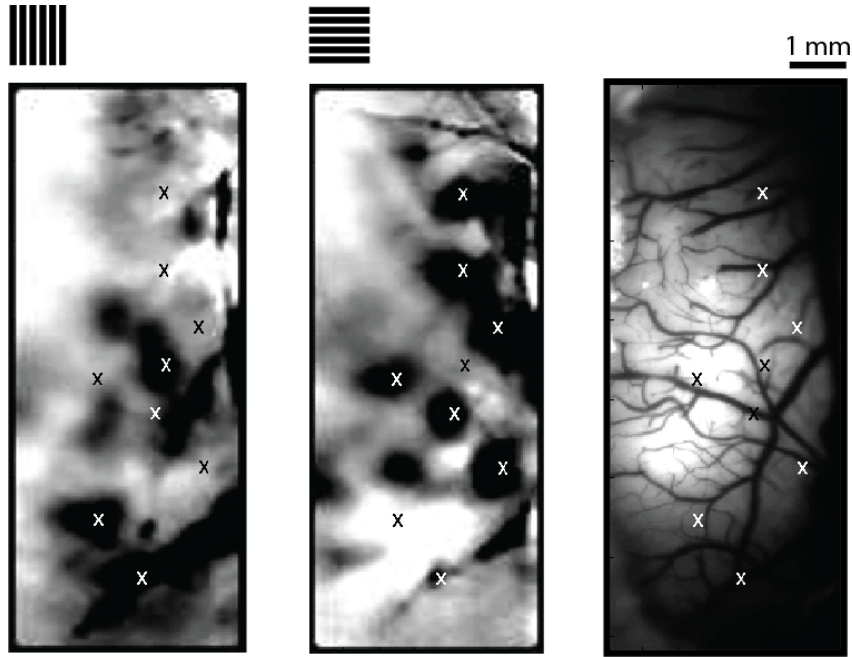


**Figure 11. Intrinsic signal map.** Left: Map obtained from vertical gratings stimulation. Center: Map obtained from horizontal grating stimulation. Right: Photo of the cortex area exposed. The markers indicate a possible location for electrodes implantation. These points were selected for displaying a clear response to the stimulation (orientation columns). White and black markers are used just for contrast matters with no color-coding involved.

### 4.3. Electrode Implantation

Two  $4 \times 4$  arrays of Tungsten electrodes (MicroProbes, Gaithersburg, USA) were implanted on the left hemisphere of eight out of nine cats. A third  $4 \times 4$  array was implanted in the ninth animal (Figure 12). The arrays had an inter-electrode spacing between 250 $\mu\text{m}$ -400 $\mu\text{m}$  depending on the experiment. The first array (device I) aimed at area 18 and the second array (device II) aimed at the transition zone between areas 17 and 18. On the right hemisphere a surface cryoloop was implanted on the topographically corresponding region (Wunderle, 2012). All signals were recorded from supragranular layers (recording depth between 200-700 $\mu\text{m}$  using Narishige micro drives).

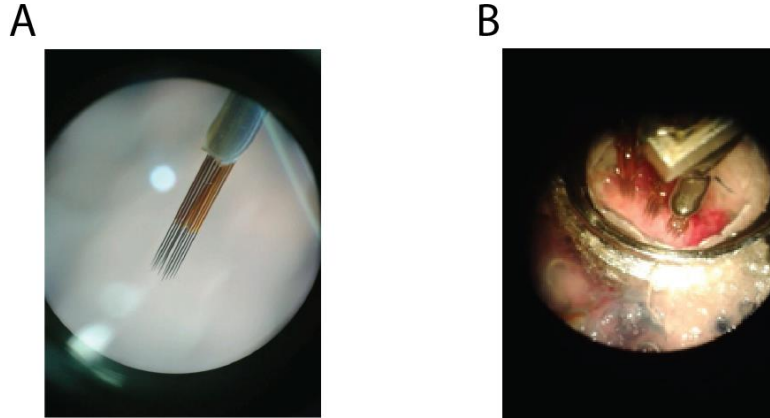


**Figure 12.** (A) Electrode matrix (4x4, 250 $\mu$ m between electrodes) (B) Recording chamber and three implanted matrixes. Both photos were taken through the microscope lens.

#### 4.4. Stimuli

Two stimuli categories were presented during the experiments (square gratings and natural scenes) in two different configurations (whole-field -WF- and Patch). The Patch configuration was defined by selecting an area (which defines the *figure*) to perceptually pop-out by setting an orientation or direction of motion contrast between the figure and the surrounding area (ground).

In the case of grating stimulation (all experiments), the WF configuration consisted of two sets of 4 full-field gratings oriented clockwise in steps of 45 degrees moving in one of the two directions perpendicular to the bars orientation. The Patch configuration consisted of the same eight full-field gratings containing a squared grating patch (12deg x 12deg of visual field angle) with an orthogonal surround also moving in one of the two directions perpendicular to their own orientation (see Figure 13A). All gratings had the same spatial and temporal frequency with parameters adapted to the response properties of the majority of the recorded neurons in the respective sample (area 18: 0.15 cyc/deg and 16 deg/sec).

In the case of natural scene stimulation (two experiments), the WF configuration consisted of a full-field grayscale image moving in all cardinal directions at 15 deg/sec (4 conditions, see Figure 13B). Here, the Patch configuration consisted of a round centered patch of 10 degrees diameter moving either into the direction orthogonal to the surround (4 conditions) or into the direction opposite to the surround (4 conditions). In order to minimize any contour, the border between the patch and the surround was shaded using a 20-point moving average.

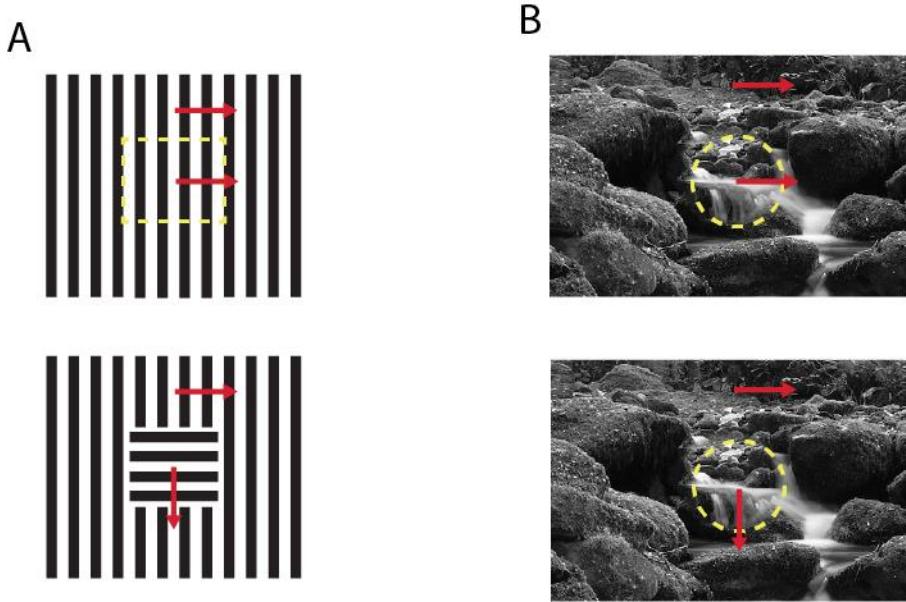


**Figure 13. Examples of the two stimulus categories.** (A) Square gratings in two different configurations: WF (upper sketch) and Patch (lower sketch). (B) Natural scene. Same conventions as in (A). Red arrows indicate the direction of motion. The complete set of conditions for each stimulus category is depicted in Supplementary Figure 1.

#### 4.5. Cooling Procedure

The cryoloop (fitted with a surface thermometer, dimensions: 7 x 3.4mm) was cooled by pumping chilled methanol (-70°C) through it, maintaining the cortical surface between 1°C and 3°C (Figure 10). This temperature is known to be sufficiently efficient to knock out all cortical layers between the two loop shanks and up to 2mm in its vicinity (Lomber et al 1999). It thus silences the interhemispheric input from a restricted part of the visual areas in the contralateral hemisphere. After having reached the target temperature a period of 5 min was left to stabilize the cortex temperature until recordings were performed. During the recording, the temperature of both methanol and cortical surface was continuously monitored to ensure efficacy of the cooling procedure. After the recordings, the methanol pump was switched off and the cortical temperature left to recover and stabilize during a 40min period. One of the main advantages of this procedure is that it is reversible, allowing a causal approach.

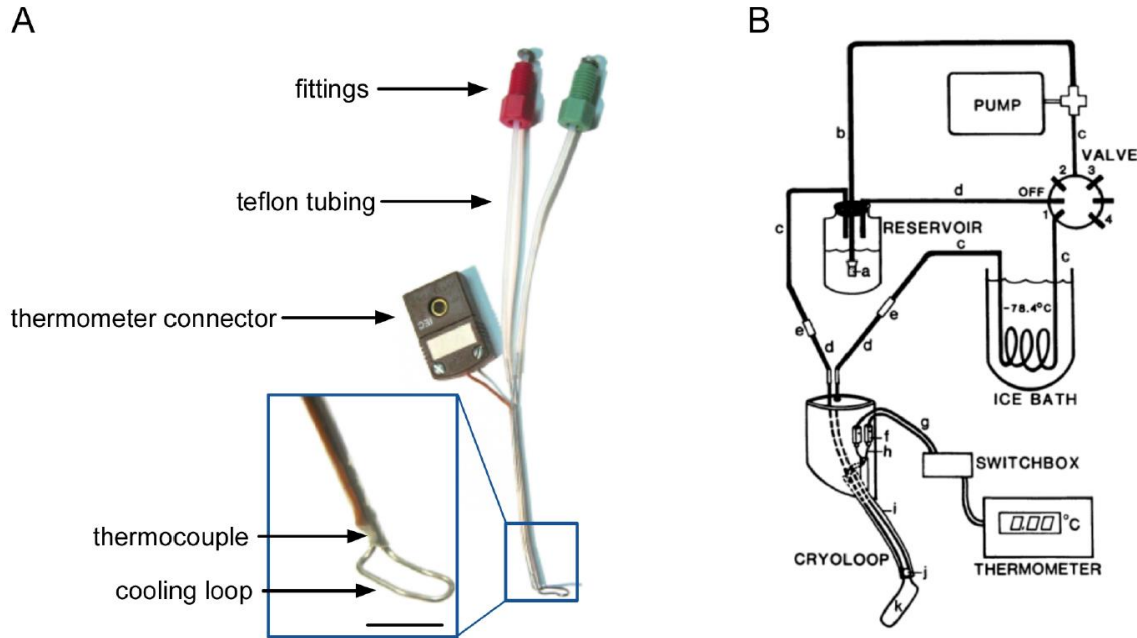


**Figure 14. Cooling setup.** [Taken from (Wunderle, 2012)] (A) Cooling probe with a thermocouple attached. (B) Cooling system. Chilled methanol is pumped through the system while the probe temperature is monitored.

#### 4.6. Data Recording

Both recording and stimulus presentation were accomplished using custom software in LabView (MEC and SPASS by S. Neuenschwander). In a first step, a CRF mapping was performed by stimulating with a single bar oriented in 22.5° steps moving in the perpendicular direction (16 conditions). For each condition a peri-stimulus time histogram (PSTH) was computed in order to identify the variation of spiking activity over time. After considering all conditions and knowing the position of the bar at the PSTH's peak time, we could infer the area of the visual field that, when stimulated, produced the response of the measured channel (Fiorani et al., 2014).

Before data recording, recording sites with well-defined CRF were identified based on visual inspection and the monitor position was adjusted in order to maximize the number of CRF within the patch area. Then, a first recording session was performed (baseline) where LFP and spiking multiunit activity from 32 recording sites were collected (48 for the ninth cat) at 1KHz and 32KHz respectively, in recordings of 2 seconds including 250ms pre stimulus, 250ms static and 1500ms of moving stimulus (see Figure 15). Each stimulus condition (gratings or natural scene) was repeated 20 times in a pseudo-randomized manner.

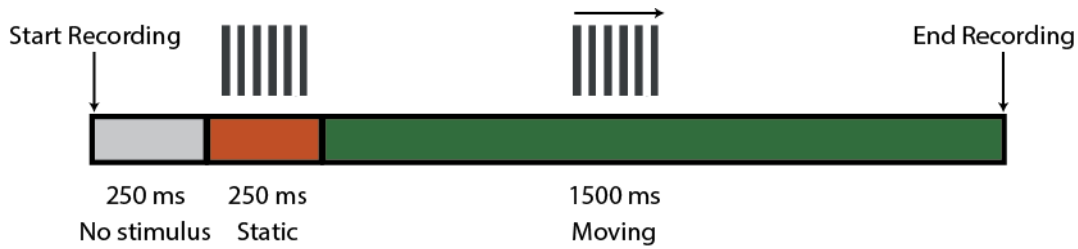


**Figure 15. Stimulation scheme of a single recording.** After the data acquisition starts there is a 250ms blank interval followed by 250ms of static and 1500ms of moving stimulus.

Subsequently, the right hemisphere was cooled and after temperature stabilization a new recording session was executed (cooling, see Section 4.5). The cooling session was followed by a resting period of 40min to recover normal cortical temperature and stabilize responses until a third and final recording period was performed (recovery).

#### 4.7. Data Analysis

All data analysis was performed using the Matlab signal processing toolbox and customized codes to read from LabView, organize, select and analyze the recorded data. As pre-processing procedure all recordings were visually inspected in order to identify and discard possible damaged recording sites or artifacts.

##### 4.7.1. Orientation and Direction Tuning of Multiunit Activity

In order to define selection criteria we characterized the multiunit activity from each recording site according to three main parameters: Receptive field position (see Section 4.6), orientation preference, and direction of motion preference; the last two defined by an angle and a tuning index. The tuning index was calculated by equation 1, i.e. by vectorial addition of spike counts across all trials,

$$\text{Tuning Index} = \frac{\sqrt{(\sum R(\theta_i) \cos(\theta_i))^2 + (\sum R(\theta_i) |\sin(\theta_i)|)^2}}{\sum R_i} \quad (1)$$

where *Tuning Index* can be an orientation index (OI) or a direction index (DI),  $R(\theta_i)$  is a vector with magnitude equal to the accumulated spike count as response to condition  $i$  across all repetitions and angle defined by  $\theta$  in Figure 16. The index has a range between 0 and 1 considering the first as the worst possible case where a unit has exactly the same

response (if any) to all conditions, and the second the ideal case where the unit responds only to a single condition.

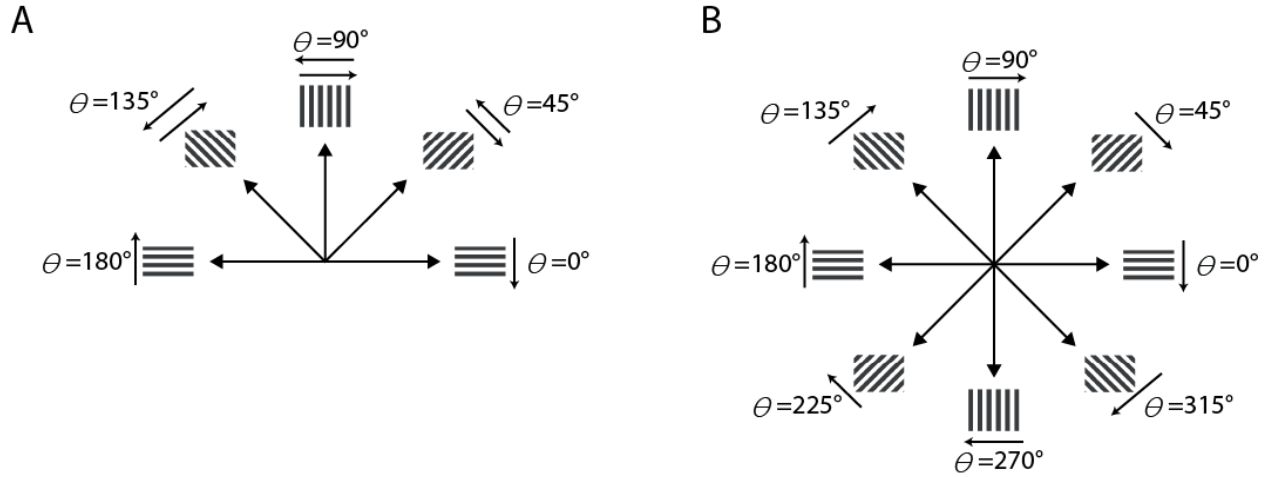


**Figure 16. Correspondence between stimulus conditions and angles.** (A) Angles for OI computation. Note that stimulus conditions with the same orientation contribute to the same vector regardless of the direction of motion. (B) Angles for DI computation. Note that stimulus conditions with contrary direction of motion contribute to opposite vectors. In both cases, the resultant is the vectorial sum across all trials normalized by the sum of all responses.

#### 4.7.2. Firing Rates and Power Spectral Density

First, for each stimulus condition, the mean firing rate (FR), defined by equation 2 was computed for each recording site as a response to each stimulus condition.

$$FR(c) = \frac{\sum_{tr_c=1}^{20} spk(tr_c)|_{t_0}^{t_1}}{T} \quad (2)$$

where  $FR(c)$  denotes the mean firing rate during the presentation of stimulus condition  $c$ , computed by adding the spike counts  $spk$  obtained in each trial  $tr_c$  of  $c$  in the moving period of the stimulation (see Figure 15) between  $t_0=500\text{ms}$  and  $t_1=2000\text{ms}$ . This value was normalized by the length of the moving period  $T=1500\text{ms}$ .

For LFP recordings a power spectral density (PSD) was computed for the moving stimulation period described in FR computations above. The PSD is an estimate of energy distribution across frequencies of a given time series and allows to detect periodic events (oscillations) in LFP signals by identifying specific bands with higher energy. It is defined by equation 3

$$PSD(\omega) = \frac{F(\omega)F^*(\omega)}{2\pi} \quad (3)$$

$$F(\omega) = \int_{-\infty}^{\infty} f(t)e^{-i\omega t} dt \quad (4)$$

Where  $F(\omega)$  denotes the Fourier transform of time series  $f(t)$  defined in equation 4 (in this case the LFP signal),  $\omega$  denotes frequency and  $F^*(\omega)$  is the  $F(\omega)$  conjugate. There are several methods to compute the PSD. Here the Welch's method was used which calculates an average of periodograms obtained from several overlapping time windows across the signal, reduces the noise and provides a good PSD estimate. For these calculations a Hamming window of 250ms with 50% overlapping and a frequency resolution of 0.5Hz were defined.

In a study of awake cats, visually stimulated with sine gratings, Kayser and colleagues (2004) suggested that temporal and structural stimulus features could be locked to the power of different frequency bands (23Hz to 36Hz and above 109Hz for temporal features and 8Hz to 23Hz and between 36Hz and 109Hz for structural features). Based on this finding, in addition to qualitative inspection of PSD from our data (see Figure 17), we computed the power (defined as the area under the curve) of three different frequency bands: 10-20 Hz (Alpha), 20 – 50 Hz (Low Gamma) and 50 – 90 Hz (High Gamma) (Niessing et al., 2005). From now on, we'll use the abbreviations LG and HG to denote low gamma and high gamma rhythms respectively.

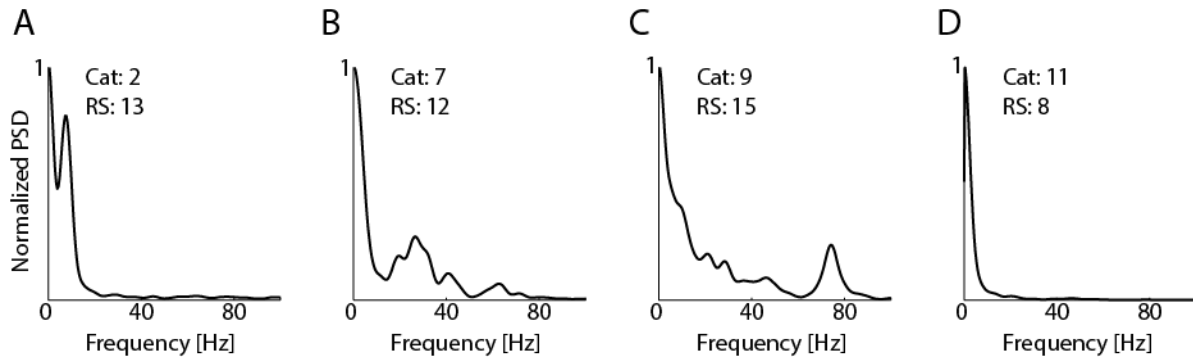


**Figure 17. Representative examples of four PSD.** Obtained from different cats at recording site  $RS$  for a single presentation of a given condition. In general terms, the majority of PSD showed a clear power concentration in Alpha (A), Low Gamma (B), or High Gamma (C) bands. However there are also some recordings with an exponentially decreasing PSD (D).

In order to quantify the figure-ground segmentation an index was defined as follows:

$$SI = \frac{R_{Patch} - R_{WF}}{R_{Patch} + R_{WF}} \quad (5)$$

where  $SI$  is the segmentation index,  $R_{Patch}$  denotes the magnitude of the neuronal response (FR or LFP band's power) to a given Patch condition, and  $R_{WF}$  denotes the magnitude of the same response to the WF condition. Since we aim to quantify the effect of surround, the  $SI$  was computed just for WF-Patch responses pairs that maintained the same stimulation of the CRF (feedforward input) between the two conditions. The  $SI$  ranges from -1 to 1 with more positive values indicating higher responses to Patch stimulation.

To quantify the IHCs deactivation effect on neuronal responses (FR or LFP band's power), a cooling index was defined as:

$$CI = \frac{R_C - R_B}{R_C + R_B} \quad (6)$$

where  $CI$  is the cooling index,  $R_B$  denotes the response magnitude to a given condition (WF or Patch) during Baseline recording and  $R_C$  denotes the same response during cooling recording. This index also ranges from -1 to 1 with positive values indicating a response increase in the absence of interhemispheric input and negative values indicating a response decrease during the same recording. Note that response increases during cooling indicate the release of inhibitory influences in the intact system and decreases indicate the release from excitatory influences.

#### 4.7.3. Assembly Detection

According to the Hebbian theory "*any two cells that are repeatedly active at the same time will tend to become associated, so that activity in one facilitates in the other*" (Hebb, 1949); this process results in groups of neurons with the tendency to fire together known as neuronal assemblies. In order to identify such a tendency it is necessary to isolate the activity of single neurons. As our spiking data from each recording site could originate from more than one neuron, a spike sorting method was necessary, however, in order to track the activity of single units along the entire experiment, we first concatenated the spiking data from baseline, cooling and recovery recording periods before sorting. We used *Waveclus*, a spike sorting toolbox developed by Quiroga and colleagues (2004) to determine the spiking times of single units based on multiunit activity. The toolbox calculates a set of parameters based on wavelet decomposition of spike waveforms, followed by a super-paramagnetic clustering of these parameters (for details see Quiroga, 2004) with each cluster containing the spike times of one single unit.

## 4. Materials and Methods

### 4.7.3 Assembly Detection

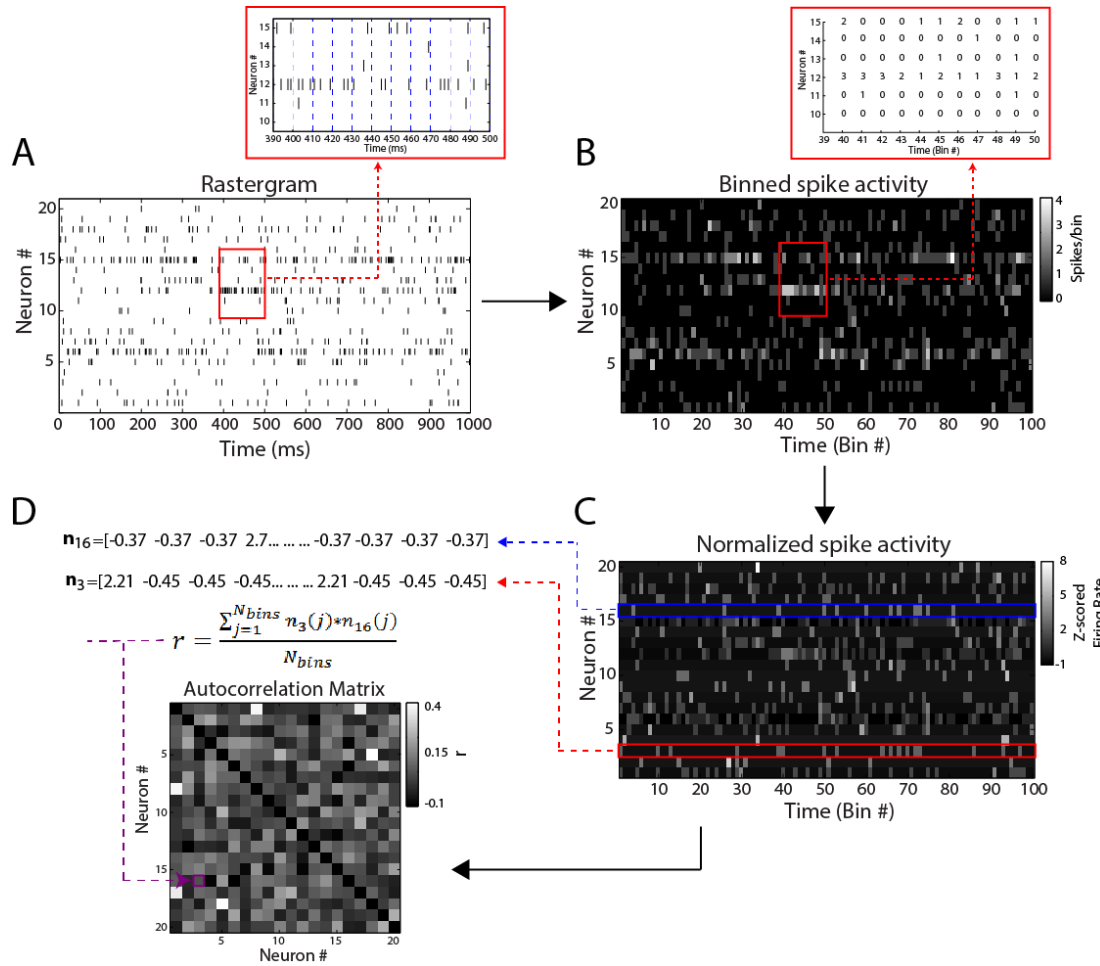


**Figure 18. General overview of the construction of the normalized rastergram Z and autocorrelation matrix computation.** [Modified from (Lopes-dos-Santos et al., 2011)] (A) Rastergram. Each line represents a neuron and each mark denotes an action potential (spike) (B) Five milliseconds bins were defined and the spikes inside each bin were counted resulting in the binned spike activity. (C) Spiking activity normalized by z-score. (D) Autocorrelation matrix. Each element is computed by linear correlation of a pair of neuronal activity (lines)

The spiking times of single units were organized into a rastergram (Figure 18A) where each line corresponds to a single cell's activity. Then, the rastergram was binned using 5ms non-overlapping time windows counting the number of spikes in each bin (Figure 18B). The binned rastergram was z-scored in order to normalize each neuron's activity obtaining zero mean and unit variance for each row (Figure 18C).

Based on the z-scored rastergram ( $Z$ , with  $B$  bins and  $N$  neurons) we identified neuronal assemblies as proposed by Lopes-dos-Santos et al. (2013). The method is a variation of the method previously proposed by the same author (Lopes-dos-Santos et al., 2011. See supplemental material for the full text). In general terms, the method begins by calculating

the number of assemblies based on the eigenvalues of the autocorrelation matrix of Z. If Z is a random matrix (i.e. without ensemble activity) these eigenvalues follow the Marcenko-Pastur distribution defined in equation 7.

$$p(\lambda) = \frac{q}{2\pi\sigma^2} \frac{\sqrt{(\lambda_{max} - \lambda)(\lambda_{min} - \lambda)}}{\lambda} \quad (7)$$

where  $q = B/N$ ,  $\sigma$  is the standard deviation of the elements of Z (since Z is the result of z-score normalization, in this case  $\sigma = 1$ ;  $\lambda_{max}$  and  $\lambda_{min}$  are defined by:

$$\lambda_{min}^{max} = \sigma^2 \left( 1 \pm \sqrt{1/q} \right)^2 \quad (8)$$

If Z is not random (i.e. contains ensemble activity), some eigenvalues of its autocorrelation matrix lie outside the theoretical boundaries determined by equation 8 (see also Figure 19), with the number of eigenvalues above the upper boundary ( $N_{as}$ ) indicating the number of assemblies in Z.

In order to identify each assembly, first the eigenvectors corresponding to the  $N_{as}$  eigenvalues were used to reduce the dimensionality of Z. Then, an independent component analysis was made to find the assembly patterns (Lopes-dos-Santos et al., 2013).

## 4. Materials and Methods

### 4.7.3 Assembly Detection

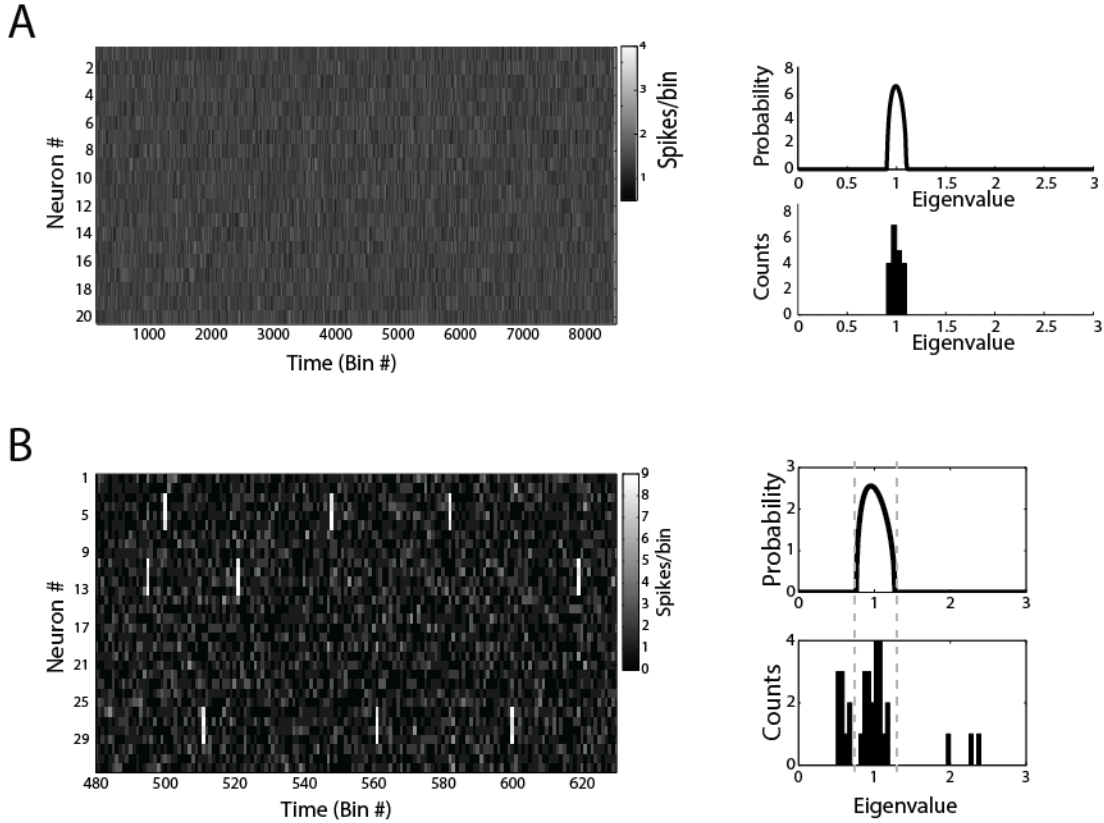


**Figure 19. Examples of Marcenko-Pastur distributions** [Modified from (Lopes-dos-Santos V et al. 2011)]. (A) Left: Binned spiking activity of 20 simulated independent neurons. Right: Theoretical Marcenko-Pastur distribution (up) and eigenvalues distribution (down). Note that the eigenvalues follow the Marcenko-Pastur distribution. (B) Left: Binned spiking activity of 32 simulated neurons. Three assemblies were artificially defined (assembly 1: neurons 4 to 7, assembly 2: neurons 10 to 13 and assembly 3: neurons 26 to 29). Right: same as (A). Note that in this case there are three eigenvalues above the upper boundary of the Marcenko-Pastur distribution matching the number of assemblies simulated.

The result of the assembly detection is a set of  $N_{as}$  assembly patterns of  $N$  values where  $N_i$  is the weight of the  $i_{th}$  neuron in a given pattern. The largest the weight the more often that neuron takes part in the assembly.

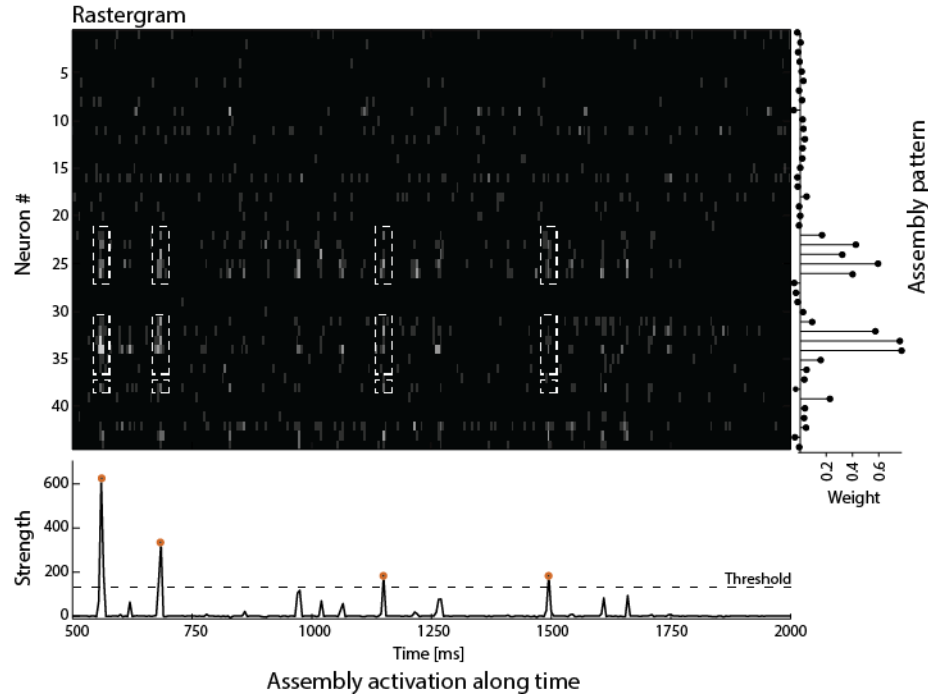


**Figure 20. Assembly pattern and assembly activation along time.** The figure shows a 1500ms length rastergram representing the spiking activity of 44 neurons during one trial. Right: Assembly pattern. Each neuron (lines in the rastergram) is associated with a weight value. Neurons with high weight are more likely to participate in the assembly activity. Lower trace: Projection of the assembly pattern on the spiking activity in each time bin. The assembly is considered active when its projection exceeds a threshold (dashed black line). Note that the firing rate of neurons with high weight (within the dashed white squares) simultaneously increases at the time bin the assembly activity reaches threshold (orange dots).

As a last step, each pattern was projected along the rastergram in order to quantify the assembly's activation on each time bin. At a given time bin, the more similar the bin and assembly patterns are, the higher the values of the projection will be, thus indicating stronger assembly activation. In order to define specific times of activation it was defined that the assembly is active in time bins with projection values above the percentile 99.

#### 4.7.4. Phase Locking

A phase locking analysis was made in order to explore coordinated activity between spiking elements (single cells or assemblies) and LFP. This analysis evaluates if these elements have a preference to occur when a given LFP's frequency band (Alpha, LG or HG) is at a certain phase. In simple terms, for each time point where a spike event occurs (i.e. single cell spike or assembly activation), the LFP's phase is extracted. Intuitively, if such a phase preference does not exist, the distribution of extracted phases will be uniform. Otherwise, the distribution will indicate a higher incidence of the preferred phase.

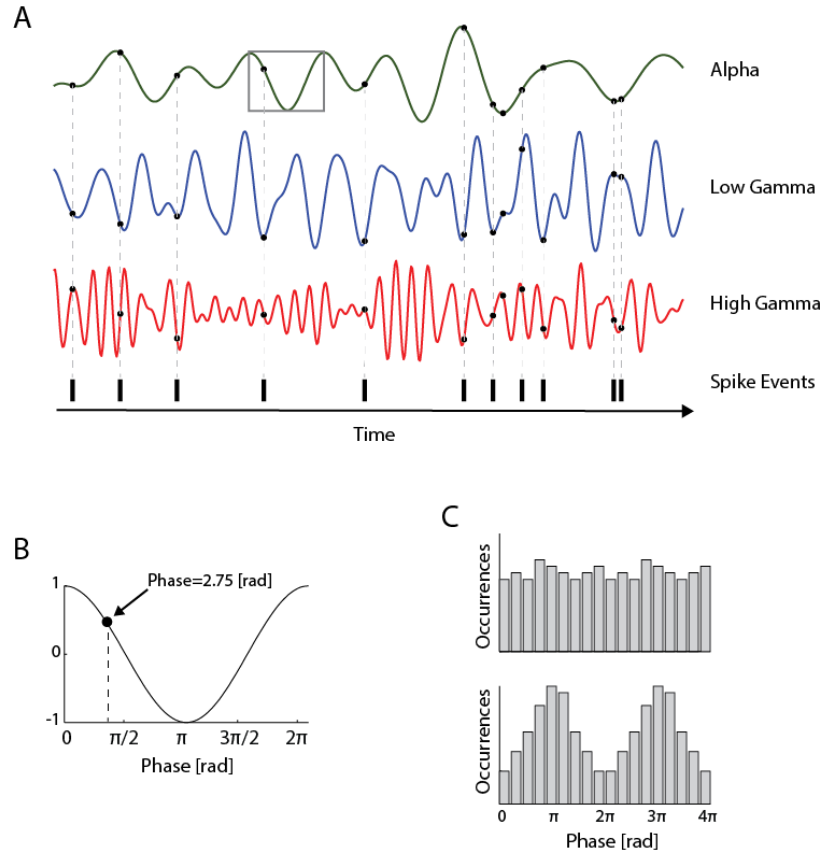


**Figure 21. General overview of phase locking analysis.** (A) Filtered LFP in three different frequency bands (Alpha, LG and HG). Short black lines at the bottom indicate the occurrence of a spike event in time (i.e. a spike from a single cell or assembly activation). For each time point, a phase of each rhythm is extracted (black dots) (B) Detail from grey square in (A). (C) Illustrative examples of two phase distributions. Upper histogram: uniform distribution indicating no phase preferences. Lower histogram: Non-uniform distribution showing preference for an occurrence of a spike event in moments when the LFP's phase is around  $\pi$  radians.

To evaluate whether a phase distribution is uniform or not, a circular Rayleigh test of non-uniformity was performed. When this test indicated non-uniformity, we evaluated the strength of the phase preference by fitting the phase distribution to a Von Mises function and calculated its *kappa* ( $K$ ) value which is a dispersion measure. The higher the  $K$ , the lower the dispersion is. Thereby, regarding the spiking elements, values of  $K$  are directly associated with their phase selectivity.

## 5. Results

### 5.1 Recording Sites Characterization

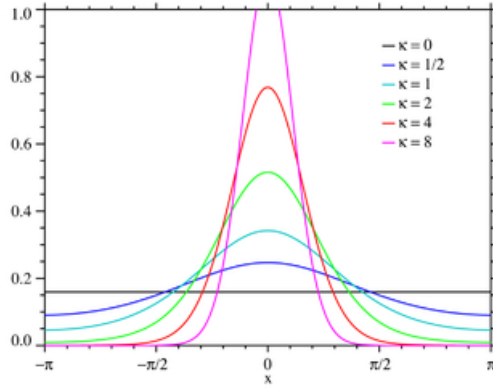


**Figure 22. Von Mises distribution** for different  $K$  values. Note that the higher the  $K$  the narrower the distribution. The x-axis corresponds to radians and y-axis to probability. [Obtained from [http://en.wikipedia.org/wiki/Von\\_Mises\\_distribution](http://en.wikipedia.org/wiki/Von_Mises_distribution)]

If the number of spike events is low enough, the phase distribution can be poorly determined introducing a bias in  $K$  computations. In order to avoid these biased values, we excluded single cells and assemblies with too low activations (for details see Results).

## 5. Results

### 5.1. Recording Sites Characterization

We recorded and inspected a total of 544 recording sites from sixteen different datasets (a new dataset was defined by lowering the electrodes at least 150 $\mu$ m into the cortical surface from the previous recording depth; see Table 1) from which a set of 406 sites presented a well-defined receptive field (Figure 23A. Left).

**Table 1.** Number of datasets and recording site for each cat

Cat Code	Number of datasets	Number of recording sites
Ca7	1	16
Ca10	2	32
C11	1	32
C12	1	32
C15	2	64
C27	1	32
C28	3	96
C29	3	144
C31	2	96

Regarding the CRF's position, we classified the recording sites as lying inside the patch area ( $n=282$ ), at the border ( $n=27$ ) or outside ( $n=97$ ). We also classified each recording site as moderately to highly selective to orientation ( $OI>0.2$ ,  $n=302$ ) or direction of motion ( $DI>0.1$ ,  $n=273$ , Figure 23B) or poorly selective to orientation ( $n=104$ ) or direction of motion ( $n=233$ , Figure 23C).

## 5. Results

### 5.1 Recording Sites Characterization

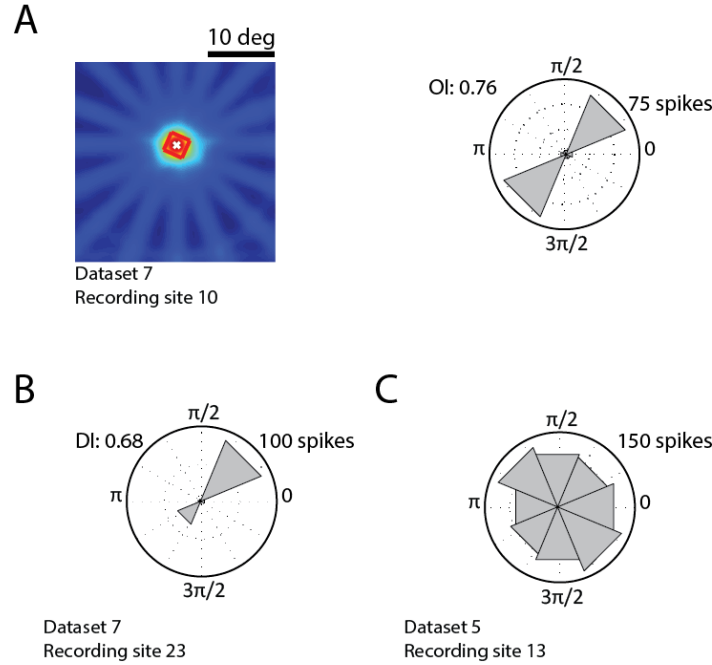


**Figure 23. Recording sites characterization.** (A) *Left:* Example of recording sites with well-defined CRFs, inside the patch area. *Right:* Tuning polar plot from the same recording site. OI stands for orientation tuning. Note that the multi-unit is highly orientation selective. (B) Example of tuning polar plot, from another recording site, revealing high selectivity to direction of motion. DI, direction selectivity index (C) Example of a poorly selective recording site according to all criteria. In all plots the outer circle is scaled to the maximum number of spikes (upper left).

In case of grating stimulation we selected recording sites which were highly selective to orientation stimulation and whose CRF was inside the patch area ( $n=205$ , mean OI:  $0.47 \pm 0.17$  SD) aiming to consider the optimal responses from each recording site. Since the natural scene stimulus can't be described in terms of orientations we selected the responses from recording sites which were highly selective to direction of motion and whose CRF was inside the patch area ( $n=184$ , mean DI:  $0.27 \pm 0.14$  SD).

## 5. Results

### 5.1 Recording Sites Characterization

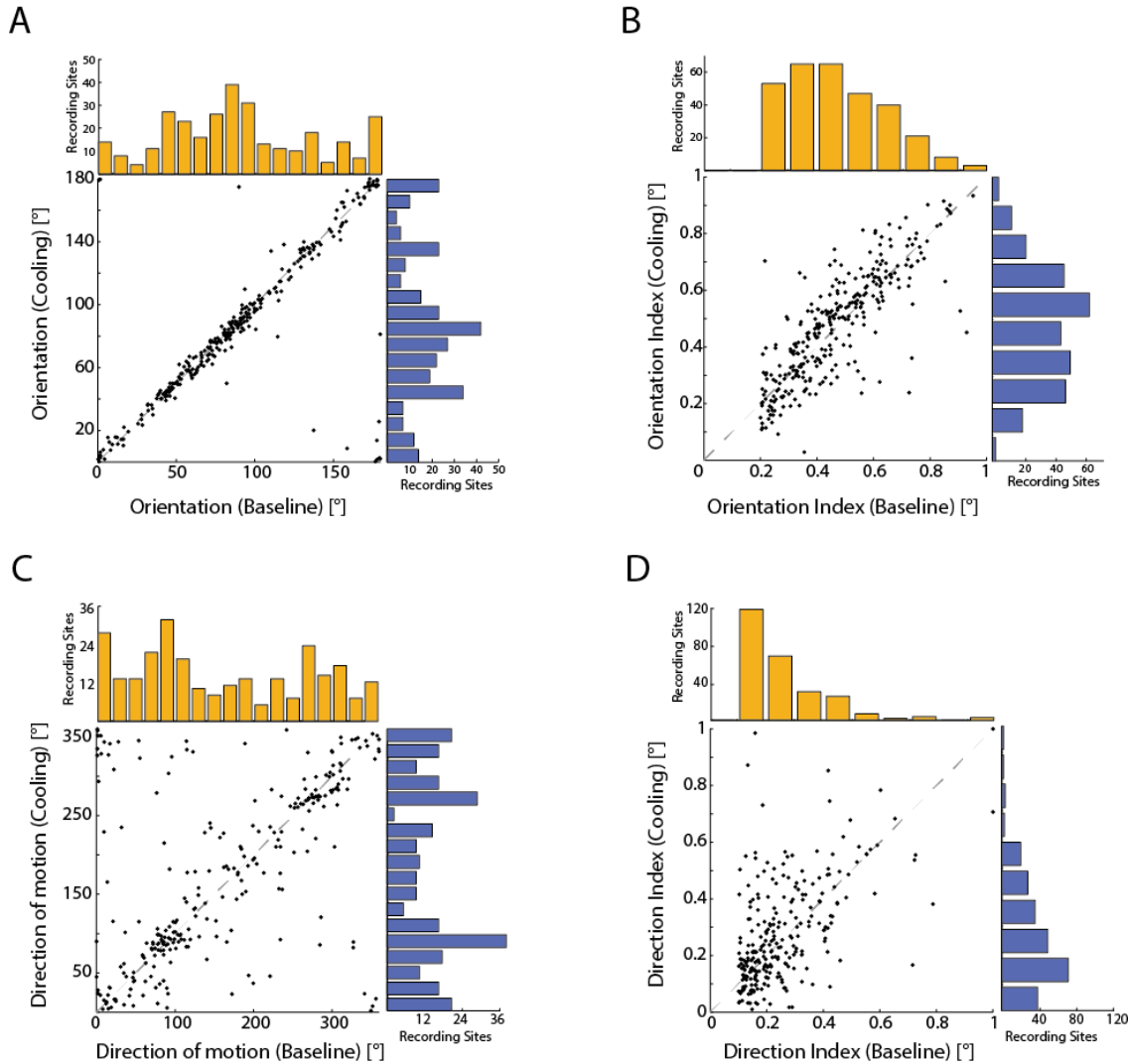


**Figure 24. Orientation and direction of motion preferences.** Bars represent the number of recording sites during baseline (orange) and cooling (blue). Dashed gray lines correspond to line  $x=y$  (A) Orientation preference. (B) Orientation index. (C) Direction of motion preference. (D) Direction index.

Removal of interhemispheric input did not affect the distribution of orientation indices or preferences. The preferences during baseline point out a bias towards orientations around 90 degrees in our multi-unit sample that was maintained during cooling. The mean orientation index during cooling was  $0.46 (+/- 0.19 \text{ SD})$ . The sparse distribution of orientation preferences in Figure 24A, as opposed to orientation indices in Figure 24B, (i.e. less concentrated around line  $x=y$ ) indicates that IHCs can slightly modify the tuning strength to preferred conditions, yet without changing the preference.

## 5. Results

### 5.2 Raw Responses

As expected for the areas we are recording from, our sample was less selective to direction of motion than to orientation. The data distributions in Figure 24C and D suggest a higher influence of interhemispheric connectivity on direction selectivity than on orientation selectivity but changes in direction of motion parameters were also not significant.

These results are in line with previous reports stating that orientation and direction selectivity examined with gratings do not change drastically in the absence of interhemispheric input and that direction selectivity is –if at all– stronger influenced (Schmidt et al., 2010; Wunderle et al., 2013)

#### 5.2. Raw Responses

We first computed the mean firing rates to the WF and Patch configuration and the LFP power from Alpha, LG and HG bands. For grating stimulation, Figure 25 illustrates representative examples where differences between responses to WF and Patch conditions were present. Figure 25A and B depicts the PSD and PSTH of the responses obtained from the same recording site where more LFP power and firing rate were evoked during Patch stimulation in comparison with WF. Although in this example the differences between these responses clearly point out a favoring of the Patch configuration, a considerable number of recording sites showed the contrary relationship as demonstrated in the PSTH from a different recording site in Figure 25C. The absence of interhemispheric input reduced the difference between the LFP power evoked by the two stimulus configurations, particularly in the LG range (Figure 25A, middle). Interestingly, the deactivation of IHCs affected more the responses to Patch stimulation (red traces in Figure 25B,C) in comparison to WF stimulation (green traces in Figure 25B,C).

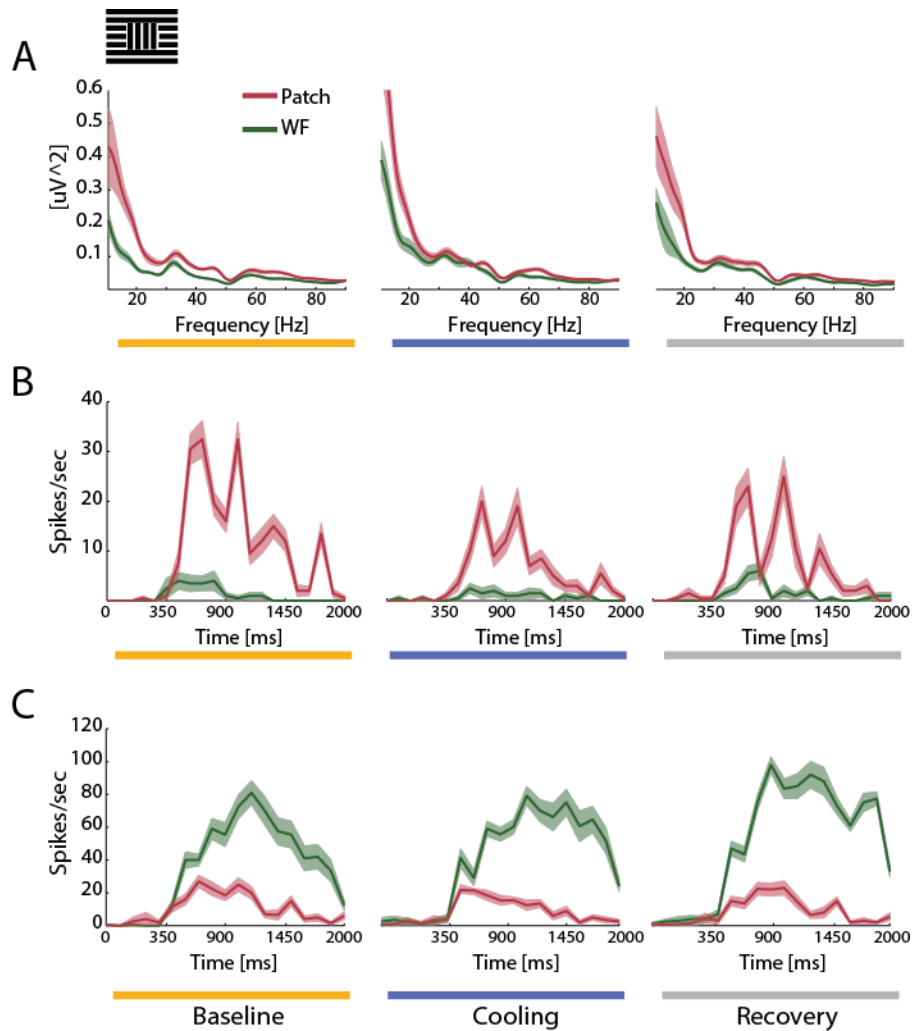


**Figure 25. Representative examples of responses to preferred condition during grating stimulation.** (A) Mean power spectrum density (B,C) Mean peri-stimulus time histograms (PSTH). All plots depict responses to Patch (red) and WF (green) stimulation during baseline (orange), cooling (blue) and recovery (grey). (B) Response facilitated by Patch stimulation. (C) Response suppressed by Patch stimulation. Note that the facilitated response was more affected in the absence of interhemispheric input than the suppressed response. Shaded represent standard error.

On average, we found that Patch conditions evoked less spikes than WF conditions during baseline (paired T test  $p<0.05$ ) and cooling (paired T test  $p<10^{-3}$ ) (see Figure 26C). In contrast, the power of Alpha and LG bands was lower during WF stimulation in comparison to Patch stimulation (paired T test  $p<10^{-3}$ , Figure 26D and  $p<0.05$ , Figure 26E respectively) during baseline. Noteworthy, only the LG's power difference between WF and Patch stimulation was lost after deactivation of IHCs.

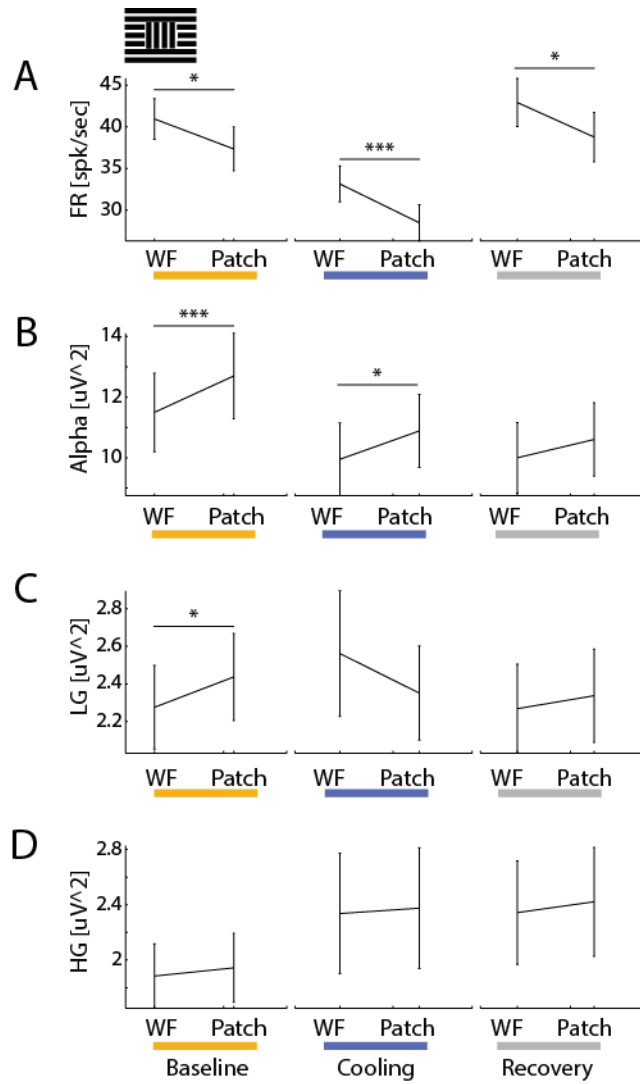


**Figure 26. Grating stimulation.** Averaged responses ( $n=205$ ) to preferred whole-field (WF) and Patch conditions during baseline (orange), cooling (blue) and recovery (gray). (A) Mean firing rates for 205 multi-units. (B) Mean Alpha power. (C) Mean Low Gamma power. (D) Mean High Gamma power. Statistical test: paired T-test (\*) significance level  $p<0.05$ ; (\*\*\*) significance level  $p<10^{-3}$ . Note that the relation between WF and Patch response almost reverses in the absence of IHC input for the LG band.

For natural scene stimulation, the difference between the responses to Patch and WF stimulus was clearer in the firing rate in comparison with PSD responses as depicted in Figure 28. However, in some cases we noted a rebound effect during recovery mainly for responses to the Patch stimulus (Figure 27A, right). This indirectly supports the notion that the manipulation of IHCs affects the processing of that kind of stimulus configuration. In the same way as described for grating stimulation, we identified a group of recording sites where Patch stimulation resulted in higher firing rate (Figure 28B) and also another group where this difference was inverted (Figure 27C).

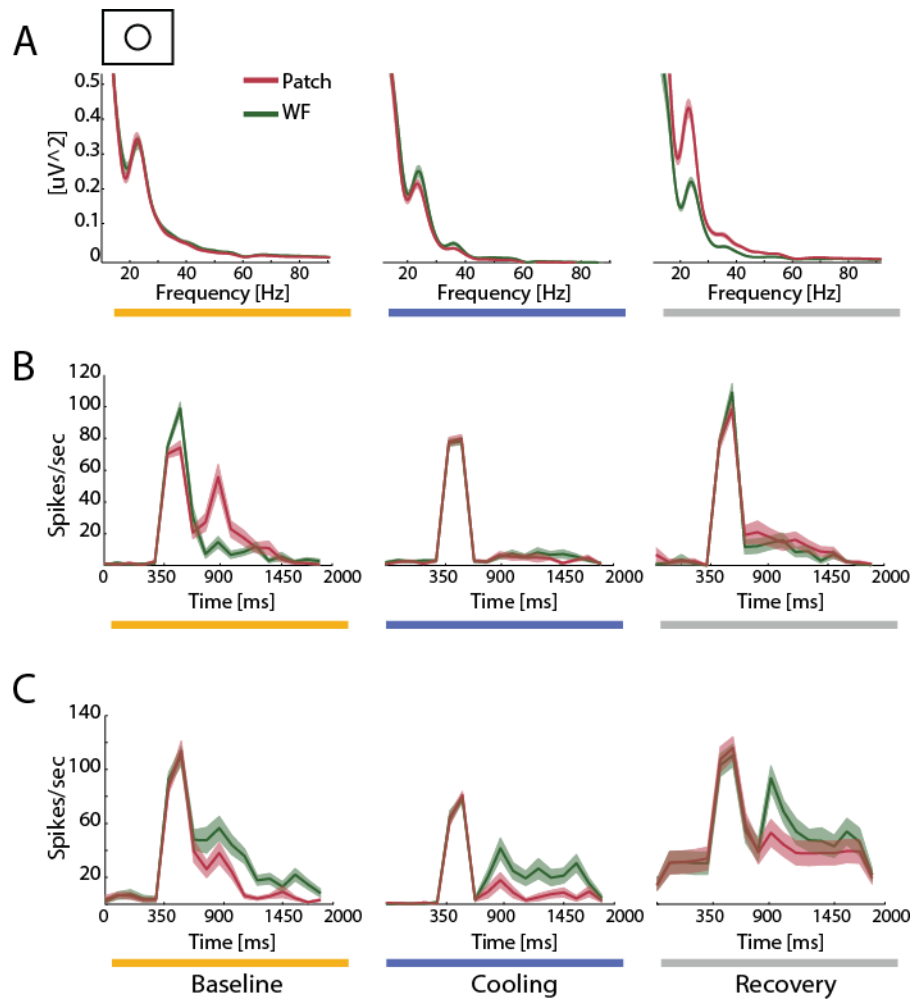


**Figure 27. Representative examples of responses to preferred condition during natural scene stimulation.** (A) Power spectrum density. Note the rebound of Patch gamma activity in the recovery. (B,C) Mean peri-stimulus time histograms (PSTH). Conventions as in Figure 26. (B) Response facilitated by Patch stimulation. (C) Response suppressed by Patch stimulation. Note that the facilitated response was more affected in the absence of interhemispheric input than the suppressed response. Shaded represent standard error.

On average, during baseline (Figure 28) we only observed differences in firing rates for WF and Patch (paired T test  $p<10^{-3}$ ). Here, the power differences observed for LFPs obtained with the two different grating stimuli above were not present. Yet, during the deactivation of IHCs, both firing rates as well as Alpha and LG power were lower for Patch conditions (paired T test  $p<10^{-3}$ ) similar to the result obtained with gratings.

Interestingly, this difference remained significant for the LG band even after the deactivation had been discontinued (Figure 28D). This is in line with earlier unpublished results that LFP changes induced by cooling deactivation do not always reverse to baseline

## 5. Results

### 5.3 Segmentation and Cooling Indexes

levels but can lead to yet another activation state (Wunderle, Schmidt, personal communication)

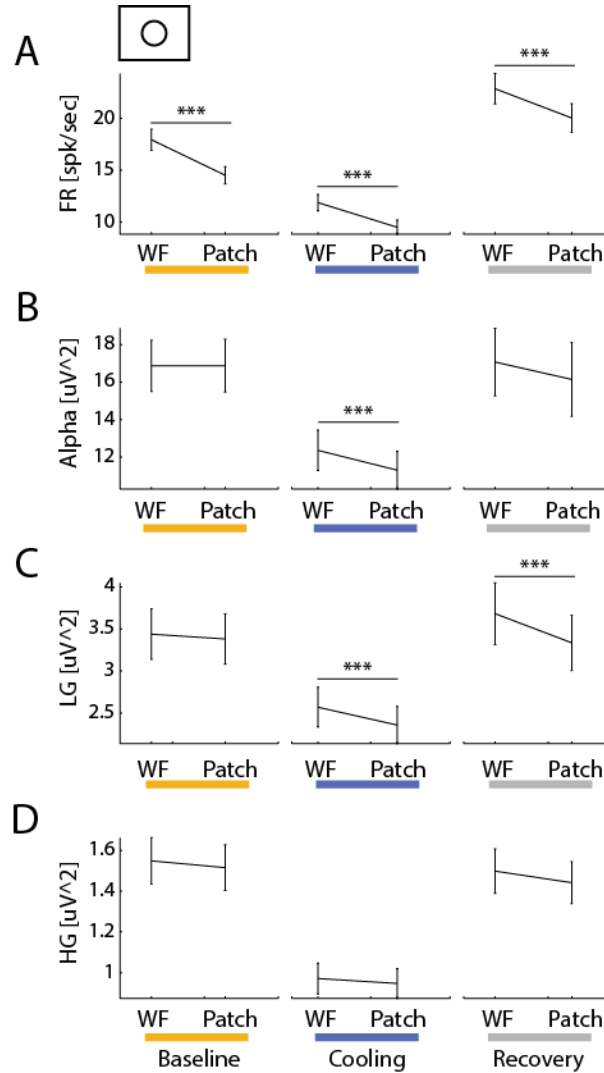


**Figure 28. Natural scene stimulation.** Averaged responses ( $n=184$ ) to preferred whole-field (WF) and Patch conditions during baseline (orange), Cooling (blue) and Recovery (gray). (A) Firing rates. (B) Alpha's power. (C) Low Gamma's power. (D) High Gamma's power. Statistical test: paired T-test (\*\*\*): significance level  $p<10^{-3}$ . Note that LFP power differences between WF and Patch stimulation are not present in the baseline but are disclosed by deactivation of IHCs and are maintained in the recovery period (significant for the LG band)

### 5.3. Segmentation and Cooling Indices for firing rates and LFPs

We defined the SI in order to quantify the differences between the responses to WF and Patch conditions as a measure of response suppression by the iso versus cross- oriented surround (i.e. figure-ground segmentation). In addition, we also defined the CI to measure

## 5. Results

### 5.3 Segmentation and Cooling Indexes

the IHCs deactivation effects separately on the two conditions, Patch (cross-oriented) and WF (iso-oriented) (see Equation 5 and 6 in Methods, section 4.7.2).

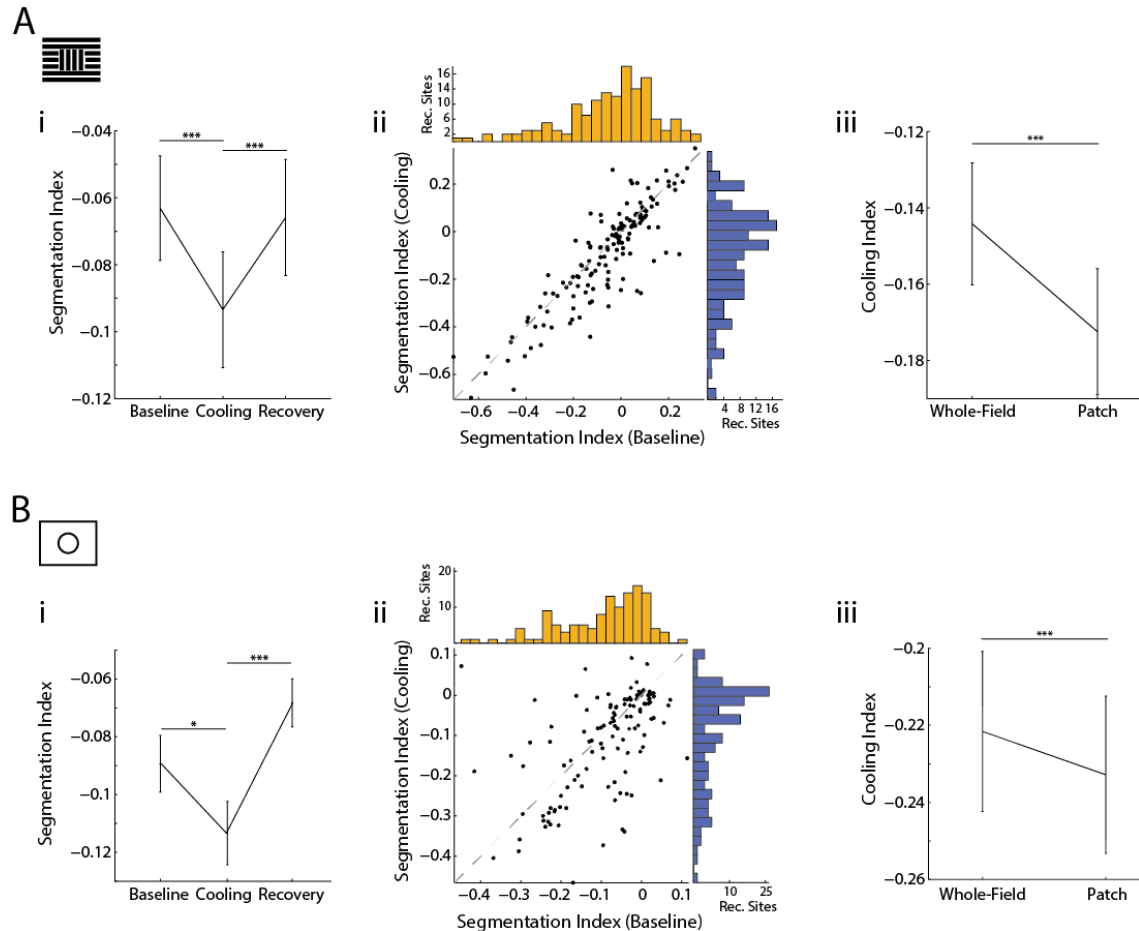


**Figure 29. Segmentation and cooling indices of firing rates.** (A) Results from grating stimulation (i) Averaged segmentation index of the same set of recording sites ( $n=205$ ) during baseline, cooling and recovering. (ii) Segmentation index correlation plots and histograms for the individual recording sites during baseline (orange) and cooling (blue). In the correlation plot, each point represents one recording site. (iii) Cooling index from responses to WF and Patch stimulation of the same set of recording sites. (B) Results from natural scenes stimulation. (i) (ii) and (iii) as in (A). All bars represent the mean +/- standard error of each distribution. Statistical test: paired T-test. (\*\*\*): significance level  $p<10^{-3}$ . Rec. Sites stands for recording sites.

We first considered the firing rates from each recording site as response to stimulation with gratings. The negative value of SI during Baseline (Figure 29Ai) showed that, on average, Patch conditions evoked less spikes than WF, indicating higher response suppression by orthogonal surround when compared to iso-oriented surround. This difference between Patch and WF responses significantly increased during cooling leading to an even more negative SI (paired T-test,  $p<10^{-3}$  Figure 29Ai). This points to even more

## 5. Results

### 5.3 Segmentation and Cooling Indexes

suppression or less excitation for the Patch as opposed to the WF condition in the absence of interhemispheric input. The analysis of CI revealed that, on average, the effect of IHCs deactivation was more accentuated on Patch responses than on WF responses (firing rate mean reduction of 23.7% and 19.02% respectively, Figure 29Aiii, paired T-test,  $p < 10^{-3}$ ). This explains the SI variation depicted on Figure 29A and indicates that the decrease of the SI is a result of a higher loss of excitation for the Patch than for the WF condition when removing IHCs.

Despite that on average (negative SI in Figure 29i), the firing rate for iso-oriented surround (i.e. WF) was slightly higher than the firing rate for orthogonal surround (i.e. Patch), the histogram in Figure 29Aii reveals that during baseline the contrary is also frequent, resulting in a nearly symmetric distribution of SI values (orange; 55% of negative SI and 45% of positive SI). The plot in Figure 29Aii also points out that there is tendency of recording sites with negative SI during baseline to be more affected by deactivation of IHCs. Figure 29B demonstrates the SI and CI results from natural scene stimulation. Overall tendencies are similar to grating stimulation (compare Figure 29A). Firing rates are on average higher for WF stimulation, i.e. iso-oriented surround, than for Patch stimulation, i.e. cross-directed surround movement. Deactivation of the contralateral hemispheres enhances that tendency mainly by removing more spikes for stimulation with the Patch than with WF condition (firing rate mean reduction of 34.8% and 33.7% respectively). However, overall, the SI and CI decreases are stronger for that stimulus category than with gratings. This goes along with an earlier observation that responses to stimuli which are less salient than gratings reveal more integration by the lateral networks and thus predominantly decrease their spike rates during deactivation of IHCs (Wunderle et al., 2013).

We next considered the power of Alpha, LG and HG frequency bands. Computation of SI indices for grating stimulation revealed, on average, more power in Alpha and LG bands for Patch as compared to WF conditions, during baseline (positive SI in Figure 30Ai, Bi and Ci). This in contrast to the average negative SI indices observed with firing rates Figure 29) but one should note that average SI indices are rather small in all cases as confirmed by the histograms (Figure 29ii, 28ii, 29ii) of the individual SI indices showing that facilitative and suppressive effects are quite balanced in our sample.

Whereas the positive Alpha band index was maintained during cooling, the SI of LG and HG significantly decreased, reaching negative values. This indicates that after deactivation of IHCs, the gamma band power evoked by Patch was lower than that evoked by WF conditions. The SI's changes are in concordance with CI's changes (Figure 30Biii and Figure 30Ciii) demonstrating that -as with firing rates- LFP power evoked by Patch conditions decreased more during deactivation of the IHCs than those to WF conditions.

## 5. Results

### 5.3 Segmentation and Cooling Indexes

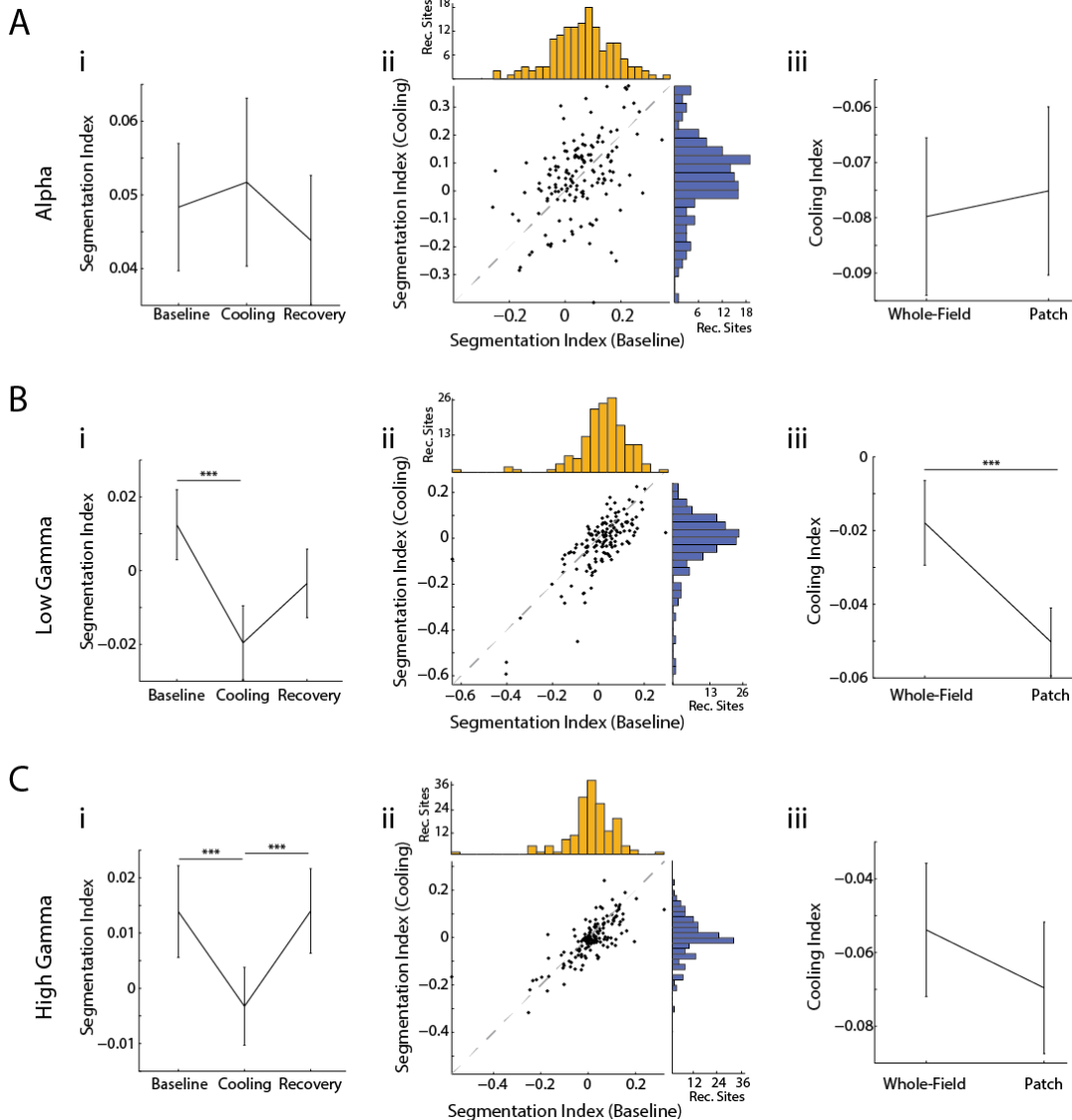


**Figure 30. Segmentation and cooling indexes of LFP's power for grating stimulation.** Results in the Alpha (A), LG (B) and HG (C) band from grating stimulation. Conventions as in Figure 29.

We repeated the analysis considering the LFP responses obtained by stimulation with natural scenes (Figure 31). Here, the average power evoked for Patch conditions started slightly lower than for WF conditions during baseline, and this trend was even enhanced in the absence of interhemispheric input for all LFP's rhythms (Figure 31Ai; Bi and Ci) following the same tendency as observed to gratings, with the result of a more negative SI during cooling. In agreement, isolated power in these two LFP rhythms decreased also significantly more for Patch than for WF conditions as expressed by lower Patch CIs (Figure 31Aiii and Figure 31Biii).

## 5. Results

### 5.3 Segmentation and Cooling Indexes

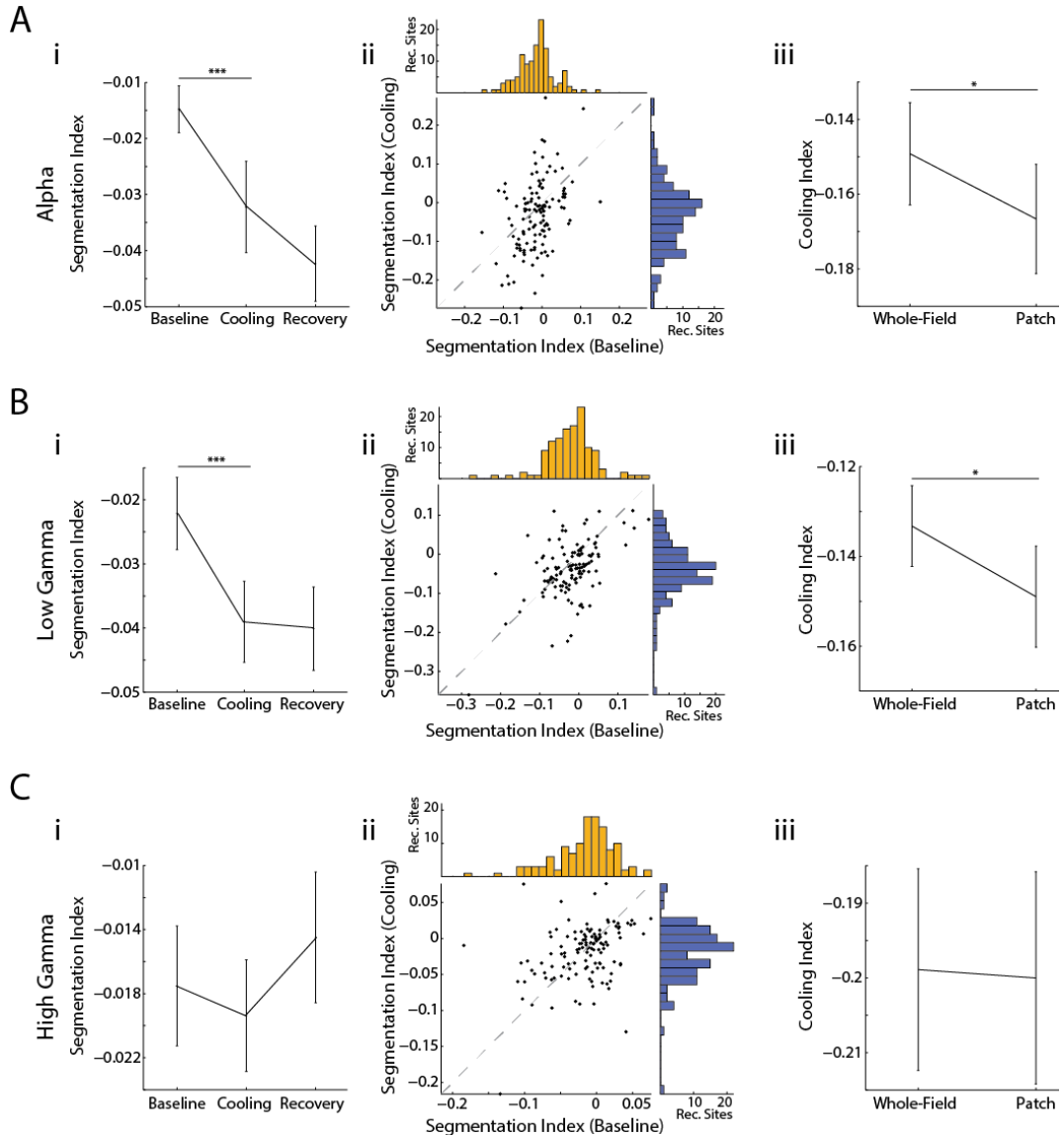


**Figure 31. Segmentation and cooling indexes of LFP's power for natural scene stimulation.**  
Conventions as in Figure 29.

Taken together, we observed that in a population of neurons located at the cat's 17/18 border responses to a “pop-out” patch condition tend to be lower than to a uniform whole-field stimulus. A “pop-out” in the sense of a bigger response to the Patch stimulus was only observed for LFP power in case of grating stimuli, but not for natural scene stimuli. Consistently for both stimulus types, the deactivation of IHCs affected the responses (either firing rates or LFP power at a given frequency band) to Patch more than WF conditions as indicated by a decreasing SI during cooling. This possibly indicates that responses to a defined figure-ground stimulus benefit more from an intact interhemispheric input than responses to uniform stimuli.

## 5. Results Characterization

### 5.4 Assemblies Detection and

Interestingly, we observed that for that stimulus category, the SI had a tendency to fall in function of the frequency increase of the considered response.

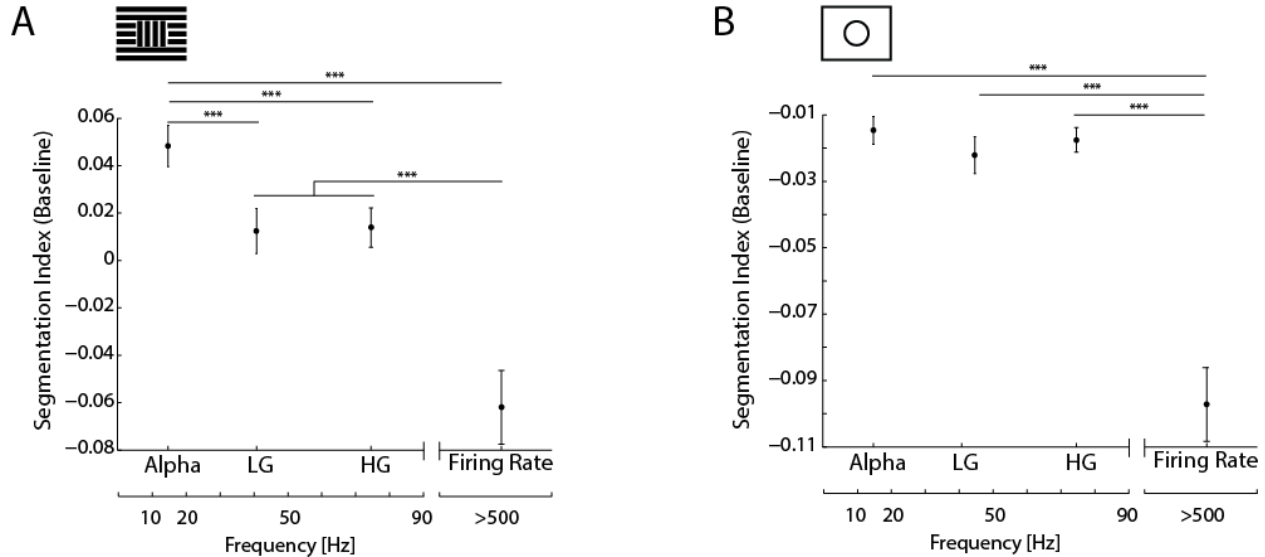


**Figure 32. Variation of segmentation index in function of the response's frequency.** During the presentation of gratings (A) and natural scenes (B). LG: Low Gamma. HG: High Gamma. Statistical test: T-test (\*\*\*\*) significance level  $p<10^{-3}$ .

### 5.4. Assembly Detection and Characterization

The above results so far are compatible with the interpretation that figure-ground segmentation involves also other mechanisms than a mere generalized increase or decrease of firing rates or LFP's power in primary visual cortex. In fact, other studies showed that synchrony processes at single unit or LFP levels (Biederlack et al., 2006; Gail et al., 2000) can also play an important role for figure-ground segmentation. In order to define an approach that examines the population activity of the in parallel recorded neurons focusing on the foreground patch we evaluated the activity of neuronal assemblies. Aiming to characterize these assemblies we followed a similar analysis described for individual recording sites. As a first step, we computed an extended version of the CRF mapping in order to identify that part of the visual field which could strongly influence the activity of each assembly (i.e. the joint receptive field -JRF- formed by the CRFs of the more active -highly weighted- neurons in the assembly).

For each assembly pattern, we constructed  $N$  two-dimensional Gaussians ( $N$ = number of neurons), centered at the CRF of each neuron, with standard deviation equal to the area of its CRFs and an amplitude equal to the neuron's weight in the pattern. The JRF is defined as the mean of all Gaussians and is centered at its maximum value (Figure 33). Depending on the JRF center's location, we classified the assembly as figure-driven or ground-driven.

## 5. Results Characterization

### 5.4 Assemblies Detection and

Table 2 presents general information about the assemblies detected during grating and natural scene stimulation.

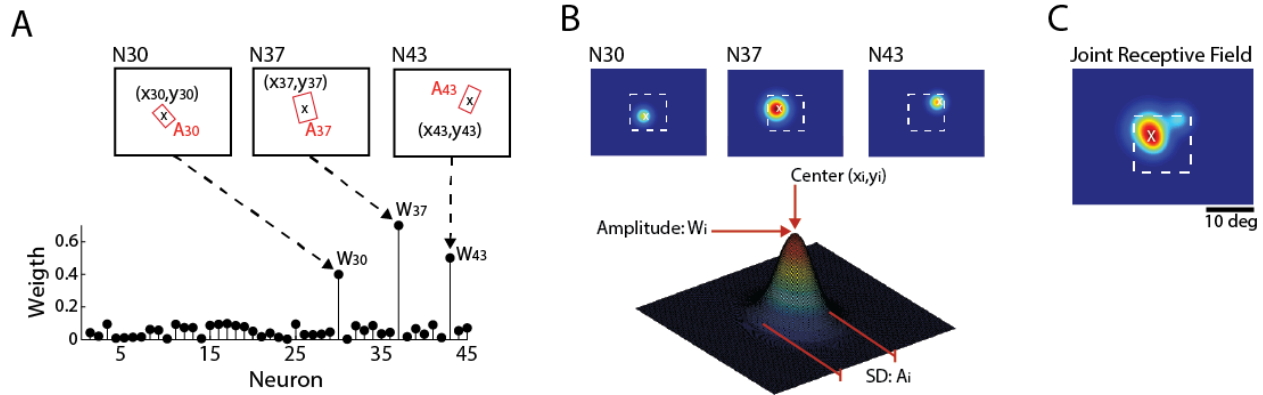


**Figure 33. Joint receptive field computation.** (A) Upper row: Receptive fields (red rectangles) of three neurons belonging to the assembly pattern at the bottom. Here, for a matter of visualization, we only depict the CRF for those neurons, however the calculations were performed for all units. (B) Based on the center of the receptive field of a given unit  $i$  ( $x_i, y_i$ ) and its area  $A_i$ , we constructed a two-dimensional Gaussian centered at  $(x_i, y_i)$ , with standard deviation  $A_i$  and amplitude  $W_i$  equal to the neuron's weight in the assembly. (C) The joint receptive field (JRF) by calculating the mean of the Gaussians obtained in B. Depending on the location of its center (white x), we classify the assembly as figure-driven or ground-driven.

**Table 2.** Assemblies' characterization.

Stimulus	Neurons per recording site	Neurons per data set [min max]	Assemblies per data set	Figure-driven assemblies	Ground-driven assemblies
Grating	1.47	[22 60]	9.33	100	60
Natural Scene	1.84	[38 60]	11.1	60	51

Since we identified the activation times (and thus, the number of activations) during the presentation of each condition of gratings stimuli (see Figure 20 in Methods section), we could characterize each assembly in terms of its orientation and direction of motion preferences by the calculation of the direction and orientation indices (Figure 34). Based on these parameters, we considered only figure-driven assemblies with an orientation index higher than 0.2 for all further analysis regarding grating stimulation ( $n=76$ ).

The same approach was not possible for natural scene stimulation because the lack of a specific stimulus orientation and the low resolution of direction of motion (only cardinal

## 5. Results Characterization

### 5.4 Assemblies Detection and

directions). Instead, we identified the preferred of all the four WF conditions, and selected figure-driven assemblies and their response to that preferred condition.

Assemblies observed with grating stimulation revealed a clear preference for one of the four orientations presented with the stimulus, rather than being distributed across all possible interpolated orientations (Figure 34A). We also noticed a slight bias to the vertical orientation. This was to be expected considering that this bias was already present in the orientation preference distribution of the individual recording sites (see Figure 24). Deactivations of IHCs did not affect significantly the orientation preference of the assemblies; however, it significantly increased their orientation index (paired t-test,  $p=0.009$ , Figure 34B)

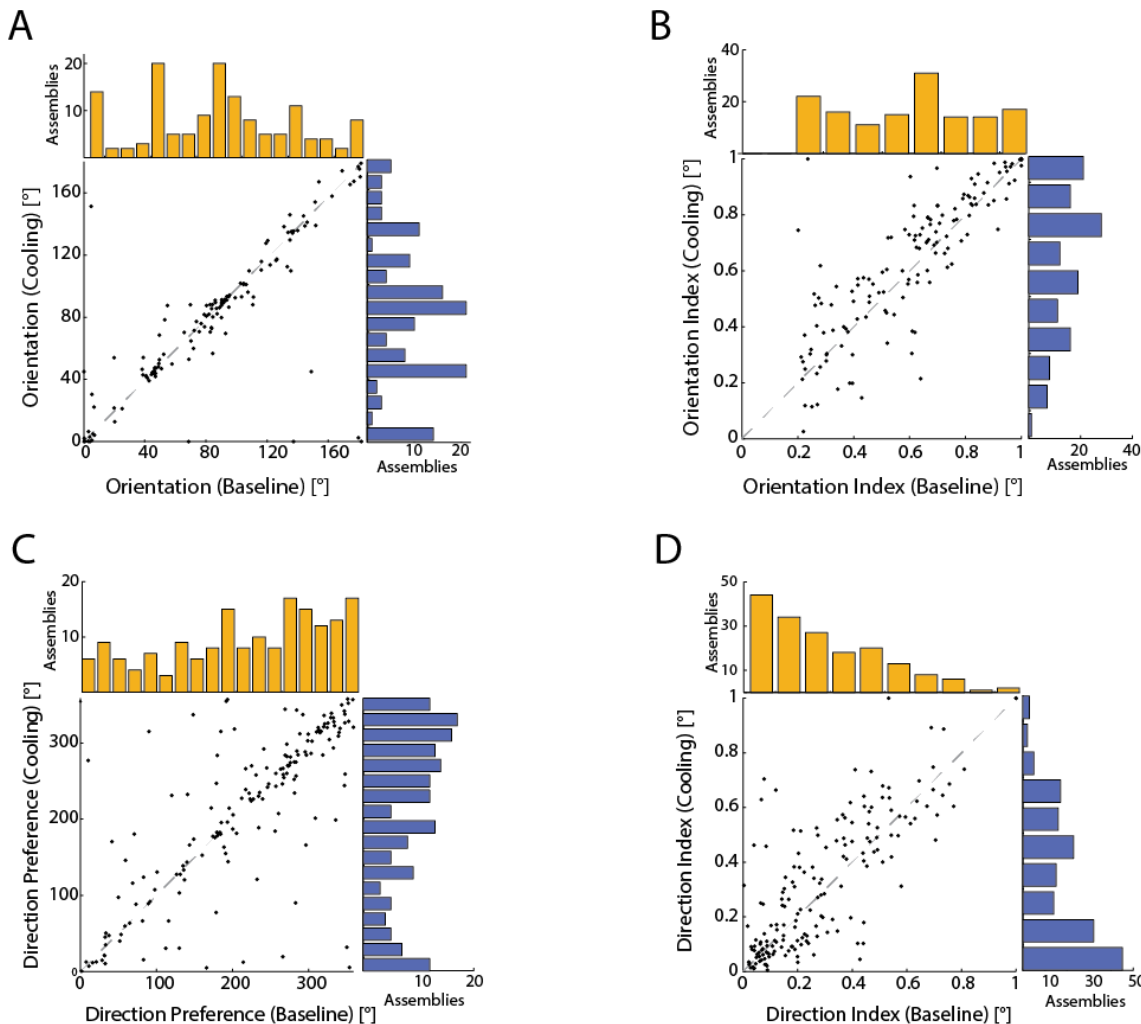


**Figure 34 Assembly preferences during grating stimulation.** The number of assemblies during baseline (orange) is compared to the number of assemblies during cooling (blues). The traced gray

## 5. Results

### 5.5 Segmentation and Cooling Indexes (Assembly case)

line corresponds to  $x=y$  (A) Orientation preference. (B) Orientation index. (C) Direction of motion preference. (D) Direction index

For the assembly direction preference similar results were obtained. However the data distribution in Figure 34C suggests that – as observed for single cells above- assembly direction preferences were more sensitive to IHCs deactivation than orientation preferences. Averaged direction indices increased during cooling (paired t-test,  $p=0.012$ , Figure 34D).

In order to compare the orientation preferences of assemblies and individual neurons we computed the difference between those parameters as a function of the neuron's weight in the assembly. We expected to find similar preferences between high-weighted neurons and the assembly; however, that was not always the case (Figure 35). The result, considering only the top 25% high-weighted neurons of each assembly, pointed out that it is possible to find neurons even with orthogonal preferences participating in the assembly, although 90% of the neurons differed only around 55 degrees from each other (percentile 5=-61.3°, percentile 95=51.97°).

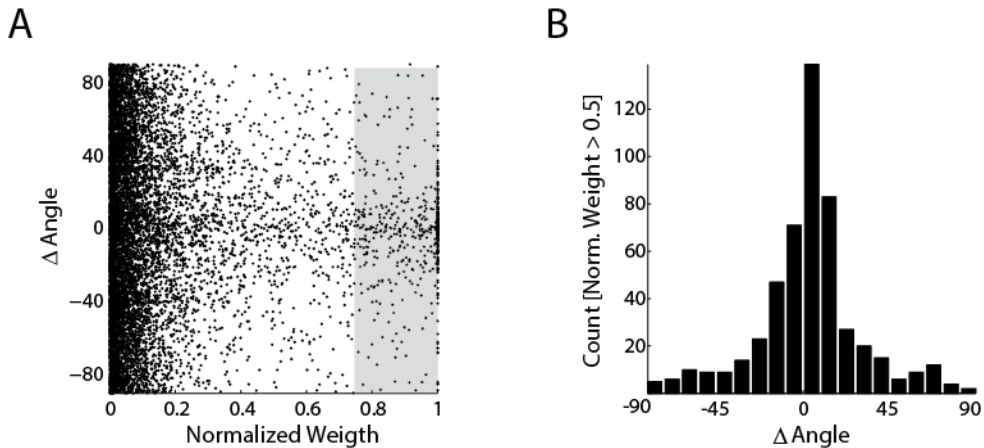


**Figure 35. Comparison between neurons and assemblies preferences** (A) Difference between the neuron's and assembly's preferred orientations as a function of neuron's normalized weight. Despite an expected tendency to have similar orientation preferences between the assembly and highly-weighted neurons, note that there is also highly-weighted neurons with different individual preferences. (B) Histogram of differences between assembly and individual orientation preferences considering the higher 25% weighted cells.

### 5.5. Segmentation and Cooling Indices for Assemblies

We calculated the cumulative number of activations of each assembly during baseline, cooling and recovery. This allowed us to identify the presence of four main assembly

## 5. Results

### 5.5 Segmentation and Cooling Indexes (Assembly case)

groups: a first group, that reduced the number of activations during cooling and recovered to baseline levels, a second group, that increased its activations during cooling and returned during the recovery, a third group, that despite being active in the baseline, lost its activity during cooling and did not recover it, and finally a fourth group, that was not active during baseline, yet gained activity during cooling or only in the recovery. We considered only the first two groups with recovery for all further analysis.

**Table 3.** Number of assemblies in the four groups defined by activity during baseline, cooling and recovery.

	Group 1	Group 2	Group 3	Group 4
Gratings	45	8	3	20
Natural scene	37	11	3	9

We computed the mean number of activations of each assembly during the presentation of its preferred stimulus' condition. The results showed that for both stimulus categories (gratings and natural scenes) the Patch conditions evoked less assembly activity than WF conditions during baseline ( $p<0.05$  for both categories), indicating iso-orientation facilitation by the uniform as compared to the contrasting surround (Figure 36).

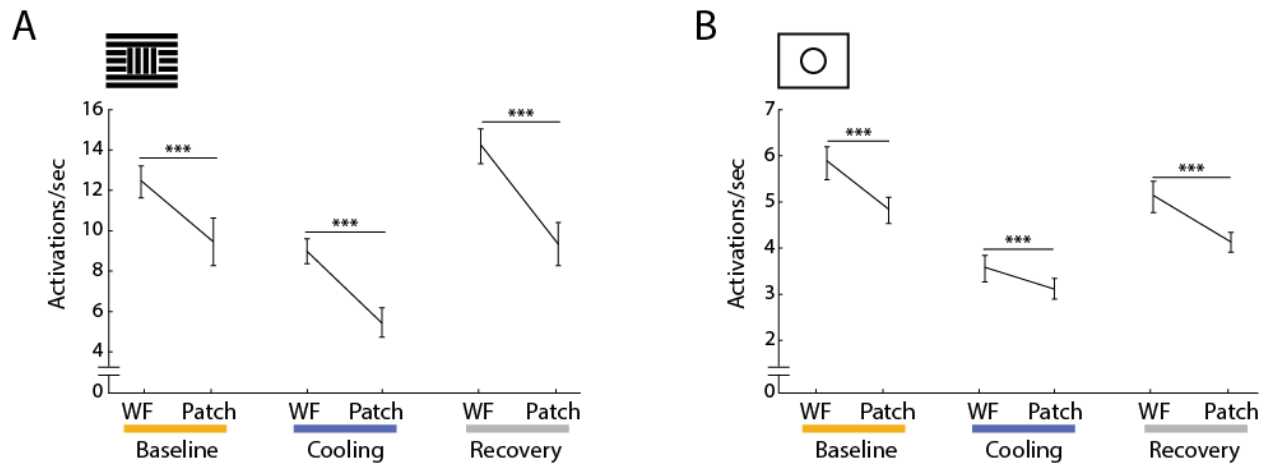


**Figure 36. Number of assembly activations per presentation of the preferred condition.** (A) gratings and (B) natural scene stimulation. Statistics: paired T-tests; significance level  $p<10^{-3}$  (\*\*\*)

However, during IHC deactivation, the number of activations was reduced regardless of the stimulus category. Note that for grating stimulation the re-activation of IHCs (recovery period) increased the number of assembly activations as compared to baseline levels, i.e. there occurred an activity rebound which is occasionally observed with gratings.

The above described changes in average assembly activation were reflected in the segmentation indices. As for both, grating and natural scene stimulation, the number of

activations evoked by Patch was lower than WF conditions, SI values during baseline were negative (Figure 37A, B). For grating stimulation this relationship was maintained during cooling, demonstrated by the SI's invariance. In contrast, for natural scenes stimulation the SI increased thus shifting closer to zero during IHCs deactivation (paired T-test,  $p<10^{-3}$ ), indicating a smaller difference in the number of activations evoked by the two stimulus conditions. In this case, the CI revealed a tendency of WF responses to be more affected than Patch conditions, however this difference did not reach statistical significance ( $p=0.63$ ).

For both gratings and natural scenes, the CI indicated that the number of assembly activations decreased equally for both WF and Patch conditions (negative CI values without significant differences for both stimulus categories, see lower plots, Figure 37A, B).

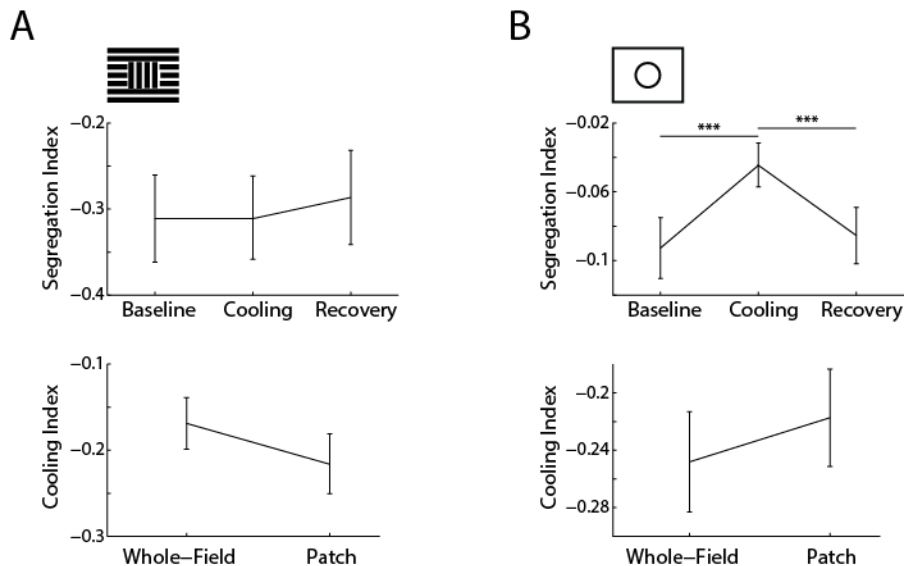


**Figure 37. Cooling and segmentation indexes based on number of assembly's activations.** Stimulation with (A) gratings and (B) natural scenes. Statistic: paired T-test; (\*\*\*) significance level  $p<10^{-3}$

In summary, the population analysis did not reveal a different effect of contralateral deactivation for (grating) Patch or WF conditions. Rather, the assemblies seem to have lost response gain by a similar factor for both condition types during cooling as indicated by a similar SI for baseline and cooling and similar CIs for Patch and WF (Figure 37A). This is surprising and in contrast to the results obtained for single cells in the previous chapters. Therefore, we will examine the temporal relationship between a spiking event or an assembly event and the local field potentials of the participating neurons in the next chapter.

## 5.6. Phase Locking

At the end of section 5.3 (Figure 32) we compared cooling effects on spiking and LFP activity but so far, we did not make any attempt to examine the relationship between the two. However, it is very likely that lateral connectivity is involved in modulating that relationship and that this relationship is also stimulus-dependent, i.e. different for figure-ground (Patch) and uniform (WF) stimuli.

We aimed to first evaluate if there was a relation between the spiking times from individual neurons and the phase of the LFP rhythms Alpha, LG and HG (phase locking). For cases where this relation was significant (Rayleigh uniformity test) we quantified the strength of the phase locking by calculating the *kappa* value of the Von Mises distribution. This parameter indicates how narrow the distribution is, with an increase of *kappa* indicating a distribution narrowing, and thus a stronger phase locking (for details see Methods, Section 4.7.4). Secondly, we repeated this analysis for the population approach by considering the activation times of the assemblies.

### 5.6.1. Single Cell and Assembly Phase-Locking with Grating Stimulation

In general, the results indicated an overall increase of assemblies' phase locking after deactivation of IHCs for all rhythms (paired T-test  $p < 10^{-3}$ ). This was not the case for single cell phase locking except for the Alpha range.

In order to identify if phase locking was related to figure-ground segmentation, we separated the responses to WF and Patch conditions. In the case of grating stimulation, the results revealed differences between the two in the strength of phase locking of single neurons during baseline. Single neurons were more locked to Alpha and LG phases when stimulated to WF in comparison with Patch conditions. The contrary occurred in HG (Figure 38A, orange). The deactivation of IHCs inverted this difference from Alpha and HG rhythms and eliminated it from LG (Figure 38A, blue).

Contrary to the single neuron results, the assemblies were more phase locked to Alpha and LG for the Patch than to the WF condition during baseline (Figure 38B, orange; paired T-test,  $p < 0.05$ ). This difference was maintained during the absence of interhemispheric input for LG phase relationships (Figure 38B, blue; paired T-test,  $p < 0.05$ ).

## 5. Results

## 5.6 Phase Locking

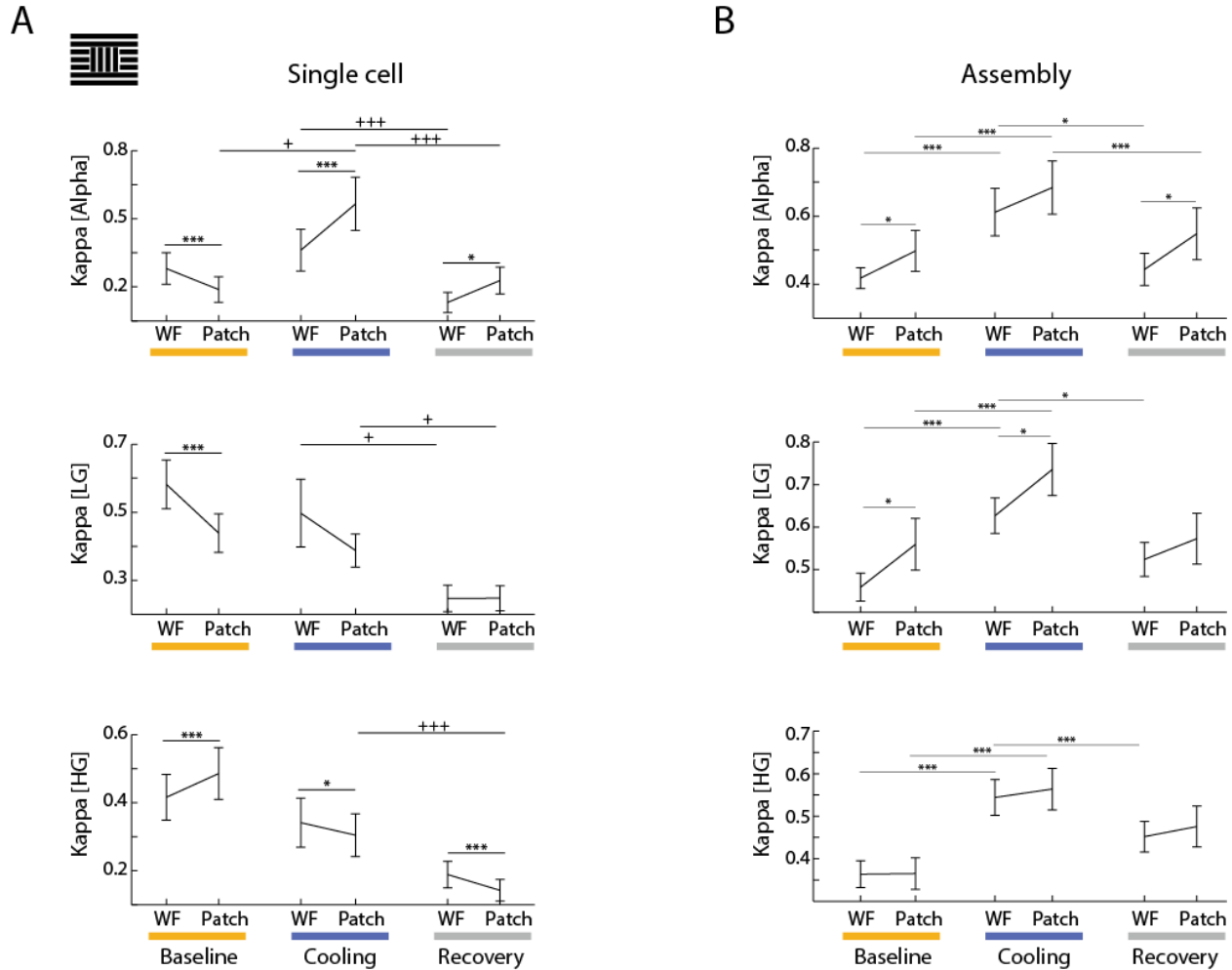


**Figure 38. Kappa values during gratings stimulation.** Single neuron (A) and assembly levels (B). The phase locking was evaluated during baseline (orange), cooling (blue) and recovery (gray) for Alpha (top), Low Gamma (center) and High Gamma (bottom) rhythms. Statistic: paired T-test; (\*) significance level  $p<0.05$ ; (\*\*\*) significance level  $p<10^{-3}$ . Note that phase locking with Gamma rhythms decreases for single cells but increases for assemblies during IHC deactivation.

### 5.6.2. Single cell and assembly phase locking with natural scene stimulation

In contrast to grating stimulation, the results from natural scene stimulation revealed that during baseline, single neurons were more locked to Alpha for Patch than for WF conditions. The same neurons showed opposite results for LG and HG, where WF conditions resulted in higher *kappa* values (Figure 39A, orange). The deactivation of IHCs affected in particular the phase locking with LG, eliminating the difference between WF and Patch (Figure 39A, blue).

As for grating stimulation, natural scene assembly phase locking increased also during cooling. Although a tendency for stronger phase locking with Patch than WF stimulation

## 5. Results

## 5.6 Phase Locking

could be observed in all rhythms both during baseline and cooling, this difference reached significance only for the Alpha rhythm.

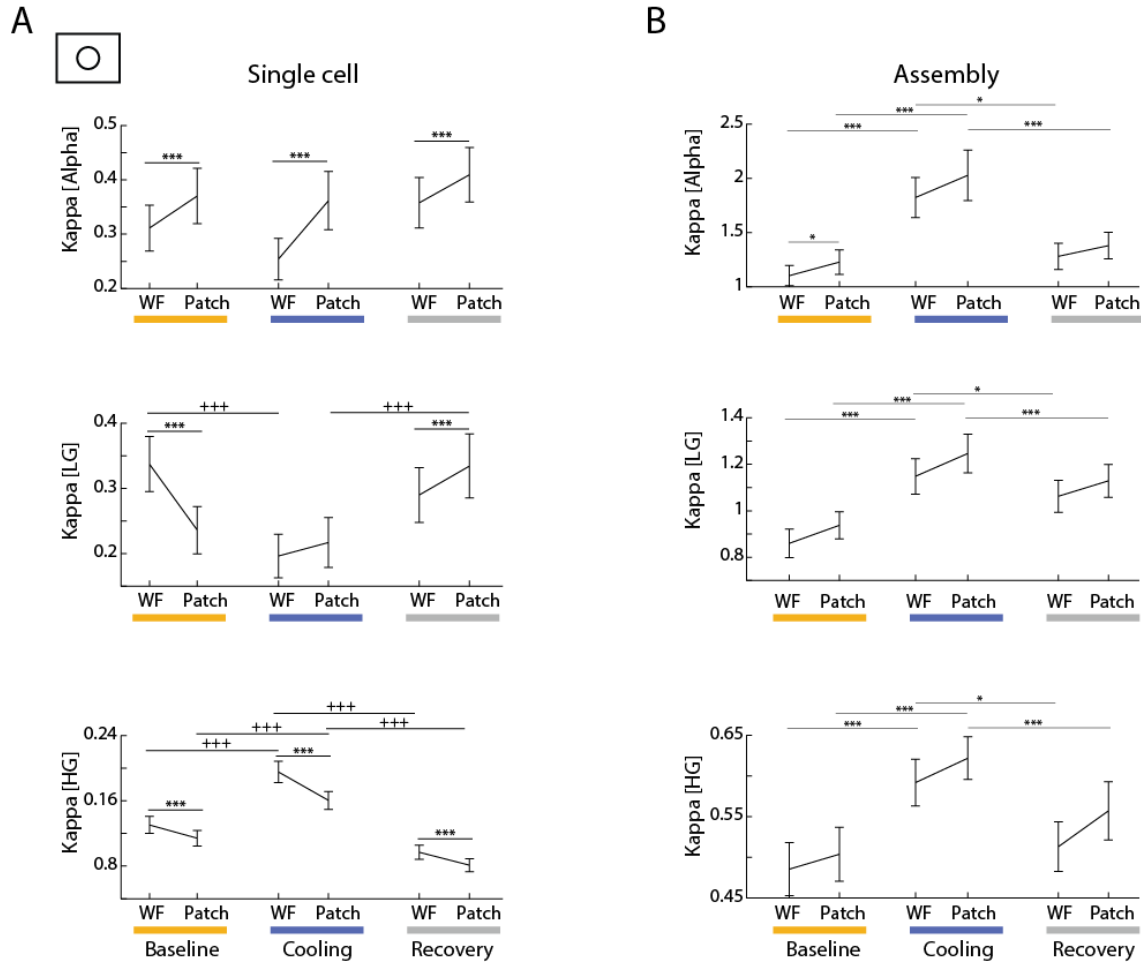


**Figure 39. Kappa values during natural scenes stimulation.** Center (patch) and surround move in orthogonal directions. Single neuron (A) and assembly levels (B). The phase locking was evaluated during baseline (orange) and cooling (blue) for Alpha (top), LG (center) and HG (bottom) rhythms. Statistic: paired T-test; (\*) significance level  $p < 0.05$ ; (\*\*\*) significance level  $p < 10^{-3}$

Based on this result, we considered the possibility that the motion contrast of 90 degrees between center and surround in the natural scenes was not sufficient to unveil a figure-ground segmentation mechanism in the anesthetized preparation (Kastner et al., 1997). Thus aiming to maximize the pop-out effect we modified the surround's direction to the counter direction of the center Patch direction (see Supplementary Figure 1B; conditions 9-12).

## 5. Results

### 5.6 Phase Locking

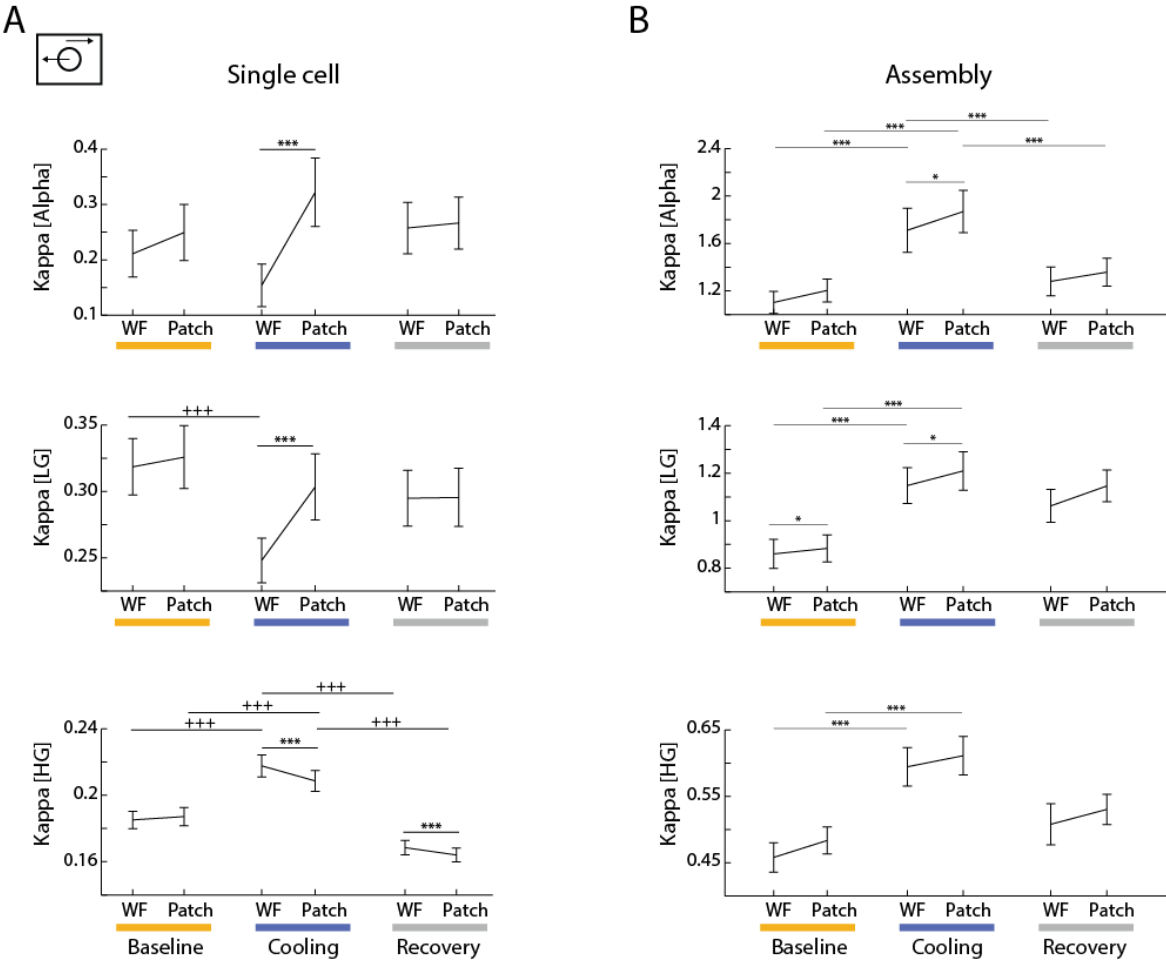


**Figure 40. Kappa values during natural scene stimulation.** Center (patch) and surround move in opposite directions. Single neuron (A) and assembly levels (B). The phase locking was evaluated during Baseline (orange), Cooling (blue) and Recovery (gray) for Alpha (top), LG (center) and HG (bottom) rhythms. Statistic: paired T-test; (\*) significance level  $p<0.05$ ; (\*\*\*) significance level  $p<10^{-3}$

The results for this new set of conditions pointed out *kappa* values similar to orthogonal movement contrast. However, as expected, the difference of phase locking between WF and Patch conditions was emphasized during cooling and reached now significance levels in the Alpha and LG ranges for both single cells and assemblies. Preliminary analyses of all responses including also the non-preferred conditions show even stronger *kappa* differences between Patch and WF conditions. This indicates that the separation of WF and Patch configurations becomes clearer for improved figure-ground contrasts (data not shown).

In general these results demonstrated that the surround stimulus influences the phase locking between spiking activity (i.e. single cells and assemblies) and LFP. When comparing single cell with assembly locking we noted that the phase locking of assemblies was more

## 5. Results

### 5.7 Coherence Variation during IHCs Deactivation

robust than that of single cells. This was reflected in higher  $\kappa$  values for assemblies than for single cells (mainly for natural scenes stimulation) and consistent differences between stimuli conditions (assemblies always more phase locked during Patch than during WF conditions) regardless of the stimulus category. In the absence of interhemispheric input, phase locking became stronger mainly independent of the stimulus condition and category indicated by an increase of  $\kappa$  by a certain factor.

#### 5.7. Coherence Variation during the Deactivation of IHCs

The rather uniform  $\kappa$  increase during cooling periods led us to consider the hypothesis that the deactivation of IHCs reduces the integration radius of LFP, transforming the LFP into a representation of a more restricted and local area. In that sense, a  $\kappa$  increase would not necessarily imply a higher precision of firing and a better system function, but instead it may reflect isolated functional islands within which LFPs and spiking activity are stronger coupled due to the absence of a large part of the lateral (interhemispheric) network.

A first step towards testing this hypothesis is to measure the variation of LFP-LFP coherence between electrodes as a function of distance. Considering coherence as an indicator of coordinated population activity, we would expect a coherence reduction for distant electrodes and an increase for those nearby if the removal of interhemispheric input in fact reduces the integration of activity.

Although the results were not strongly conclusive, they supported the hypothesis. In Figure 41, we present a representative example of the variation of coherence as a function of distance. Each point corresponds to the mean coherence of all pairs of electrodes at a given separation, taking the LFPs during the preferred stimulation with the grating stimulus. The lines are the linear fit for all points during baseline (orange) and cooling (blue).

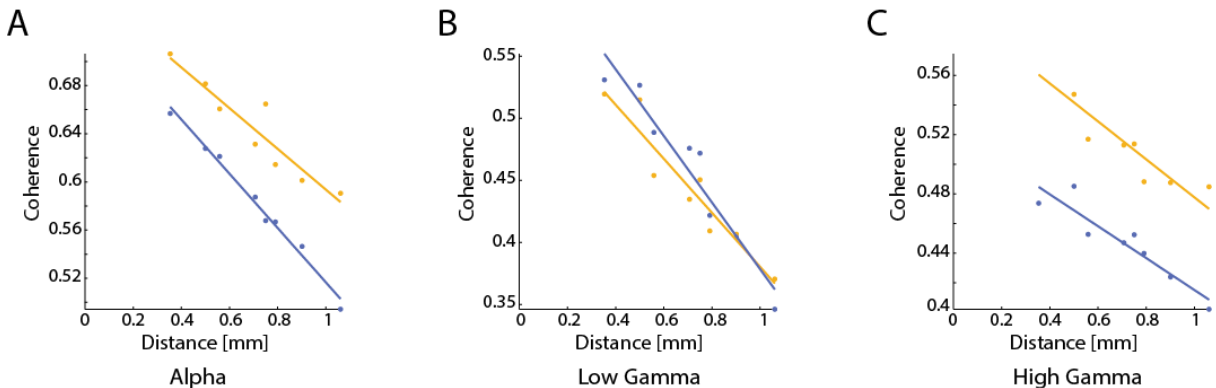


**Figure 41. Representative examples of coherence variation.** (A) Alpha (B) Low Gamma and (C) High Gamma as a function of distance (Dataset 10). Each point represents the mean coherence of all channel pairs at a given distance, during preferred orientation stimulation. Orange points represent

## 5. Results

### 5.7 Coherence Variation during IHCs Deactivation

coherence during baseline and blue points after deactivation of IHCs. Solid lines are the linear fit for each points set.

Note that for Alpha (Figure 41A) the coherence of nearby recording sites, after IHC deactivation, diminished less than that of distant recording sites. Regarding LG coherence (Figure 41B), the results indicate a coherence increase of nearby recording sites, while distant recording sites remained almost unaltered. On average, this latter analysis reveals that the slope of the fit obtained for cooling coherence was, on average, more negative than for baseline fits, supporting our initial hypothesis that deactivation of IHCs would restrict the signal integration radius resulting in a more local LFP. Figure 42 depicts the results for the slope values of all datasets considering Alpha, LG and HG coherences.

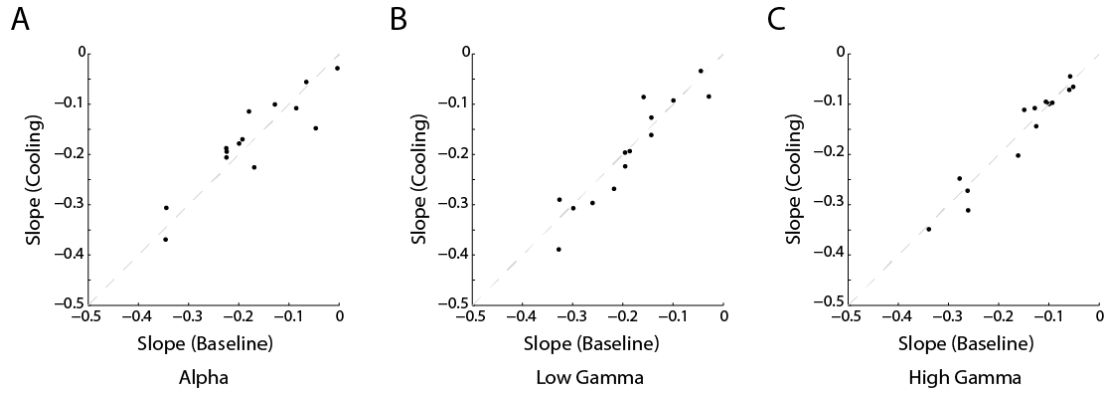


**Figure 42.** Slope variation after deactivations of IHCs for each LFP rhythm. Each point represents a pair of line slopes taken from the linear fits depicted on Figure 41. (A) Alpha. (B) Low Gamma. (C) High Gamma.

Each point represents the comparison between baseline and cooling slopes for a given dataset. Note that, even with small magnitude, the coherence variations tended to be under the identity line, revealing a shift to more negative slopes during cooling especially for Gamma ranges. However, the amount of points showing the opposite slope relation cannot be despised.

## 5.8. Summary of Results

### 5.8.1. From Individual Recording Sites

- We studied 205 highly selective recording sites, i.e. multi-units, ( $OI > 0.2$  or  $DI > 0.1$ ) with a receptive field in the center patch of the stimulus. IHC deactivation did not change the orientation or direction preferences of the neurons drastically. Direction selectivity was affected more strongly than orientation selectivity. However, in agreement with previous reports of a mainly multiplicative effect of interhemispheric connections without changing response properties both selectivity indices  $OI$  and  $DI$  did not change significantly (Schmidt et al., 2010; Wunderle et al., 2013)
- Firing rates evoked by both grating and natural scene Patch stimuli (“pop-out”) decreased more during deactivation of interhemispheric input than those evoked by uniform WF stimuli as indicated by more negative CI values. LFP power also largely decreased more for Patch than for WF stimulation but overall CI differences were smaller and reached significance only for the Low Gamma (grating, natural scene) or Alpha (natural scene) range.
- On average, firing rates were slightly higher for uniform WF stimuli than for the Patch stimuli as indicated by small negative SI values. However, despite this bias, facilitatory and suppressive effects observed with cross-oriented (Patch condition) as opposed to iso-oriented surround (WF condition) were rather balanced in our sample. A similar distribution was observed for LFP power. Interestingly, for grating but not for natural scene stimuli, this balance was slightly biased towards small positive values indicating that in the LFP the Patch evoked on average more power than the WF condition in the baseline.
- This difference between the two conditions increased in the absence of interhemispheric input for both firing rates and LFP power, i.e. during cooling the SI got on average more negative than during baseline. This was likely due to the fact that responses evoked by the Patch condition suffered much more from the lack of the IHC input than those evoked by the WF.
- Interestingly, the SI values, i.e. the difference in response strength for Patch versus WF grating stimulation, decreased with the increment of the frequency of the examined response band (Alpha-> LG-> HG-> firing rate). This result was less clear for natural scene stimulation, but LFP power showed always lower SI values than firing rates.

### 5.8.2. From Population Level

- Intriguingly, we found that the assemblies' joint orientation preference did not distribute uniformly over all possible orientation preferences. Rather, preferred orientations peaked closer to the orientation contained in the stimulation cocktail than to the ones in between. As for single units, the deactivation of IHCs did not affect the preference but the response strength of a certain assembly.
- In concordance with the findings for individual units' firing rates, assemblies spiked more often during WF than Patch conditions for both stimulus categories (gratings and natural scenes). However, in contrast to the result obtained for the individual units, assembly formation to both stimulus conditions suffered almost equally from the lack of the IHC so that the difference between the two conditions remains during cooling or even decreases as expressed by decreasing absolute SI values.
- Phase locking strength, expressed by the *kappa* value, of single and assembly responses to Patch was higher than to WF conditions. In the absence of interhemispheric input phase locking became on average stronger, i.e. *kappa* increased. As observed for the raw numbers of assembly activations, also *kappa* was affected similarly for all stimulus conditions. Thus, cooling did not lead to a better separation of WF and Patch responses.
- For natural scene stimulation, much higher *kappa* values were obtained for assemblies than from single neurons considered separately.
- The variation of the LFP-LFP coherences suggests that the increase of *kappa* after the deactivation of IHCs could be related to a general spatial reduction of signal integration. This reduction renders LFP signals more local and easier to coordinate with local spiking activity.

## 6. Discussion

### 6.1. Methodological discussion

#### 6.1.1. About Visual Stimulation

We used two stimulus categories: gratings and natural scenes. To work with gratings has the advantage of providing concrete stimulus features as spatial and temporal frequency, contrast, orientation, direction of motion, and others that can be used to identify certain preferences of the recorded cells. Moreover, it facilitates the characterization of neural responses as a function of specific stimulus feature variations. In addition, there is an abundant bibliography built through several years that allows comparison with published results based on controlled stimulus features. On the other hand, gratings are not the kind of visual stimulus that the brain normally has to deal with. High contrast gratings are likely to maximally drive orientation selective neuronal populations by a mere feed forward drive and thus put the cortex into a low gain regime, in which contextual influences are difficult to be unveiled. Indeed, contextual influences are easier to observe with low salient stimuli (Hupe et al., 1998; Mizobe et al., 2001; Nauhaus et al., 2009). Therefore, we introduced a figure-ground stimulus constructed from natural scenes. Indeed, the lateral network's influence we observed when deactivating the interhemispheric input was much higher with natural scene stimuli than with gratings on both firing rate and especially LFP power on the various investigated time scales. This is in line with previous observations that responses to lesser salient stimuli such as random dot textures (Wunderle et al., 2013) or single Gabor patches (Peiker et al., 2013) benefit much more from an intact network - in the sense of receiving predominantly excitatory inputs - than grating evoked responses. It also agrees with the notion that lateral influences are even more obvious in ongoing activity when a feed forward driving stimulus is absent (Peiker et al., 2013).

One major point in the stimulus definition was to delimit the CRF of each recording site in order to avoid direct feed-forward stimulation from the surround. In our case, we opted for a figure area sufficiently big (12 degrees of visual field angle) to enclose the CRFs of a larger population of nearby neurons (up to 28 recording sites). As the density of callosal connections is known to decrease with distance from the 17/18 border (Houzel et al., 1994; Hubel and Wiesel, 1967) and thus the vertical meridian's representation we chose a patch in form of a square in order to maintain the same eccentricity from the vertical meridian at all elevations. The tradeoff of such a stimulus design is that the border between foreground and background stimulus might introduce artificial contours or edges, which confound the CRF responses. However, the neurons selected for analysis had their receptive fields well within the confines of the patch.

Another argument that this stimulus construction did not bias our results comes from the results with natural scene stimulation. In order to overcome any “non-natural” bar-like contrast borders, we defined the foreground figure as a round patch with a blurred border. In fact, the results are not qualitatively different from the results obtained with the squared grating patch.

The patch figure was placed into the contralateral visual hemifield slightly below the horizontal meridian and close to the vertical meridian but without crossing it. The figure was thus restricted to that hemifield. However, it probably reached into the bilaterally represented overlap zone (Payne and Siwek, 1991; TUSA et al., 1978; TUSA et al., 1979) in some of the cases. Thus, it is possible that by the cooling procedure feed forward input indirectly delivered to the investigated neurons via the corpus callosum was eliminated. However, this does not explain our finding that the Patch conditions were always more affected by cooling than the WF conditions, as this argument should apply equally to all stimulus conditions. This is in line with earlier observations from our group that qualitative cooling effects do not depend on the absolute eccentricity of the investigated stimulus as long as it is situated in the transcallosally-connected zone of the visual field (Peiker et al., 2013). It rather strengthens the view that the callosal transition zone represents an area where feed forward and longer-range lateral networks interdigitate and perpetuate the intrahemispheric networks like anywhere else in the visual field.

### **6.1.2. About the cooling technique**

We used the cryoloop technique (Lomber et al., 1999) to deactivate the contralateral transition zone. This technique has several advantages over other older deactivation techniques. First, in contrast to lesion studies or sectioning of the corpus callosum and/or the optic chiasm cooling is reversible. Second, multiple deactivation cycles during one acute experiment are possible, which increases the statistical power and reduces the number of animals needed for a particular study. Third, the cooling loop can be flexibly adjusted to the cortical tissue to be deactivated.

Possible disadvantages arise from the fact that lowering the temperature below a physiological level can introduce different physiological effects. There will be a temperature gradient from tissue directly touching the probe to more distant cortical tissue (Lomber et al., 1999; Rushmore et al., 2005). Accordingly, different physiological effects might occur at different distances from the probe, like hyperexcitability of neurons at a specific temperature to complete silencing of synapses and thus depolarization block (Volgushev et al., 2009). It is thus likely that cortical areas directly beneath the cooling probe will be completely silenced due to a depolarization block. However, at some distance a region of cortex will be in the temperature range of hyperexcitability, thereby increasing

the activity of the neurons in those regions. Therefore, theoretically, cooling one hemisphere could paradoxically provide excitation onto the contralateral side via callosal connections. However, deoxyglucose labeling below cooling probes does not confirm that (Lomber et al., 1999).

We consider a direct spread of cooling to the recording site unlikely, because we left the bone bridge above the sinus sagittalis and thus the adhesion of the dura duplication – carrying the sinus – to the bone intact, providing a temperature barrier to the other hemisphere.

## 6.2. About Figure-Ground Segmentation

The figure-ground segmentation paradigm aims to understand how the visual system recognizes and separates a given object from its background. The main approach is to use visual stimulus configurations containing an area defined to perceptually pop-out (figure) from its background and identify neuronal response variations of neurons with their CRF inside the figure's area. Several works studied the variation of firing rate during this experimental framework and considered a firing increase to the figure as an electrophysiological correlate of figure-ground segmentation (Biederlack et al., 2006; Lamme, 1995). As in previous studies we defined the figure by an orientation or motion contrast introduced into the background. Contrary to the idea of a “pop-out”, we obtained, on average, slightly higher firing rates for the iso-oriented whole-field than for the cross-oriented Patch configuration.

Our low facilitation rate for cross-oriented surround (Patch) configuration can be associated with anesthesia. In concordance with (Lamme et al., 1998) who demonstrated that V1 neurons from awake monkeys that initially increased their firing rates when stimulated by a figure did not show any response variation between uniform stimuli and such containing a “pop-out” under anesthesia. However, our results from grating stimulation revealed an almost equal amount of clear increases and decreases (see histogram, Figure 29), supporting the idea that even under anesthesia, a considerable population can show a correlate of figure-ground segmentation. Our numbers are rather in line with a study in anesthetized cats using grating stimuli and reporting that 36% of the neurons responded significantly better to a motion and 24% to an orientation feature-contrast than to uniform stimulation (Kastner et al., 1997).

An alternative interpretation could be that earlier studies in awake animals did not have access to a large, in parallel recorded number of neurons and thus underestimated the true number of indifferent units or those suppressed by the figure.

## 6. Discussion

Finally, we could also come to the conclusion that the minimum requirement for a possible figure-ground segmentation mechanism is simply that responses for stimuli with and without figure have to be distinguishable. This requirement seems to be fulfilled even in anesthesia and significant facilitation or suppression could be two parts of the same segmentation process. It is possible that the ratio can be shifted more towards facilitation by optimizing the stimuli for single neurons, setting a contrast difference between figure and background (Levitt and Lund, 1997) or recording in an un-anesthetized preparation.

Along the line of a dynamical facilitation/suppression ratio in the population of neurons responding to a foreground figure is also that - differently from grating stimulation - natural scene stimulation did not reveal the same proportion of positive and negative values of SI. In this case, the ratio was shifted to predominately negative SI values, indicating higher firing rates from WF conditions for the majority of recording sites. As the stimulation was likely to be sub-maximal for the majority of neurons natural scene stimulation also evoked lower spike rates. Nevertheless, absolute SI values could be as large or larger as for grating stimulation indicating that figure-ground and uniform stimulation were well segregated.

### 6.3. About the Influence of Interhemispheric Connections on Raw Responses

Our results support the idea that connections between the primary visual areas in the two hemispheres play a similar role than that reported for long-range horizontal connections and serve predominantly excitatory functions. As observed previously with bar or grating stimuli, deactivation through reversible cooling of the contralateral hemisphere showed an average decrease of firing rates (about 19%) reflecting a mainly excitatory influence but also significant inhibitory actions (Payne et al., 1991; Peiker et al., 2011; Schmidt et al., 2010; Wunderle et al., 2013). With natural scene stimulation, excitatory action predominated clearly more (about 34%) matching the results for stimuli with a lower contrast or lesser saliency in previous interhemispheric (Peiker et al., 2013; Wunderle et al., 2013) and feedback deactivation studies (Galuske et al., 2000; Hupe et al., 1998). Interestingly, the average LFP power did not even decrease in the Gamma frequency bands for grating stimulation but decreased drastically for natural scene stimulation in all three examined frequency ranges (see Figure 26 and Figure 28). This goes in parallel with the average changes observed for the firing rates. However, when comparing individual rate and power changes per cell and stimulation these were not necessarily correlated, especially not for gratings and the Alpha and LG band (data not shown; T. Wunderle personal communication).

Our grating LFP finding is in line with previous reports that especially with gratings an almost equal amount of excitatory and inhibitory effects can be observed in the local field

potential (Makarov et al., 2008). A possible interpretation is that more inhibitory than excitatory actions remains subthreshold. Apparently, high-contrast square wave gratings evoke more such inhibition than natural scenes, possibly because they evoke maximal response in a population of neurons which is densely interconnected by both orientation-selective excitatory but also direct or indirect inhibitory connections.

Further, in our study, effects on the strength of orientation selectivity were mild without changing the orientation preference. This in accordance with studies demonstrating that horizontal connections contribute to orientation selectivity but do not instruct it (Eysel et al., 1990; Galuske et al., 2002; Wunderle et al., 2013). Direction selectivity was clearly more disturbed than orientation selectivity and individual direction preferences could change dramatically but on average these trends were not significant like in previous interhemispheric deactivation studies with grating stimuli (Peiker et al., 2013; Wunderle et al., 2013). In summary, our results are thus compatible with a mainly multiplicative effect on tuning curves (Wunderle et al., 2013).

## **6.4. About the Influence of Interhemispheric Connections on Figure-Ground Segmentation**

### **6.4.1. Spike Rates**

Newer theoretical models usually consider a collaboration of feedback and horizontal cortical networks to account for figure-ground segmentation in early visual areas (Roelfsema et al., 2002; Schwabe et al., 2006; Shushruth et al., 2012) but a causal contribution of either of these connections has been rarely demonstrated.

In a causal approach using cooling, Hupe and colleagues (1998) showed that feedback connections from the awake monkey's MT facilitate early visual responses to objects moving within the CRF and can enhance suppression evoked by a uniformly moving background stimulus.

Although a role for horizontal or lateral intrinsic connections in figure-ground segmentation tasks has been indirectly inferred many times (Angelucci and Bullier, 2003) a direct test by interrupting them has not been undertaken. This test would be also difficult as any pharmacological or thermal manipulation of an intrinsic connection will directly influence the cortical area under study.

Here, we deactivated interhemispheric connections as a model for a special type of lateral intrinsic connection. Although in the baseline data, the Patch, i.e. "pop-out", configuration evoked less activity than the uniform whole-field stimulus in the majority of signal types

and for both grating and natural scene stimuli (except for the grating LFP and *kappa* phase-locking values) we observed a stronger influence of the lack of IHC input for exactly that stimulus. Segmentation indices remain negative and get even larger during cooling but this is mainly caused by the fact that the response to the Patch stimulus loses more excitatory drive (drop of CI) than that to the WF stimulus. Thus, there is indirect evidence for a facilitating effect of lateral connectivity on the “pop-out” configuration. Removing the ipsilateral hemifield stimulation by cooling deactivation of the right hemisphere removes probably more surround stimulus than foreground figure. As the majority of IHCs are of excitatory nature it is likely that this distant surround part had a larger facilitatory effect when setting a contrast (Patch) as compared to the uniform background pattern. When removing that distant input the Patch responses loose more activity than the WF responses. WF responses also loose excitatory input but they might be more stabilized by local interactions from the intra-hemispheric CRF surround than the Patch with the result that, on average, Patch responses are even lower than WF responses during cooling.

This interpretation is strongly supported by individual cases where the Patch evoked higher baseline activity than the WF configuration and lost more spikes during deactivation than the latter (see Figure 25B). Also along this line, individual cases with stronger WF than Patch configuration demonstrate that these WF responses did not suffer that much during cooling. Future analyses and experiments should be undertaken to further elucidate that issue by including a Patch stimulus without any surround into our stimulus cocktail for comparison.

Our results are in line with the report of Hupe et al. (1998) in the sense that the responses to the stimulus with the largest contrast between foreground and background suffered more from deactivation of feedback/lateral connectivity than the uniform stimulus (see their Figure 3a). Their uniform stimulus (a moving bar on a background moving into the same direction), though, evokes less activity during baseline than their patch configuration but the two stimuli and settings (awake monkey V3 versus anesthetized cat V1) might not be directly comparable.

Taken together the evidence from previous feedback and our interhemispheric deactivation study our results are compatible with the interpretation that feedback circuits exert their action in perceptual grouping by impinging on horizontal networks (Gilbert and Li, 2013; Roelfsema, 2006).

#### 6.4.2. Local Field Potential Power

Despite that the efforts to understand the neuronal mechanism behind figure-ground segmentation have been concentrated on spiking activity, LFP signals could also give

## 6. Discussion

important insights as they involve bigger populations. Our baseline results revealed also differences in the LFP's power, at certain frequency bands, between responses to WF and Patch configurations. Interestingly, different from natural scenes, the grating LFPs showed on average more power in the baseline Alpha and LG bands for the Patch condition than for the WF condition supporting the conclusion that uniform high-contrast gratings evoke more subthreshold inhibitory activity than natural scenes. However, cooling also removed more power to LFP responses for the patch than for the WF condition in the majority of cases.

The key to explain such differences could be in the LFP's fluctuations induced by the balance between inhibitory and excitatory spiking activity. The LFP signal is the result of superposition of all ionic processes involved in a brain tissue and it depends on the contribution of several sources (for review see (Buzsaki et al., 2012)). One main source of LFP's fluctuations is the flux of  $I_h$  and  $I_T$  intrinsic currents through the membrane. In high intracellular depolarization states, this flux can generate sustained membrane's potential oscillations due to its resonance properties. These oscillations will be reflected in the LFP signal, if they occur synchronously in nearby neurons producing an additive superposition rather than a cancelation superposition of individual neurons' activity.

In a recent model of surround modulation, Shushruth and colleagues (2012) proposed a balance between local orientation-dependent excitation and two sources of inhibition: one iso-oriented inhibitory connection through high threshold inhibitory interneurons (I), and another between columns of both similar and different orientation preferences through basket-like inhibitory neurons (B) with recurrent connections onto themselves, as well as reciprocal connections with pyramidal excitatory neurons (E) (see Figure 43).

Taking together Shushruth's model and the above elaborated generation mechanism for LFPs we might propose that for grating Patches, the recurrent and reciprocal connections between B and E neurons can account for a coordinated activity resulting in an additive superposition of membrane's fluctuations reflected as an oscillatory LFP. The oscillatory capability of this kind of network architecture is also supported in Gamma generation models (PING models, see (Tiesinga and Sejnowski, 2009)). This synchrony could be diminished by a higher contribution of non-reciprocal I connections proceeding from the iso-oriented surround in WF conditions, resulting in less coordinated LFP's contributions and therefore less LFP's power at Alpha and LG bands as seen during grating WF stimulation.

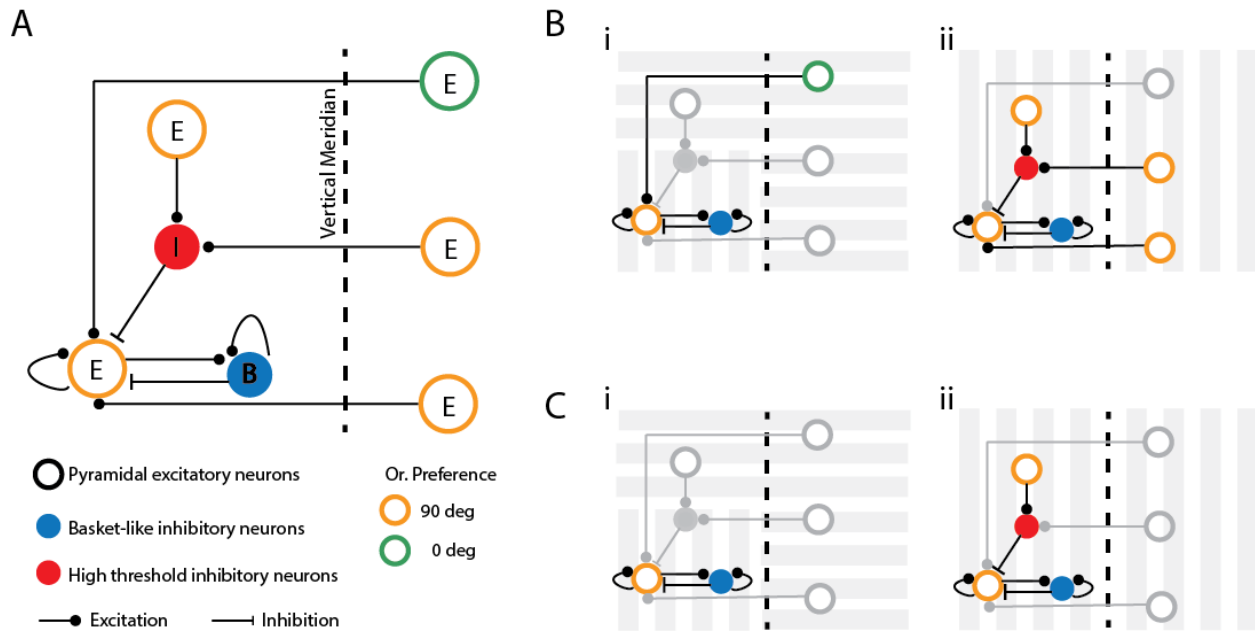


**Figure 43. Model of LFP generation during figure-ground segmentation.** (A) General connectivity of the model proposed by (Shushruth et al., 2012). Here we added the interhemispheric input represented by the excitatory neurons on the right hemisphere. The connectivity configuration formed by pyramidal and basket-like neurons is considered to form a natural oscillator. (B) Baseline during Patch stimulation (i) the oscillator is free from disturbances from iso-oriented excitation and inhibition through inhibitory neuron I (gray symbols), differently from WF stimulation (ii). (C) Cooling. The interhemispheric input during WF stimulation (ii) is removed, reducing the disturbance of the oscillator, thereby increasing the LFP power.

In contrast, natural scene stimulation lacks this huge amount of iso-orientation-driven activity by lateral connections from the surround because neurons are more likely to be differently stimulated at different moments in time than similarly. Thus, the proportion of the contributions from B and I to the LFP's fluctuation remain unaltered regardless the stimulus' configuration resulting in similar baseline LFP power for Patch and WF configuration in all frequency bands.

An alternative explanation for the contrast between gratings and natural scene is based on the intuitive idea that the neural connectivity is “pre-configured” to process natural scenes rather than gratings. This could imply a more robust balance between all different excitatory and inhibitory sources which explains the similarity of the responses to WF and Patch stimulations during baseline. Thus, the lack of interhemispheric input would result in an unbalanced behavior of the network, thereby generating the response differences. In the case of grating stimulation, the stimulus would evoke an unbalance behavior already in the baseline since the inhibition from iso-oriented surround is set by WF stimulation, thereby creating the response differences through feed-forward drive.

Interestingly, the SI showed a systematic variation in function of the frequency increase of the analyzed responses (Alpha, Low Gamma, High Gamma and spiking activity) supporting the idea that population activity, as represented by LFP, could contain additional information pieces to spiking activity about a particular figure-ground segmentation in different frequency bands.

When deactivating IHCs, LFP power was also largely more diminished for the Patch condition than for the WF condition. This led to a decrease of the SI with the result that Patch stimuli, which evoked similar or more LFP power than whole fields in the baseline were now clearly weaker. This result suggests that while for Patch conditions, the contributions of E, I and B neurons was proportionally reduced, for WF conditions the contribution from I neurons was proportionally more affected, reducing its interference in LFP's oscillations generated by E and B. This is in concordance with the idea that IHCs are orientation selective; therefore their deactivation reduces the drive on iso-oriented surround neurons that previously had an inhibitory influence through I neurons. In conclusion, the reasons why LFP power did, on average, not decrease so much for whole field as for Patch gratings are the following. An overall loss of excitatory drive E that was removed from the ipsilateral hemifield affected both stimulus conditions. However, for uniform whole field gratings this loss of excitation was at the same time counter-balanced by a removal of iso-orientation inhibition. The latter was not the case for the Patch condition.

#### **6.4.3. Assemblies and Phase Locking**

In a third approach, we considered the coordinated activity of groups of neurons (assemblies) and the results were qualitatively similar to those from firing rates from individual recording sites. We obtained less assembly activations for Patch than for WF conditions in the baseline. Yet, the SI calculated from assemblies' activity was more than three times higher in module than for firing rates. This suggests a more marked difference between the responses to WF and Patch conditions and points to the strongest influence of the surround stimulation on population activity. However, since the absolute number of activations is much lower than the number of spikes, this result can be biased by the SI definition. Since the raw difference in the number of spikes and in the number of assembly activations are in the same order of magnitude, it is interesting for future works to evaluate whether the reduction of firing rates is predominantly a result of variations in the activity of specific neurons that are also involved in assembly's activity.

Our results also suggested different relations between the time of occurrence of spiking events (spikes or assembly's activation) and the LFP's phase depending on the stimulus configuration (WF or Patch). In primary visual cortex, phase relations in specific frequency

bands have been related to coordinate the latency of synchronous responses (first-spike latency) of groups of neurons sharing the same orientation preferences (Fries et al., 2001). This spiking activity coordination could be based on the definition of windows of depolarization, creating specific time intervals when arriving inputs are more effective (Volgushev et al., 1998)

In a figure-ground paradigm, the key could be in considering the coordination of spiking activity and the area in the visual field whose stimulation contributes to the LFP that performs such coordination. By means of locking the event activity to a certain phase of the underlying field potentials, neurons, which simultaneously raise their spiking activity because of a visual stimulus, could be tagged as belonging to either the figure or the background (Singer, 2009)

If we consider the activity of a group of neurons as representation of a stimulus in a delimited area of the visual field, we could intuitively expect a higher coordination of such a group with the LPF signal resulting from the population that processes the same area of the visual field, in comparison with an LFP signal resulting from a bigger population that also processes distant areas in the visual field. This idea is in concordance with our results of the assembly's activity where the *kappa* value consistently indicated stronger phase locking during Patch conditions in comparison with WF conditions. The Patch configuration could generate a more local LFP around the assembly than the WF configuration. This is because the Patch lacks influences from neurons stimulated by the surround that share the same orientation preferences and are directly connected through lateral orientation-selective connections.

For the natural scene stimulation, this argumentation is also applicable if we consider that the coherent direction of movement of figure and surround could enhance the coherence between populations stimulated by both areas of the visual field, resulting in a less local LFP for the WF condition.

The phase locking result was more robust for assemblies than for single units. This could be related to the notion that individual neurons can be easier perturbed than assemblies. In the latter case, if a given neuron loses its synchrony with the assembly or alters its firing pattern, the assembly still can maintain its main firing pattern based on the activity of the other neurons forming it. By this mechanism, redundancy is ensured and the same information can be coded even though not all neurons faithfully participate in each assembly event. This is also supported by higher assembly's *kappa* values mainly with natural scene stimulation.

Most interestingly, the deactivation of IHCs uniformly increased *kappa* for both Patch and WF conditions. Assembly activations continued to be stronger phase locked for the Patch than for the WF conditions and the ratio between the Patch and WF *kappa* did not change.

This did not hold true for the single cell phase locking, in agreement with the fact that the individual cell's spike and LFP responses also changed during cooling.

One possible explanation of the uniform *kappa* increase for assemblies could be that the cooling procedure eliminates the input of half of the visual field, which belonged to the surround, thus reducing the contribution of that area to the LFP, hence enhancing the local/global relation. Support for that interpretation can be inferred from the LFP-LFP coherence analysis. This coherence is interpreted as synchronized activity of different neuron populations and is proven to fall with increasing distance and is higher for lower frequency bands (Neuhaus et al., 2009). The IHCs deactivation resulted in a tendency of a faster decay of coherences over the same distance and in some cases even an increase of coherence between nearby recording sites. In general terms, this result can be interpreted as enhancing the local/global relation of the LFP.

The significantly higher number and higher phase locking of assemblies evoked by the Patch as opposed to the WF stimulation especially for the lesser salient natural scenes indicates that this variable might be useful to separate the stimulus, which is "popping out" from the contrasting background from the uniform stimulation. Most interestingly, the ratio between Patch and WF assembly activation and phase locking was not changed when IHCs were lacking. This is surprising as all other variables, which show higher values for the WF than for the Patch condition, decreased significantly more for the Patch during cooling (decreasing SIs in spike and assembly activations, LFP power).

There are two alternative interpretation of this finding:

- I. A phase locking code is not important for figure-ground segmentation implemented by "lateral" interhemispheric connections as this can be done by simpler codes like firing rates. Support for that interpretation comes from earlier studies arguing that a code using the coordinated activity from many neurons would be only used in cases where a rate code is not sufficient (Samonds et al., 2003; Biederlack et al., 2009).
- II. Assembly phase locking is a likely code for figure-ground segmentation but IHC deactivation did not influence the coding of our particular figure-ground segmentation qualitatively. Although the number of spikes and the overall LFP power decreased more for the Patch than for the WF the phase locking ratio between the two stimulus configurations remained the same because the removed spikes were redundant for the figure-ground operation. This is supported by the fact that assembly phase locking was in general more robust than the single cell phase locking, and that assembly phase locking was the only variable responding on average "better" to the stimulus containing the figure.

## 6. Discussion

It is important to note that despite our results supporting the idea that intrinsic horizontal connections and IHCs share similar functions, our experimental approach of deactivating the contralateral hemisphere cannot account for a generalization of the lateral network's role in figure-ground segmentation. A large intra-hemispheric part of this network remained probably fully functional during the experiments and thus accounts for persistent figure-ground segmentation in the absence of callosal input.

## 7. Summary and Conclusion

In the current thesis, we performed electrophysiological recordings using multi-electrode arrays implanted in the primary visual cortex of anesthetized cats. We used a figure-ground segmentation paradigm using both classical grating and natural scene stimuli in order to evaluate the effects on the spiking activity and LFP from individual recording sites derived from changes in a visual field area defined as surround. We also evaluated the presence and activity of neuronal assemblies and their relation with the phase of the LFP signal in different frequency bands.

In order to examine the influence of lateral interhemispheric connections (acting on the same hierarchical level as lateral intracortical connections) on a possible figure-ground segmentation mechanism, we deactivated these connections by performing a reversible cooling procedure of a topographically corresponding part of the contralateral hemisphere.

The results led us to conclude that the figure-ground segmentation mechanism involves a more complex process than a simple increase of the firing rates of a given group of neurons. Instead, by comparing the responses from a stimulus configuration with and without figure (i.e. WF and Patch), we observed a “continuum” starting from recording sites whose responses were diminished by the Patch configuration, passing through recoding sites with practically unaltered responses and ending with recording sites with increased responses to this same stimulus configuration. In addition, the difference in the stimulus processing between WF and Patch configuration was also reflected in the LFP’s power.

Furthermore, we demonstrated the presence of neuronal assemblies spiking synchronously in our population. These assemblies had orientation preferences and assembly activation times were phase locked to the LFP in different frequency bands. Phase locking was stronger for stimuli, which contained a figure on the population’s CRF (Patch) than for uniform stimuli (WF). This indicates that the figure-ground segmentation mechanism involves not only the spiking activity or the fluctuations of field potentials as separate codes but instead a coordinated interaction between the two. We propose that the foreground assemblies’ preference of firing during a given LFP’s phase could reflect coordinated processing of a delimited area of the visual field, i.e. the figure.

Part of the origin of the differences between the responses to WF and Patch configurations can be explained by the action of intra- and interhemispheric lateral connections. The deactivation of IHCs revealed that these connections could contribute a mainly excitatory drive to both Patch and WF configurations and an additional inhibitory drive to the uniform WF stimulation. Therefore, more single cell spikes to Patch than to uniform WF stimulation get lost in the absence of the IHC. These changes could also indirectly reflect feedback connections from the other hemisphere acting on the lateral network there.

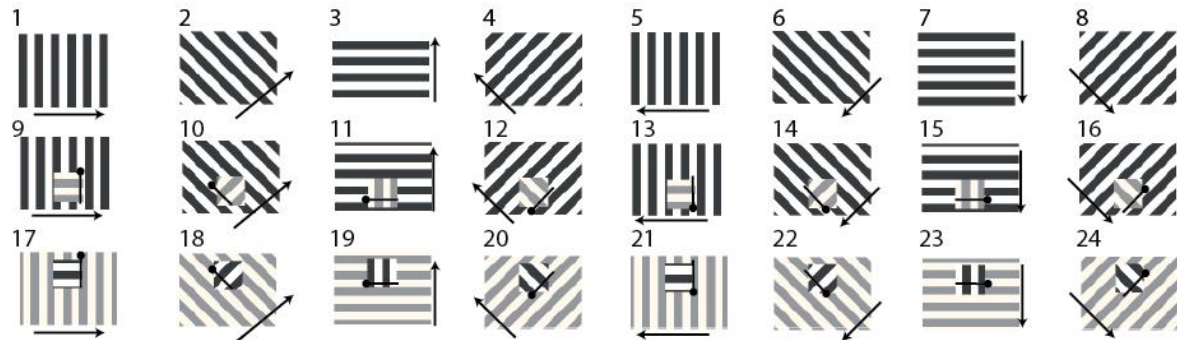
## 7. Summary and Conclusion

However, even accepting IHCs as a good model of lateral connectivity, our results might reflect the effect of the manipulation of only a small part of that network. This is emphasized by the observation that during IHC deactivation all neuronal activities investigated continue to indicate a difference between the two stimulus configurations and that the assembly phase locking ratio is not changed at all.

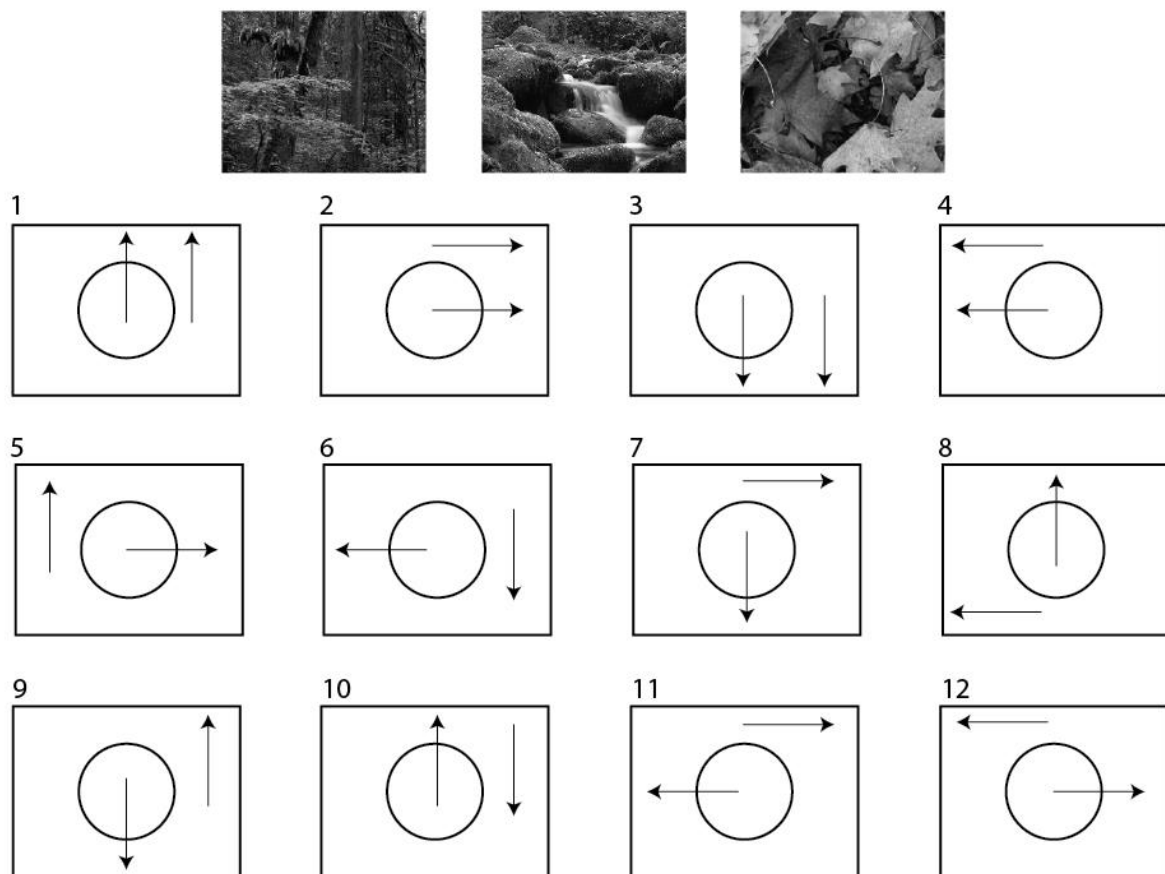
In conclusion, our results might be also interpreted in the direction that a population code like the coordinated activity of many neurons locked to their LFP is more robust to manipulations of the cortical network (i.e. removal of half of the visual field) than single cell activity.

## 8. Supplementary

A



B



**Supplementary Figure 1.** All stimulus conditions. (A) Grating stimulus. (B) Natural scene stimulus. Three different images were used (up), moving in 12 different configurations (down)

## 9. References

- Allman, J., Miezin, F., and McGuinness, E. (1985). Stimulus specific responses from beyond the classical receptive field: neurophysiological mechanisms for local-global comparisons in visual neurons. *Annu Rev Neurosci* 8, 407-430.
- Angelucci, A., and Bressloff, P.C. (2006). Contribution of feedforward, lateral and feedback connections to the classical receptive field center and extra-classical receptive field surround of primate V1 neurons. *Prog Brain Res* 154, 93-120.
- Angelucci, A., and Bullier, J. (2003). Reaching beyond the classical receptive field of VI neurons: horizontal or feedback axons? *Journal of Physiology-Paris* 97, 141-154.
- Barlow, H.B. (1972). Single units and sensation: a neuron doctrine for perceptual psychology? *Perception* 1, 371-394.
- Berlucchi, G., and Rizzolatti, G. (1968). Binocularly driven neurons in visual cortex of split-chiasm cats. *Science* 159, 308-310.
- Biederlack, J., Castelo-Branco, M., Neuenschwander, S., Wheeler, D.W., Singer, W., and Nikolić, D. (2006). Brightness induction: rate enhancement and neuronal synchronization as complementary codes. *Neuron* 52, 1073-1083.
- Blakemore, C., Fiorentini, A., and Maffei, L. (1972). A second neural mechanism of binocular depth discrimination. *J Physiol* 226, 725-749.
- Bloom, J.S., and Hynd, G.W. (2005). The role of the corpus callosum in interhemispheric transfer of information: excitation or inhibition? *Neuropsychol Rev* 15, 59-71.
- Buhl, E., and Singer, W. (1989). The callosal projection in cat visual-cortex as revealed by a combination of retrograde tracing and intracellular injection. *Experimental brain research, Buhl e, singer w.*
- Buzsaki, G., Anastassiou, C., and Koch, C. (2012). The origin of extracellular fields and currents - EEG, ECoG, LFP and spikes. *Nature Reviews Neuroscience* 13, 407-420.
- Buzás, P., Eysel, U.T., Adorján, P., and Kisvárday, Z.F. (2001). Axonal topography of cortical basket cells in relation to orientation, direction, and ocular dominance maps. *J Comp Neurol* 437, 259-285.
- Buzás, P., Eysel, U.T., and Kisvárday, Z.F. (1998). Functional topography of single cortical cells: an intracellular approach combined with optical imaging. *Brain Res Brain Res Protoc* 3, 199-208.

Carmeli, C., Lopez-Aguado, L., Schmidt, K.E., De Feo, O., and Innocenti, G.M. (2007). A novel interhemispheric interaction: modulation of neuronal cooperativity in the visual areas. PLoS One 2, e1287.

Cavanaugh, J.R., Bair, W., and Movshon, J.A. (2002a). Nature and interaction of signals from the receptive field center and surround in macaque V1 neurons. J Neurophysiol 88, 2530-2546.

Cavanaugh, J.R., Bair, W., and Movshon, J.A. (2002b). Selectivity and spatial distribution of signals from the receptive field surround in macaque V1 neurons. J Neurophysiol 88, 2547-2556.

Cerri, C., Restani, L., and Caleo, M. (2010). Callosal contribution to ocular dominance in rat primary visual cortex. Eur J Neurosci 32, 1163-1169.

Choudhury, B.P., Whitteridge, D., and Wilson, M.E. (1965). The function of the callosal connections of the visual cortex. Q J Exp Physiol Cogn Med Sci 50, 214-219.

Cook, N.D. (1984). Homotopic callosal inhibition. Brain Lang 23, 116-125.

Crook, J.M., Kisvárdy, Z.F., and Eysel, U.T. (1998). Evidence for a contribution of lateral inhibition to orientation tuning and direction selectivity in cat visual cortex: reversible inactivation of functionally characterized sites combined with neuroanatomical tracing techniques. Eur J Neurosci 10, 2056-2075.

Das, A., and Gilbert, C.D. (1995). Long-range horizontal connections and their role in cortical reorganization revealed by optical recording of cat primary visual cortex. Nature 375, 780-784.

DeAngelis, G.C., Freeman, R.D., and Ohzawa, I. (1994). Length and width tuning of neurons in the cat's primary visual cortex. J Neurophysiol 71, 347-374.

Denenberg, V.H., Gall, J.S., Berrebi, A., and Yutzey, D.A. (1986). Callosal mediation of cortical inhibition in the lateralized rat brain. Brain Res 397, 327-332.

Dennis, M. (1976). Impaired sensory and motor differentiation with corpus callosum agenesis: a lack of callosal inhibition during ontogeny? Neuropsychologia 14, 455-469.

Elberger, A.J. (1989). Binocularity and single cell acuity are related in striate cortex of corpus callosum sectioned and normal cats. Exp Brain Res 77, 213-216.

Engel, A.K., König, P., Kreiter, A.K., and Singer, W. (1991). Interhemispheric synchronization of oscillatory neuronal responses in cat visual cortex. Science 252, 1177-1179.

Eysel, U.T., Crook, J.M., and Machemer, H.F. (1990). GABA-induced remote inactivation reveals cross-orientation inhibition in the cat striate cortex. *Exp Brain Res* 80, 626-630.

Fiorani, M., Azzi, J., Soares, J., and Gattass, R. (2014). Automatic mapping of visual cortex receptive fields: A fast and precise algorithm. *Journal of Neuroscience Methods* 221, 112-126.

Fries, P., Reynolds, J., Rorie, A., and Desimone, R. (2001). Modulation of oscillatory neuronal synchronization by selective visual attention. *Science* 291, 1560-1563.

Gail, A., Brinksmeyer, H., and Eckhorn, R. (2000). Contour decouples gamma activity across texture representation in monkey striate cortex. *Cerebral Cortex* 10, 840-850.

Galaburda, A.M. (1984). Anatomical asymmetries. In *Cerebral Dominance*, A.M. Galaburda, and N. Geschwind, eds. (Cambridge: Harvard Press), pp. 11-25.

Galuske, R., Schmidt, K., Goebel, R., Lomber, S., and Payne, B. (2000). Feedback control of orientation and direction maps in primary visual cortex. *European Journal of Neuroscience* 12, 73-73.

Galuske, R., Schmidt, K., Goebel, R., Lomber, S., and Payne, B. (2002). The role of feedback in shaping neural representations in cat visual cortex. *Proceedings of the National Academy of Sciences of the United States of America* 99, 17083-17088.

Geschwind, N., and Galaburda, A.M. (1985). Cerebral lateralization. Biological mechanisms, associations, and pathology: II. A hypothesis and a program for research. *Arch Neurol* 42, 521-552.

Gilbert, C., and Li, W. (2013). Top-down influences on visual processing. *Nature Reviews Neuroscience* 14, 350-363.

Gilbert, C.D. (1992). Horizontal integration and cortical dynamics. *Neuron* 9, 1-13.

Gilbert, C.D., and Wiesel, T.N. (1985). Intrinsic connectivity and receptive field properties in visual cortex. *Vision Res* 25, 365-374.

Gilbert, C.D., and Wiesel, T.N. (1992). Receptive field dynamics in adult primary visual cortex. *Nature* 356, 150-152.

Girardin, C.C., and Martin, K.A. (2009). Cooling in cat visual cortex: stability of orientation selectivity despite changes in responsiveness and spike width. *Neuroscience* 164, 777-787.

Gray, C.M., König, P., Engel, A.K., and Singer, W. (1989). Oscillatory responses in cat visual cortex exhibit inter-columnar synchronization which reflects global stimulus properties. *Nature* 338, 334-337.

Grinvald, A. (1996). Insights from optical imaging of architecture and function in the living brain. *Progress in Biophysics & Molecular Biology* 65, PL1-PL1.

Haslinger, R., Pipa, G., Lima, B., Singer, W., Brown, E.N., and Neuenschwander, S. (2012). Context Matters: The Illusive Simplicity of Macaque V1 Receptive Fields. *Plos One* 7.

Hebb, D.O. (1949). *The Organization of Behaviour* (New York: Wiley & Sons).

Hopfield, J. J. (1995). Pattern recognition computation using action potential timing for stimulus representation. *Nature* 376: 33-36

Houzel, J.C., Milleret, C., and Innocenti, G. (1994). Morphology of callosal axons interconnecting areas 17 and 18 of the cat. *Eur J Neurosci* 6, 898-917.

Hubel, D.H., and Wiesel, T.N. (1959). Receptive fields of single neurones in the cat's striate cortex. *J Physiol* 148, 574-591.

Hubel, D.H., and Wiesel, T.N. (1960). Receptive fields of optic nerve fibres in the spider monkey. *J Physiol* 154, 572-580.

Hubel, D.H., and Wiesel, T.N. (1962). Receptive fields, binocular interaction and functional architecture in the cat's visual cortex. *J Physiol* 160, 106-154.

Hubel, D.H., and Wiesel, T.N. (1963). Receptive fields of cells in striate cortex of very young, visually inexperienced kittens. *J Neurophysiol* 26, 994-1002.

Hubel, D.H., and Wiesel, T.N. (1965). Receptive fields and functional architecture in two nonstriate visual areas (18 and 19) of the cat. *J Neurophysiol* 28, 229-289.

Hubel, D.H., and Wiesel, T.N. (1967). Cortical and callosal connections concerned with the vertical meridian of visual fields in the cat. *J Neurophysiol* 30, 1561-1573.

Hubel, D.H., and Wiesel, T.N. (1968). Receptive fields and functional architecture of monkey striate cortex. *J Physiol* 195, 215-243.

Hupe, J., James, A., Payne, B., Lomber, S., Girard, P., and Bullier, J. (1998). Cortical feedback improves discrimination between figure and background by V1, V2 and V3 neurons. *Nature* 394, 784-787.

Ichida, J.M., Schwabe, L., Bressloff, P.C., and Angelucci, A. (2007). Response facilitation from the "suppressive" receptive field surround of macaque V1 neurons. *J Neurophysiol* 98, 2168-2181.

Innocenti, G.M., Clarke, S., and Kraftsik, R. (1986). Interchange of callosal and association projections in the developing visual cortex. *J Neurosci* 6, 1384-1409.

Joo, S.J., Boynton, G.M., and Murray, S.O. (2012). Long-range, pattern-dependent contextual effects in early human visual cortex. *Curr Biol* 22, 781-786.

Kandel, E., Schwartz, J., and Jessell, T. (2000). *Principles of Neural Science* (McGraw-Hill).

Kapadia, M.K., Ito, M., Gilbert, C.D., and Westheimer, G. (1995). Improvement in visual sensitivity by changes in local context: parallel studies in human observers and in V1 of alert monkeys. *Neuron* 15, 843-856.

Karube, F., and Kisvárday, Z.F. (2011). Axon topography of layer IV spiny cells to orientation map in the cat primary visual cortex (area 18). *Cereb Cortex* 21, 1443-1458.

Kastner, S., Nothdurft, H.C., and Pigarev, I.N. (1997). Neuronal correlates of pop-out in cat striate cortex. *Vision Res* 37, 371-376.

Kayser, C., and Konig, P. (2004). Stimulus locking and feature selectivity prevail in complementary frequency ranges of V1 local field potentials. *European Journal of Neuroscience* 19, 485-489.

Kisvárday, Z.F., and Eysel, U.T. (1993). Functional and structural topography of horizontal inhibitory connections in cat visual cortex. *Eur J Neurosci* 5, 1558-1572.

Kisvárday, Z.F., Tóth, E., Rausch, M., and Eysel, U.T. (1997). Orientation-specific relationship between populations of excitatory and inhibitory lateral connections in the visual cortex of the cat. *Cereb Cortex* 7, 605-618.

Knierim, J.J., and van Essen, D.C. (1992). Neuronal responses to static texture patterns in area V1 of the alert macaque monkey. *J Neurophysiol* 67, 961-980.

König, P., Engel, A.K., Löwel, S., and Singer, W. (1993). Squint affects synchronization of oscillatory responses in cat visual cortex. *Eur J Neurosci* 5, 501-508.

Lamme, V., Zipser, K., and Spekreijse, H. (1998). Figure-ground activity in primary visual cortex is suppressed by anesthesia. *Proceedings of the National Academy of Sciences of the United States of America* 95, 3263-3268.

Lamme, V.A. (1995). The neurophysiology of figure-ground segregation in primary visual cortex. *J Neurosci* 15, 1605-1615.

Lamme, V.A., and Spekreijse, H. (1998). Neuronal synchrony does not represent texture segregation. *Nature* 396, 362-366.

Lassonde, M. (1986). The facilitatory influence of the corpus callosum on intrahemispheric processing. In *Two hemispheres - One brain: Functions of the Corpus Callosum*, F. Lepore, M. Ptito, and H.H. Jasper, eds. (New York), pp. 385 - 402.

Lepore, F., and Guillemot, J.P. (1982). Visual receptive field properties of cells innervated through the corpus callosum in the cat. *Exp Brain Res* 46, 413-424.

Levitt, J.B., and Lund, J.S. (1997). Contrast dependence of contextual effects in primate visual cortex. *Nature* 387, 73-76.

Lima, B., Singer, W., Chen, NH., neuenschwander, S. (2010) Synchronization dynamics in response to plaid stimuli in monkey V1. *Cereb Cortex*. 20 (7): 1556-73.

Lomber, S., Payne, B., and Horel, J. (1999). The cryoloop: an adaptable reversible cooling deactivation method for behavioral or electrophysiological assessment of neural function. *Journal of Neuroscience Methods* 86, 179-194.

Lopes-dos-Santos, V., Conde-Ocazinez, S., Nicolelis, M.A., Ribeiro, S.T., and Tort, A.B. (2011). Neuronal assembly detection and cell membership specification by principal component analysis. *PLoS One* 6, e20996.

Lopes-dos-Santos, V., Ribeiro, S., and Tort, A.B. (2013). Detecting cell assemblies in large neuronal populations. *J Neurosci Methods* 220, 149-166.

Makarov, V.A., Schmidt, K.E., Castellanos, N.P., Lopez-Aguado, L., and Innocenti, G.M. (2008). Stimulus-dependent interaction between the visual areas 17 and 18 of the 2 hemispheres of the ferret (*Mustela putorius*). *Cereb Cortex* 18, 1951-1960.

Minciacchi, D., and Antonini, A. (1984). Binocularity in the visual cortex of the adult cat does not depend on the integrity of the corpus callosum. *Behav Brain Res* 13, 183-192.

Mizobe, K., Polat, U., Pettet, M., and Kasamatsu, T. (2001). Facilitation and suppression of single striate-cell activity by spatially discrete pattern stimuli presented beyond the receptive field. *Visual Neuroscience* 18, 377-391.

Nauhaus, I., Busse, L., Carandini, M., and Ringach, D. (2009). Stimulus contrast modulates functional connectivity in visual cortex. *Nature Neuroscience* 12, 70-76.

Nelson, J.I., and Frost, B.J. (1985). Intracortical facilitation among co-oriented, co-axially aligned simple cells in cat striate cortex. *Exp Brain Res* 61, 54-61.

Niessing, J., Ebisch, B., Schmidt, K., Niessing, M., Singer, W., and Galuske, R. (2005). Hemodynamic signals correlate tightly with synchronized gamma oscillations. *Science* 309, 948-951.

Payne, B.R., and Siwek, D.F. (1991). Visual-field map in the callosal recipient zone at the border between areas 17 and 18 in the cat. *Vis Neurosci* 7, 221-236.

Payne, B.R., Siwek, D.F., and Lomber, S.G. (1991). Complex transcallosal interactions in visual cortex. *Vis Neurosci* 6, 283-289.

Peiker, C., Wunderle, T., Eriksson, D., and Schimidt, K. (2011). The influence of callosal input on monocular and binocular responses in primary visual cortex. Paper presented at: Neuroscience Meeting Planner, Program (Washington, DC, USA).

Peiker, C., Wunderle, T., Eriksson, D., Schmidt, A., and Schmidt, K. (2013). An Updated Midline Rule: Visual Callosal Connections Anticipate Shape and Motion in Ongoing Activity across the Hemispheres. *Journal of Neuroscience* 33, 18036-18046.

Priebe, N.J., and Ferster, D. (2008). Inhibition, spike threshold, and stimulus selectivity in primary visual cortex. *Neuron* 57, 482-497.

Ptito, M., Faubert, J., Gjedde, A., and Kupers, R. (2003). Separate neural pathways for contour and biological-motion cues in motion-defined animal shapes. *Neuroimage* 19, 246-252.

Purves, D. (2004). *Neuroscience*, Third edn (U.S.A.: Sinauer Associates, Inc.).

Quiroga, R., Nadasdy, Z., and Ben-Shaul, Y. (2004). Unsupervised spike detection and sorting with wavelets and superparamagnetic clustering. *Neural Computation* 16, 1661-1687.

Rochefort, N., Buzas, P., Kisvarday, Z., Eysel, U., and Milleret, C. (2007). Layout of transcallosal activity in cat visual cortex revealed by optical imaging. *Neuroimage* 36, 804-821.

Rochefort, N.L., Buzás, P., Quenech'du, N., Koza, A., Eysel, U.T., Milleret, C., and Kisvárdy, Z.F. (2009). Functional selectivity of interhemispheric connections in cat visual cortex. *Cereb Cortex* 19, 2451-2465.

Roelfsema, P. (2006). Cortical algorithms for perceptual grouping. *Annual Review of Neuroscience* 29, 203-227.

- Roelfsema, P., Lamme, V., Spekreijse, H., and Bosch, H. (2002). Figure-ground segregation in a recurrent network architecture. *Journal of Cognitive Neuroscience* 14, 525-537.
- Roelfsema, P.R., Lamme, V.A., and Spekreijse, H. (2004). Synchrony and covariation of firing rates in the primary visual cortex during contour grouping. *Nat Neurosci* 7, 982-991.
- Rossi, A.F., Rittenhouse, C.D., and Paradiso, M.A. (1996). The representation of brightness in primary visual cortex. *Science* 273, 1104-1107.
- Rushmore, R., Payne, B., and Lomber, S. (2005). Functional impact of primary visual cortex deactivation on subcortical target structures in the thalamus and midbrain. *Journal of Comparative Neurology* 488, 414-426.
- Samonds, JM., Allison, JD., Brown, HA., Bonds, AB. (2003) Cooperation between area 17 neuron pairs enhances fine discrimination of orientation. *J Neurosci*. 23(6): 2416-25
- Schmidt, K., Lomber, S., and Innocenti, G. (2010). Specificity of Neuronal Responses in Primary Visual Cortex Is Modulated by Interhemispheric CorticoCortical Input. *Cerebral Cortex* 20, 2776-2786.
- Schmidt, K., and Löwel, S. (2002). Long-Range Intrinsic Connections in Cat Primary Visual Cortex. In *The Cat Primary Visual Cortex* (Academic Press), pp. 387-426.
- Schmidt, K.E. (2013). The visual callosal connection: a connection like any other? *Neural Plast* 2013, 397176.
- Schmidt, K.E., Kim, D.S., Singer, W., Bonhoeffer, T., and Löwel, S. (1997). Functional specificity of long-range intrinsic and interhemispheric connections in the visual cortex of strabismic cats. *J Neurosci* 17, 5480-5492.
- Schwabe, L., Obermayer, K., Angelucci, A., and Bressloff, P. (2006). The role of feedback in shaping the extra-classical receptive field of cortical neurons: A recurrent network model. *Journal of Neuroscience* 26, 9117-9129.
- Sengpiel, F., Sen, A., and Blakemore, C. (1997). Characteristics of surround inhibition in cat area 17. *Exp Brain Res* 116, 216-228.
- Shushruth, S., Mangapathy, P., Ichida, J.M., Bressloff, P.C., Schwabe, L., and Angelucci, A. (2012). Strong recurrent networks compute the orientation tuning of surround modulation in the primate primary visual cortex. *J Neurosci* 32, 308-321.
- Siapas, A.G., Lubenov, E.V., and Wilson, M.A. (2005). Prefrontal phase locking to hippocampal theta oscillations. *Neuron* 46, 141-151.

Sillito, A.M., Grieve, K.L., Jones, H.E., Cudeiro, J., and Davis, J. (1995). Visual cortical mechanisms detecting focal orientation discontinuities. *Nature* 378, 492-496.

Singer, W. (1993). Neuronal representations, assemblies and temporal coherence. *Prog Brain Res* 95, 461-474.

Singer, W. and Gray, Ch. (1995). Visual feature integration and the temporal correlation hypothesis. *Annu. Rev. Neurosci.* 18: 555-586.

Singer, W. (2009). Distributed processing and temporal codes in neuronal networks. *Cognitive Neurodynamics* 3, 189-196.

Sompolinsky, H., and Shapley, R. (1997). New perspectives on the mechanisms for orientation selectivity. *Curr Opin Neurobiol* 7, 514-522.

Stepanyants, A., Martinez, L.M., Ferecskó, A.S., and Kisvárday, Z.F. (2009). The fractions of short- and long-range connections in the visual cortex. *Proc Natl Acad Sci U S A* 106, 3555-3560.

Thiele, A. and Stoner, G. (2003). Neuronal synchrony does not correlate with motion coherence in cortical area MT. *Nature* 421 (6921): 366-70

Tiesinga, P., and Sejnowski, T. (2009). Cortical Enlightenment: Are Attentional Gamma Oscillations Driven by ING or PING? *Neuron* 63, 727-732.

Toth, L.J., Rao, S.C., Kim, D.S., Somers, D., and Sur, M. (1996). Subthreshold facilitation and suppression in primary visual cortex revealed by intrinsic signal imaging. *Proc Natl Acad Sci U S A* 93, 9869-9874.

Tusa, R., Palmer, L., and Rosenquist, A. (1978). Retinotopic organization of area-17 (striate cortex) in cat. *Journal of Comparative Neurology* 177, 213-235.

Tusa, R., Rosenquist, A., and Palmer, L. (1979). Retinotopic organization of area-18 and area-19 in the cat. *Journal of Comparative Neurology* 185, 657-678.

Vaadia, E., Haalman, I., Abeles, M., Bergman, H., Prut, Y., Slovin, H. and Aertsen, A. (1995) Dynamics of neuronal interactions in monkey cortex in relation to behavioural events. *Nature* 373: 515-518

Volgushev, M., Chistiakova, M., and Singer, W. (1998). Modification of discharge patterns of neocortical neurons by induced oscillations of the membrane potential. *Neuroscience* 83, 15-25.

Von der Malsburg, Ch. and W. Schneider, W. (1986). A neural cocktail-party processor. *Biological Cybernetics*. 54, 29-40

Watson, R.T., Valenstein, E., Day, A.L., and Heilman, K.M. (1984). The effect of corpus callosum lesions on unilateral neglect in monkeys. *Neurology* 34, 812-815.

Wunderle, T. (2012). Der Einfluss kortiko-kortikaler Verbindungen auf die Antwortheigenschaften von Neuronen im primären visuellen Kortex (Technischen Universität Darmstadt).

Wunderle, T., Eriksson, D., and Schmidt, K.E. (2013). Multiplicative mechanism of lateral interactions revealed by controlling interhemispheric input. *Cereb Cortex* 23, 900-912.

Wörgötter, F., and Holt, G. (1991). Spatiotemporal mechanisms in receptive fields of visual cortical simple cells: a model. *J Neurophysiol* 65, 494-510.

Yamahachi, H., Marik, S., McManus, J., Denk, W., and Gilbert, C. (2009). Rapid Axonal Sprouting and Pruning Accompany Functional Reorganization in Primary Visual Cortex. *Neuron* 64, 719-729.

Yazgan, M.Y., Wexler, B.E., Kinsbourne, M., Peterson, B., and Leckman, J.F. (1995). Functional significance of individual variations in callosal area. *Neuropsychologia* 33, 769-779.

Yousef, T., Bonhoeffer, T., Kim, D.S., Eysel, U.T., Tóth, E., and Kisvárday, Z.F. (1999). Orientation topography of layer 4 lateral networks revealed by optical imaging in cat visual cortex (area 18). *Eur J Neurosci* 11, 4291-4308.

Zipser, K., Lamme, V.A., and Schiller, P.H. (1996). Contextual modulation in primary visual cortex. *J Neurosci* 16, 7376-7389.

# Neuronal Assembly Detection and Cell Membership Specification by Principal Component Analysis

**Vítor Lopes-dos-Santos<sup>1,2,\*</sup>, Sergio Conde-Ocazinez<sup>1,2</sup>, Miguel A. L. Nicolelis<sup>2,3</sup>, Sidarta T. Ribeiro<sup>1,2</sup>, Adriano B. L. Tort<sup>1,2\*</sup>**

**1** Brain Institute, Federal University of Rio Grande do Norte, Natal, Rio Grande do Norte, Brazil, **2** Edmond and Lily Safra International Institute of Neuroscience of Natal, Natal, Rio Grande do Norte, Brazil, **3** Duke University Center for Neuroengineering and Department of Neurobiology, Duke University, Durham, North Carolina, United States of America

## Abstract

In 1949, Donald Hebb postulated that assemblies of synchronously activated neurons are the elementary units of information processing in the brain. Despite being one of the most influential theories in neuroscience, Hebb's cell assembly hypothesis only started to become testable in the past two decades due to technological advances. However, while the technology for the simultaneous recording of large neuronal populations undergoes fast development, there is still a paucity of analytical methods that can properly detect and track the activity of cell assemblies. Here we describe a principal component-based method that is able to (1) identify all cell assemblies present in the neuronal population investigated, (2) determine the number of neurons involved in ensemble activity, (3) specify the precise identity of the neurons pertaining to each cell assembly, and (4) unravel the time course of the individual activity of multiple assemblies. Application of the method to multielectrode recordings of awake and behaving rats revealed that assemblies detected in the cerebral cortex and hippocampus typically contain overlapping neurons. The results indicate that the PCA method presented here is able to properly detect, track and specify neuronal assemblies, irrespective of overlapping membership.

**Citation:** Lopes-dos-Santos V, Conde-Ocazinez S, Nicolelis MAL, Ribeiro ST, Tort ABL (2011) Neuronal Assembly Detection and Cell Membership Specification by Principal Component Analysis. PLoS ONE 6(6): e20996. doi:10.1371/journal.pone.0020996

**Editor:** Matjaz Perc, University of Maribor, Slovenia

**Received** April 11, 2011; **Accepted** May 17, 2011; **Published** June 15, 2011

**Copyright:** © 2011 Lopes-dos-Santos et al. This is an open-access article distributed under the terms of the Creative Commons Attribution License, which permits unrestricted use, distribution, and reproduction in any medium, provided the original author and source are credited.

**Funding:** This work was supported by Coordenação de Aperfeiçoamento de Pessoal de Nível Superior, Conselho Nacional de Desenvolvimento Científico e Tecnológico, and Associação Alberto Santos Dumont para Apoio à Pesquisa. The funders had no role in study design, data collection and analysis, decision to publish, or preparation of the manuscript.

**Competing Interests:** The authors have declared that no competing interests exist.

\* E-mail: vtlsantos@gmail.com (VL-d-S); tort@neuro.ufrn.br (ABL)

• These authors contributed equally to this work.

## Introduction

Hebb's seminal work constitutes a landmark of modern neuroscience [1]. His theory proposes detailed neural mechanisms for the processing and learning of information, from the molecular, cellular and circuit levels to the emergence of complex cognitive functions. According to Hebb's hypothesis, the recurrent co-activation of a subset of neurons would increase the efficiency of their connections, leading to the formation of a cell assembly. Therefore, synchronization of spike times would play a critical role in the creation of new assemblies [2,3,4,5,6]. In this context, a cell assembly is defined as a group of neurons that fire together and wire together. Due to the increased strength of the connections linking members of the assembly, activation of some of its neurons would trigger the activation of the entire neuronal group, leading to pattern completion [7,8,9]. Hebb also postulated that the activation of a cell assembly can lead to the sequential activation of other assemblies, a phenomenon he termed as phase-sequences, and proposed to underlie complex brain computations (see also [10,11,12]). In line with this view, neocortical and hippocampal information has been shown to be widely distributed over neuronal populations, rather than encoded by the activity of highly specialized cells [13,14,15,16,17,18,19].

The actual investigation of Hebbian cell assemblies and their dynamics is only beginning to be possible, thanks to major technological advances that allow the simultaneous and chronic recording of large neuronal populations [20,21,22]. In parallel with these advances, mathematical methods have been developed to address Hebb's hypotheses in experimental data, such as template matching of neuronal population activity [23,24,25] and the detection of precise multi-neuron firing [26,27,28,29,30]. Powerful methods for the detection of neuronal co-activation based on Principal Component Analysis (PCA) were also described [31,32,33], which have recently been extended to incorporate strong statistical support [34]. The latter framework is able to reliably detect the presence of cell assemblies and to assess ensemble activation with high temporal resolution based on the projection of network activity on the principal components (PCs) of the neuronal correlation matrix (see next section for a definition).

Despite its successful initial applications [32,35,36], the PCA-based method presents some limitations. First, it does not identify which specific neurons compose the detected assemblies. In addition, as demonstrated in the present work, the use of individual PCs in order to represent assembly activity patterns is misleading when there are neurons shared by different assemblies. As a consequence, in these cases the projection of neuronal activity

based on PCs does not match the actual time course of individual assembly activation. Since it is currently believed that most, if not all, neocortical and hippocampal neurons take part in multiple assemblies (see Discussion), such limitation is an important one.

To address these gaps, we present here an exploration of some of the key properties of the PCA method for assembly detection, and propose critical modifications of the current framework. First, we show that the number of assemblies and assembly neurons can be computed from the analysis of the eigenvalues of the neuronal correlation matrix. We then show that the subspace spanned by the PCs can reveal which neurons compose the detected assemblies. We go on to show how the time course of the activity of individual assemblies can then be estimated, even when different cell assemblies have a subset of common neurons. Finally, we show that our method can properly detect, track and specify the neuronal membership of neocortical and hippocampal assemblies recorded from behaving rats.

## Results

First we briefly outline the general framework as proposed in [31,32,34,35]. Figure 1A shows an example of neuronal population activity represented by means of a standard spike rastergram plot, in which each mark denotes the firing of an action potential by a neuron (the y-axis indicates the neuron labels). The procedure begins by binning the spike rastergram into non-overlapping, short time windows (referred to as bins) and counting the number of spikes in each bin, as indicated in Figure 1B. In this way, the rows of the resulting matrix represent neuronal units, and the columns represent the time bins. More specifically, the element  $a_{ij}$  denotes the number of spikes of the  $i$ th neuron in the  $j$ th bin (Figure 1B inset). For the sake of generality, in this work we use the “bin number” (“bin #”) as our arbitrary unit of time. Next, the binned spike activity is z-scored in order to normalize the spike rate of each neuron (Figure 1C). Thus, the rows of the normalized matrix are vectors with zero mean and unit variance. The autocorrelation matrix of the normalized spike activity is then computed (Figure 1D); each entry  $\hat{y}_{ij}$  of the autocorrelation matrix is the Pearson correlation coefficient ( $\hat{r}$ ) between the rows  $i$  and  $j$  of the matrix shown in Figure 1C (i.e., a correlation between two spike rate vectors).

The next steps of the method involve the computation of the eigenvalues of the autocorrelation matrix (Figure 1E) and the associated eigenvectors (Figure 1F), which in this context are referred to as Principal Components (PCs). Finally, the PCs associated with significant eigenvalues (see below) are used to track the activity of cell assemblies in each time bin (Figure 2A).

An important question is to know when the correlation coefficient of the spike activity of two neurons can be considered statistically significant for a given dataset. To this end, a statistical threshold that separates non-significant correlations from values above chance is needed. Instead of using exhaustive surrogate methods [37,38,39,40,41,42], Peyrache et al. elegantly addressed this problem by analyzing the distribution of the eigenvalues of the autocorrelation matrix [34,35]. From random matrix theory, it can be demonstrated that the eigenvalues of an autocorrelation matrix computed from a matrix with statistically independent rows (in our case, neurons with independent activity) follow the so-called Marčenko-Pastur distribution [43]. Since the goal is to identify ensemble activity, i.e. groups of neurons with correlated firing, the theoretical upper limit provided by the Marčenko-Pastur distribution can be used as statistical threshold. Thus, if there are groups of significantly correlated neurons in the population recorded, some eigenvalues will lie above this statistical

threshold. Furthermore, the PCs associated with significant eigenvalues can be used to track assembly activity. This is accomplished by projecting the normalized spike activity matrix using projector operators computed from the PCs, resulting in a unidimensional signal representing the time series of ensemble activity.

Using simulated data, we show in Figure 2A that the activation time course computed as described above is able to represent the activity of specific cell assemblies in some cases. However, as shown in Figure 2B, this approach is unable to separate the activity of individual assemblies when the neuronal population is composed of assemblies with overlapping cells. Note in Figure 2A that the estimated time courses of the activation strength correspond to increases of firing rate of specific subsets of neurons, as desired. However, for the case depicted in Figure 2B, the projection of population activity using the PCs does not separate the activity of the two cell assemblies. This constitutes an important limitation since the existence of assemblies with shared neurons is expected (see Discussion).

In the following sections we explore in more detail the general characteristics of this method, and propose modifications to allow tracking the activity of individual assemblies even when they share neurons. We also show that it is possible to precisely identify the neurons participating in each cell assembly.

## Marčenko-Pastur distribution and the null hypothesis of independent neuronal activity

We start by exploring example cases of networks where no organized neuronal activity is present, that is, when there is no cell assembly in the network. As already introduced in the previous section, the eigenvalues of an autocorrelation matrix computed from a matrix with independent rows follow the Marčenko-Pastur distribution (see Methods for its formula). In order to illustrate this prediction, we show in Figure 3A–C three examples of random network activity differing in the number of neurons and time windows analyzed (i.e., the total number of bins). Each neuron is modeled as an independent Poissonian process (mean = 1 spike/bin). The predicted distribution of eigenvalues is shown below the corresponding network along with its empirical eigenvalues histogram. As expected, the actual eigenvalues follow the Marčenko-Pastur distribution. Note that the theoretical distribution has lower variance for greater values of the ratio  $q = N_{\text{bins}}/N_{\text{neurons}}$ .

We next performed a systematic parametric study of matrices with independent rows to investigate this property further. To this end, we defined “accuracy” as the percentage of eigenvalues that lie within theoretical bounds, that is, 100% accuracy means that all eigenvalues are within the limits predicted by the Marčenko-Pastur distribution. In other words, accuracy assesses the performance of the use of the theoretical bounds in determining the absence of cell assemblies in the network.

Figure 3D shows accuracy as a function of network size and total number of bins. Notice that, for a given network size, higher levels of accuracy are achieved with a higher number of time bins. In fact, as better seen in Figure 3E, accuracy is highly dependent on the condition  $q = N_{\text{bins}}/N_{\text{neurons}} > 1$ , i.e., the number of analyzed bins has to be greater than the number of neurons in the network. Figure 3F displays the results shown in Figure 3D for three specific network sizes. Similar results were obtained for different firing rates and also for the more realistic case in which the mean firing rate of each neuron differs from the mean rate of other neurons (data not shown). This latter result was expected since the firing rates are normalized.

Overall, we conclude that the theoretical limits predicted by the Marčenko-Pastur distribution can be used as the null hypothesis of

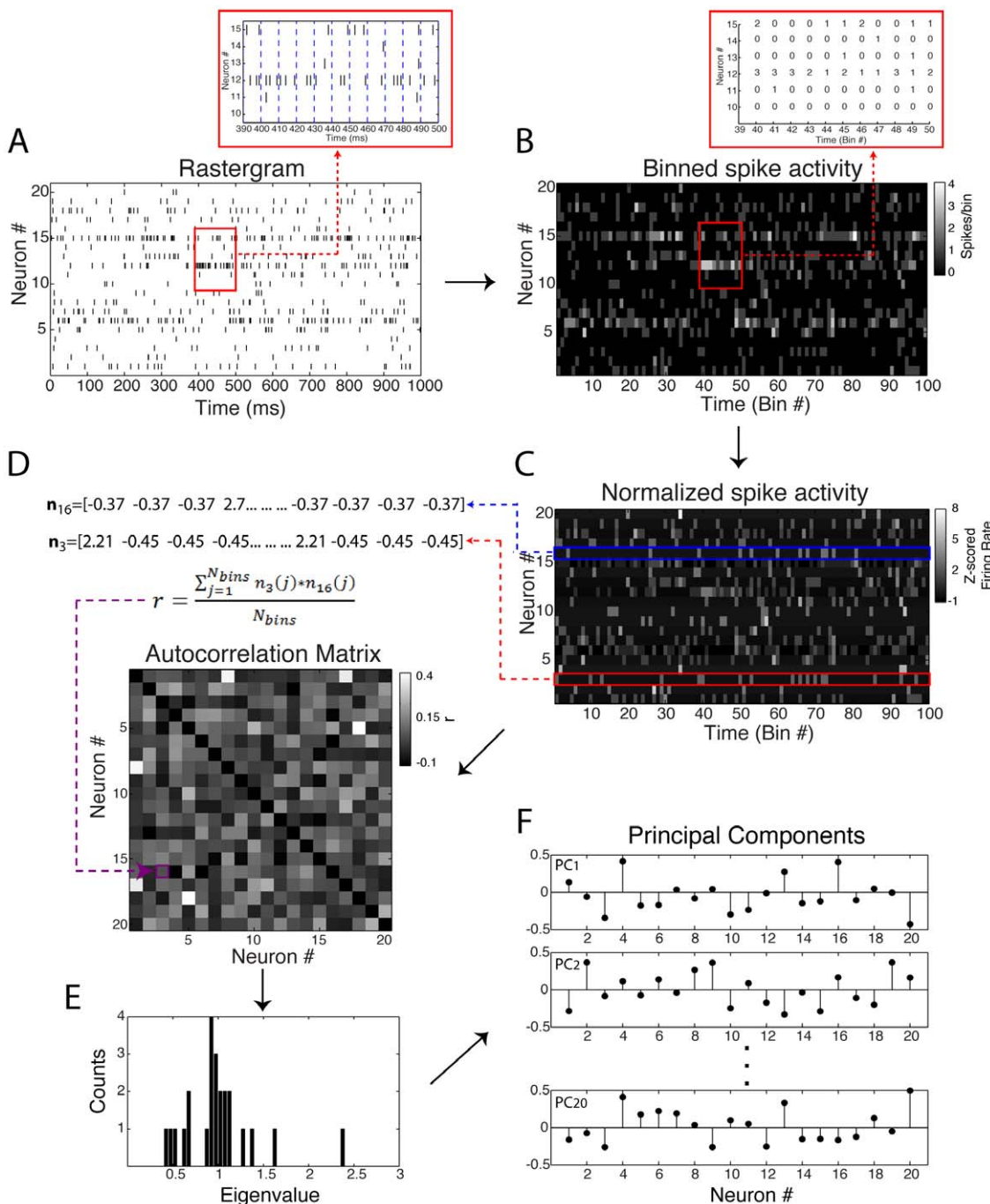


**Figure 1. Original method overview.** (A) Raster plot activity. Each row represents a neuron; marks denote an action potential and x-axis represents time. Panel inset shows the binning procedure into non-overlapping time windows. (B) Binned spike activity matrix obtained from raster plot in A. Each element is the count of the number of spikes in a given bin. (C) Z-scored binned spike activity matrix obtained by mean and variance normalization of the matrix in B. (D) Autocorrelation matrix (ACM) of the normalized binned spike activity in C. Each element denotes the linear correlation between two neurons. The main diagonal is set to zero for clearer visualization. (E) Eigenvalue histogram of the ACM shown in D. (F) Principal components (PCs) of the ACM, which are the eigenvectors associated with the eigenvalues shown in E. PCs are ordered in respect to their eigenvalues, i.e., the PC1 is associated with the highest eigenvalue and so on.  
doi:10.1371/journal.pone.0020996.g001

independent neuronal activity, as long as the number of bins analyzed is higher than the number of neurons in the network. In the next section, we show how we can also use this theoretical distribution to determine the precise number of cell assemblies in the network.

Eigenvalues outside theoretical bounds mark the number of cell assemblies and assembly neurons

We have shown above that eigenvalues of autocorrelation matrices computed from independent neuronal activity remain

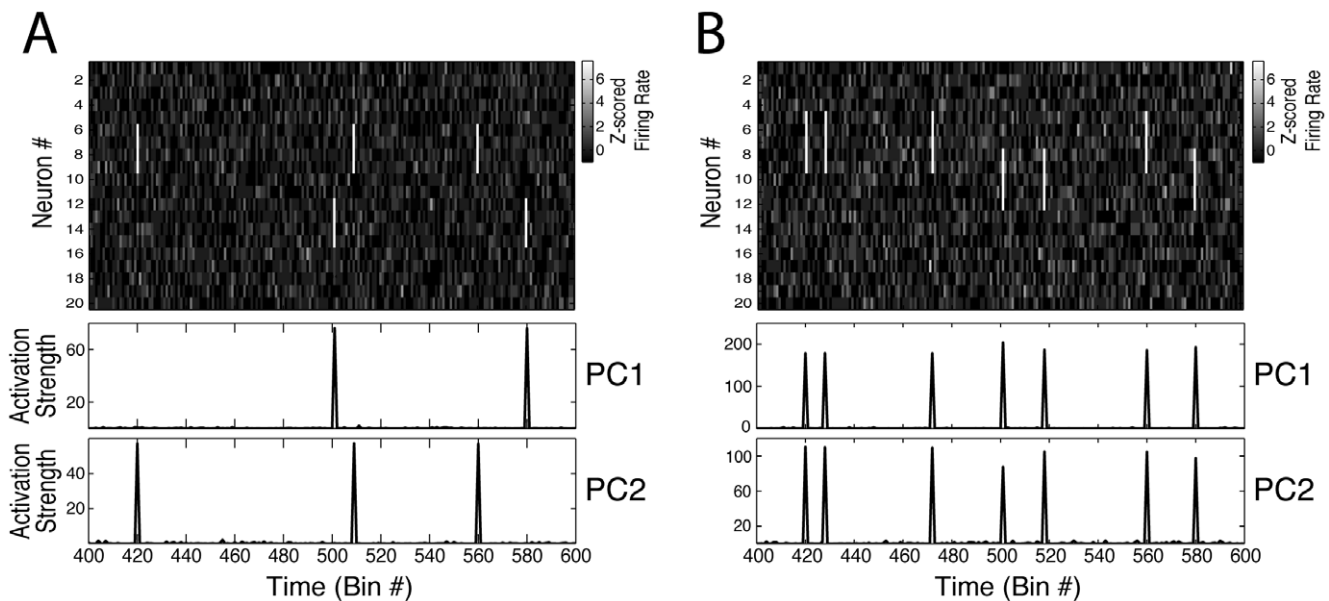


**Figure 2. PCs do not always isolate the activity of different cell assemblies.** (A) Top panel shows a binned spike activity matrix with 20 neurons (modeled as Poissonian processes) and 8000 time bins. Two cell assemblies were simulated in the network, each having four neurons (Assembly 1 neurons: #6, #7, #8, #9; Assembly 2 neurons: #12, #13, #14, #15). Neurons in the same assembly were set to fire together six times above their mean firing rate at 0.5% of the bins. Bottom panels show the estimated time course of ensemble activity obtained by the projection of the binned spike activity using the projector operator defined as the outer product of the PCs (see Methods). Note that PC1 marks the activations of Assembly 2, and PC2 marks the activations of Assembly 1. (B) Same as A, but with assemblies sharing neurons (Assembly 1 neurons: #5, #6, #7, #8, #9; Assembly 2 neurons: #8, #9, #10, #11, #12). Note that for this example this framework fails to isolate the activity of individual assemblies. doi:10.1371/journal.pone.0020996.g002

within predicted limits as long as the condition  $q > 1$  is satisfied. Now we go further to show that the number of eigenvalues above the theoretical upper limit not only indicates the presence of ensemble activity, but it is also an accurate estimation of the number of cell assemblies in the network.

In Figure 4A two examples of neuronal network activity are shown. Neurons were modeled as Poissonian processes as in Figure 3, but, in addition, simulated assembly activity was added to the network. Assembly activations were modeled as an increase of the firing rates of a subset of neurons in specific bins. More specifically, in these “activation bins”, neurons were set to fire between 6 and 9 spikes, uniformly distributed. Both examples have 32 neurons and 8000 time bins. In each example, the mean firing rates (over all time bins) of cell assembly neurons were not necessarily higher than those of the other neurons in the network (Figure 4A, leftmost panels). In other words, the specific bins of assembly activation did not lead to a considerable net change in the average spike frequency of these neurons. In Figure 4A we depict a period of 150 bins in which assembly activations can be seen (second panels from left), along with the autocorrelation matrix of the simulated network (third panels from left); the theoretical eigenvalue distribution and the empirical eigenvalue histogram are also shown (top and bottom rightmost panels, respectively).

In the first example, a cell assembly with four neurons (neurons #7, #8, #9 and #10) is present in the network. Neurons have independent activity, with the exception of the cell assembly neurons that have higher firing rate in 0.5% of the bins randomly selected (i.e., the activation bins; cell assembly neurons have independent activity in the other bins). A simple visual inspection of the autocorrelation matrix already reveals higher correlations among cell assembly neurons. Importantly, notice that one eigenvalue of the empirical distribution lies above the upper limit predicted for independent neuronal activity in this example. In the

second example, three cell assemblies were added to the network. Notice that three eigenvalues fall above the theoretical upper limit in this case. These results therefore suggest that the number of eigenvalues above the Marcenko-Pastur distribution mark the number of cell assemblies in the network. We next performed a parametric analysis to investigate in more detail such property.

In Figure 4B, we analyze networks with different numbers of assemblies and different firing rates during activation bins (“activation firing rate”). We simulated networks with 40 neurons (mean spike rate = 1 spike/bin) and 8000 time bins; assemblies were composed by 4 neurons and set to be active in 0.5% of the bins. Each data point in Figure 4B corresponds to a network with a given level of activation firing rate (labeled by colors) and number of assemblies (varying from 1 to 10, as indicated in the x-axis). The number of eigenvalues above the theoretical upper limit is plotted as a function of the number of assemblies for different activation firing rates. Note that a perfect match between the number of eigenvalues above the upper limit and the number of assemblies in the network is indicated by  $\beta = 1$  in the linear fit  $y = \alpha + \beta x$ . We found that the number of eigenvalues above the upper limit underestimated the number of assemblies in the network ( $\beta < 1$ ) in cases in which assembly activations had a firing rate below 5; on the other hand, all cases with activation firing rate equal or above 5 presented a perfect match ( $\beta = 1$ ). Taken together, these results suggest that a minimal activation firing rate is required for the proper detection of the number of assemblies.

Our next step was to conduct exhaustive simulations to investigate the requirements for reaching the criterion  $\beta = 1$ . Figure 4C shows the minimal assembly activation firing rate required to achieve such criterion as a function of background firing rate and number of analyzed bins. In the left panel, the minimal activation firing rate is shown in absolute values, while in the right panel it is expressed as a ratio relative to the background firing rate.

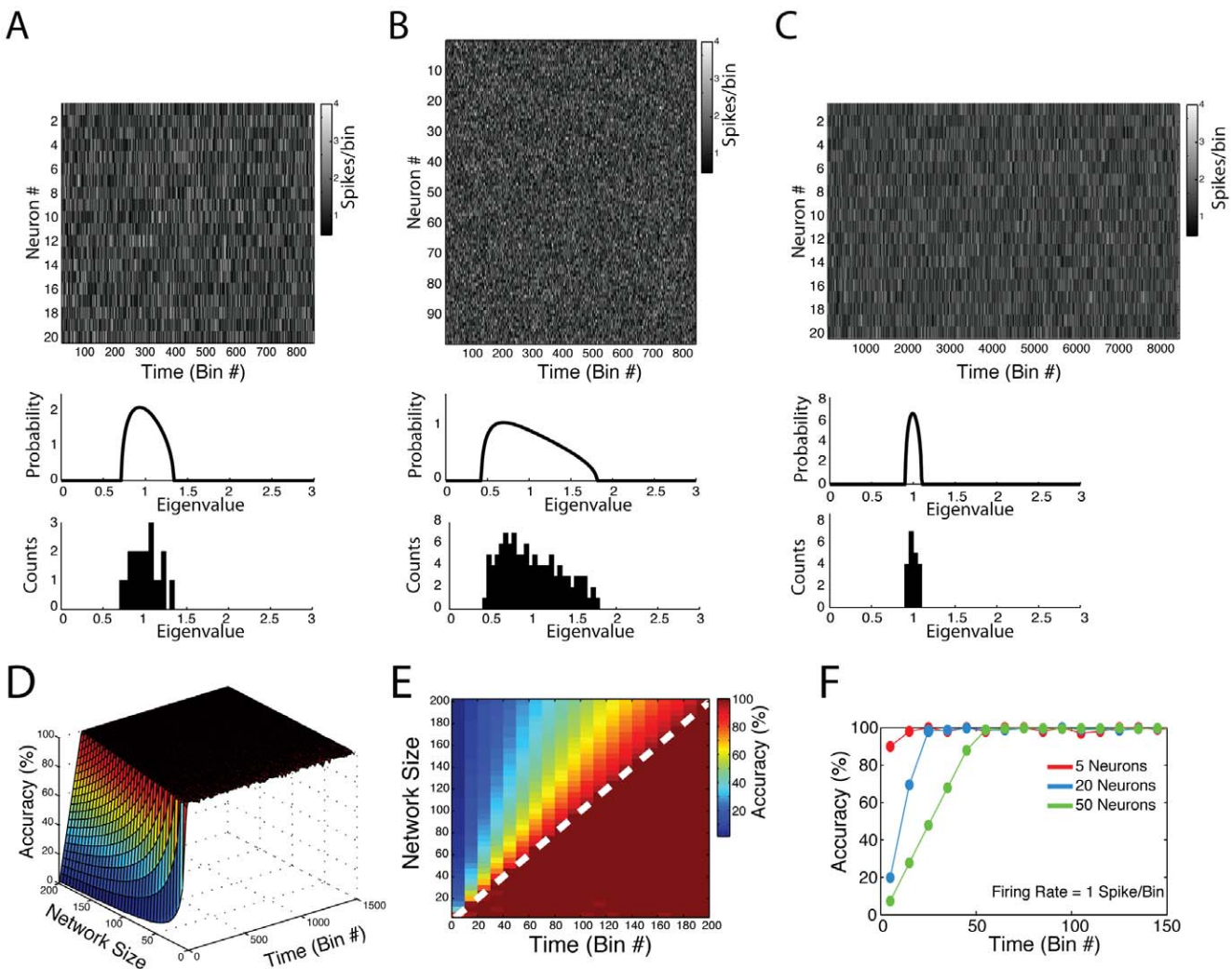


**Figure 3. Eigenvalues of autocorrelation matrices derived from the activity of independent neurons fall within theoretical bounds.** (A) Top Panel: Binned spiking activity of 20 independent neurons. Each neuron was simulated as following a Poisson process (mean = 1 spike/bin). Middle Panel: Theoretical Marčenko-Pastur distribution. Bottom Panel: Histogram of eigenvalues obtained from the autocorrelation matrix computed from the neuronal activity shown in the top panel. (B,C) Similar panels as in A but for network activities presenting a greater number of neurons (B) or bins (C). Notice that the eigenvalues follow the Marčenko-Pastur distribution in all cases, and that the width of the predicted distribution is dependent on the ratio  $N_{\text{neurons}}/N_{\text{bins}}$ , where  $N_{\text{neurons}}$  = number of neurons and  $N_{\text{bins}}$  = number of bins. (D) Percentage of eigenvalues falling within Marčenko-Pastur theoretical bounds as a function of network size and number of time bins. For each parameter set, neurons were simulated as independent Poisson processes (mean = 1 spike/bin). Values represent the mean over 20 simulations. (E) Top-down view of the surface in D. Notice that virtually 100% accuracy occurs when  $N_{\text{bins}} > N_{\text{neurons}}$ . Dashed white line denotes  $N_{\text{bins}} = N_{\text{neurons}}$ . (F) Transections of the surface in D obtained for three different network sizes.

doi:10.1371/journal.pone.0020996.g003

Note that for a higher number of bins analyzed, a lower activation firing rate is required for a perfect match between the number of assemblies and of the eigenvalues above the upper limit. Figure 4D illustrates the dependence of  $\beta=1$  on the number of assembly activation events. We studied network activities with 4000 (Figure 4D left panel) and 8000 (Figure 4D right panel) bins for four different “activation frequencies” (number of activation bins/number of time bins), and we show the minimal activation firing rate for  $\beta=1$  as a function of background activity. Notice that, as the activation frequency gets higher, lower assembly activation firing rates are sufficient for  $\beta=1$ . Overall, these simulations show that the number of eigenvalues above the theoretical bound is related to the number of assemblies present in the network. The efficiency of such estimation depends on how many bins the assembly neurons are correlated and how high this correlation is.

Next, we studied the eigenvalues that fall below the lower theoretical bound. Inspection of Figure 4A suggests that the number of eigenvalues below the predicted limit for independent activity increases when more assemblies are added to the network. In Figure 5, we show that, in fact, the total number of eigenvalues outside the theoretical distribution (below or above) is a good estimation of the total number of neurons involved in ensemble activity. More specifically, in Figure 5A we show three examples of networks with 40 simulated neurons and 8000 analyzed bins. A cell assembly was added to the network (active in 0.5% of the bins) and the number of neurons composing the ensemble was varied (4, 8 and 12 assembly neurons from top to bottom panels). The eigenvalue histograms shown in Figure 5A indicate that the number of eigenvalues below the predicted limit increases with increasing the number of cell assembly neurons; in fact, for the 3

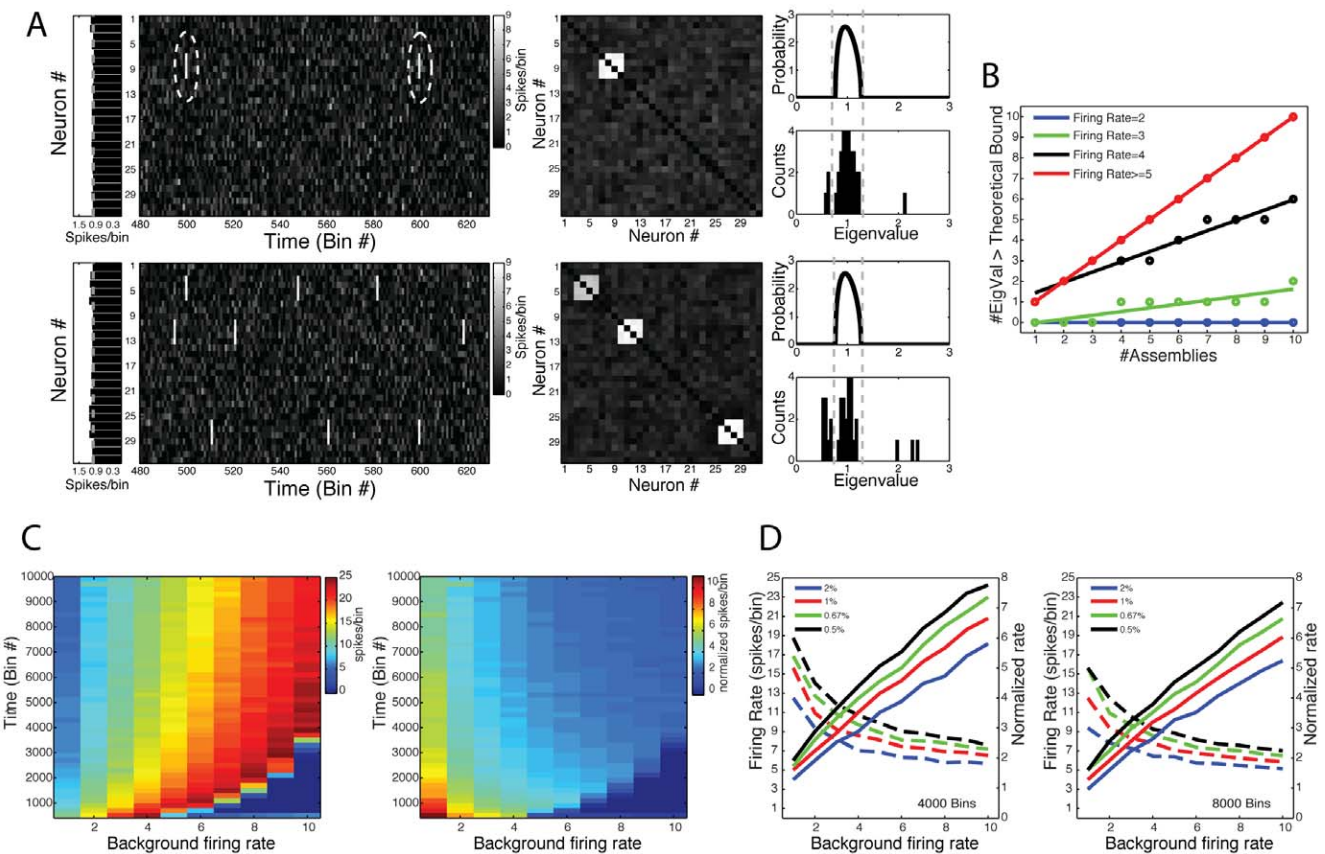


**Figure 4. Eigenvalues above theoretical bound mark the number of cell assemblies.** (A) Top: (Left panels) Shown are binned spiking activity of a network composed of 32 neurons (second panel), along with the average firing rate of each neuron (first panel). Total simulation time was 8000 bins; neurons were modeled as possessing a Poissonian firing rate (mean = 1 spike/bin). In order to simulate a cell assembly, we set a group of neurons to activate simultaneously at 0.5% of the bins (firing rate within activation events = 6–9 spikes/bin). To facilitate visual inspection, neighbor neurons were chosen as composing the cell assembly (neurons #7, #8, #9, #10; dashed circle). (Middle Panel) Network correlation matrix. Notice a cluster of correlated activity corresponding to the cell assembly. (Right Panels) Theoretical eigenvalues distribution for independent neuronal activity (top panel), and the eigenvalues histogram computed from the simulated network (bottom panel). Notice that 1 eigenvalue lies above the theoretical upper limit predicted for random activity. Bottom: Same as above, but for a network presenting three cell assemblies (Cell assembly 1: neurons #3, #4, #5, #6; Cell assembly 2: #10, #11, #12, #13; Cell assembly 3: neurons #26, #27, #28, #29). Notice that three eigenvalues lie above the theoretical bound. (B) Number of eigenvalues above the theoretical bound as a function of the number of cell assemblies in the network for different values of firing rate during cell assembly activation events. Networks were composed of 40 neurons; neurons were simulated as Poissonian processes (background mean = 1 spike/bin). Total simulation time was 8000 bins; assembly activation frequency was set to 0.5% of the bins. Each cell assembly was composed by 4 neurons (non-overlapping). Colored lines denote the linear fit  $y = \alpha + \beta x$  for each activation firing rate studied. Notice that the higher the firing rate within activation bins, the higher the slope coefficient ( $\beta$ ). If the firing rate is high enough,  $\beta$  equals 1, which characterizes the regimes in which the number of eigenvalues perfectly corresponds to the number of cell assemblies. Each data point represents a single simulation result. (C) Pseudocolors denote the minimal firing rate within activation bins leading to  $\beta$  equal to 1 as a function of the background mean firing rate (x-axis) and total number of time bins (y-axis). Results are expressed as absolute values (left) and as a ratio relative to the background firing rate (right). Assembly activation frequency was set to 0.5% of the bins. Networks were composed by 40 neurons, and each cell assembly was composed by 10 neurons. For each parameter set, values represent the mean over 20 simulations. (D) Left panel: Black line represents a transection of the result in C for network activities of 4000 time-bins. Other colored lines represent equivalent results obtained for different frequencies of cell assembly activation, as labeled. Notice that the higher the frequency of cell assembly activation, the lower the minimal firing rate leading to  $\beta$  equal to 1. Colored dashed lines represent the same result but as a ratio to the background firing rate. Right panel: Similar results as before, but for a network activity composed of 8000 time-bins.

doi:10.1371/journal.pone.0020996.g004

examples, the total number of eigenvalues outside the theoretical distribution perfectly matched the number of cell assembly neurons. In Figure 5B we show that this property depends on the assembly activation firing rate. We again used exhaustive simulations in order to assess the robustness of this estimation. Figure 5C shows the number of eigenvalues outside predicted limits as a function of assembly activation firing rate and analyzed bins; the result is expressed as a ratio of the number of the neurons composing the assembly (# outer eigenvalues/# assembly neurons). Note that a virtually perfect estimation (ratio = 1) is

approached as the activation firing rate and the number of analyzed bins increase. Figure 5D shows the minimal activation firing rate for ratio = 1 as a function of the number of analyzed bins. We show this relation for different assembly activation frequencies and for different assembly sizes. While the estimation does not depend significantly on the number of neurons in the assembly, it is improved if the assembly is active in more bins. Similar findings were obtained in networks composed by multiple assemblies, even when some neurons were shared by two or more assemblies (simulations not shown, but see Figures 6 and 7).

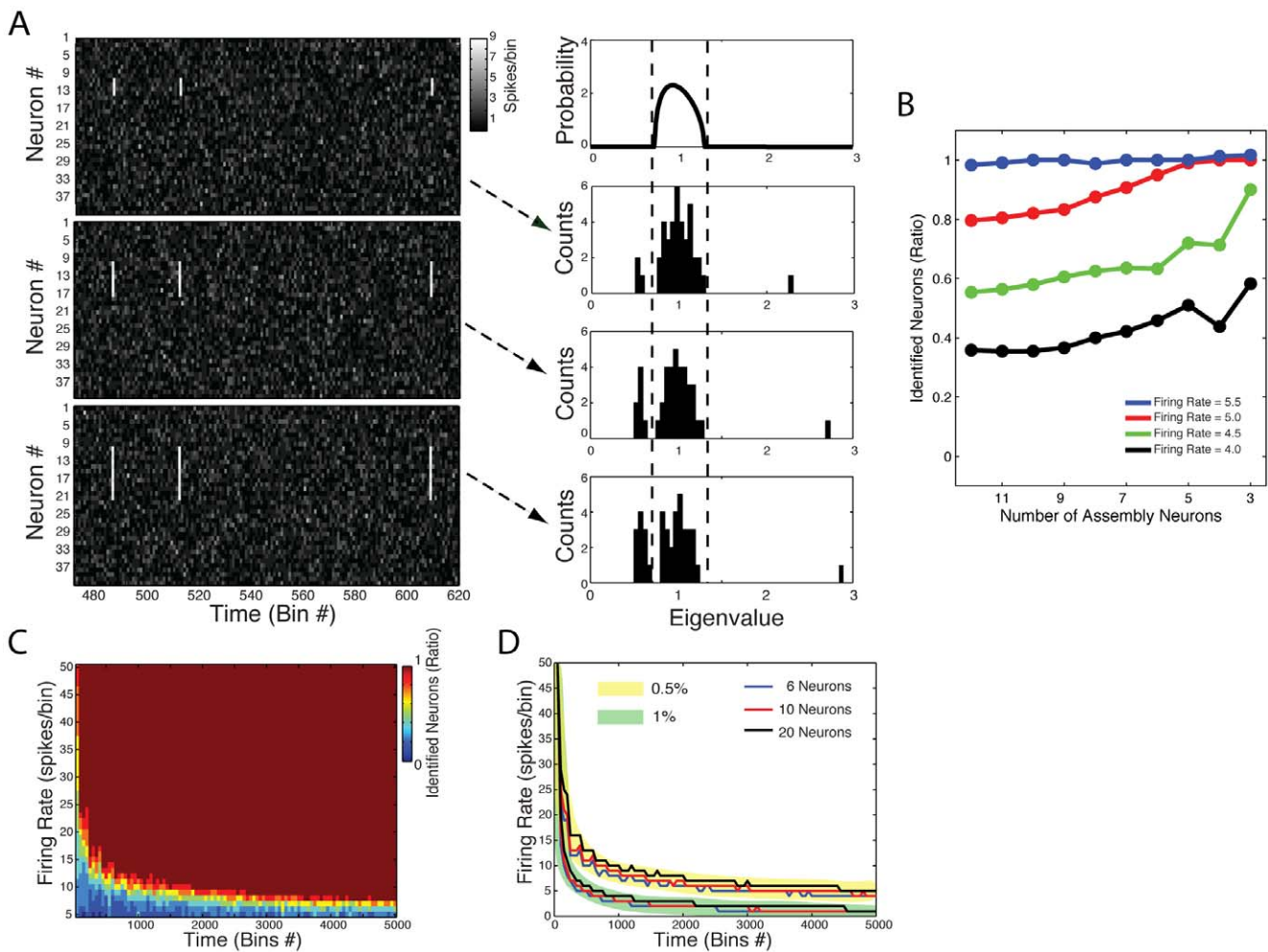


**Figure 5. The number of eigenvalues lying outside the theoretical distribution limits corresponds to the number of cell assembly neurons.** (A) Shown are the binned spiking activity matrices of networks composed of 40 neurons (left panels), along with the predicted eigenvalues distribution for independent neuronal activity (top right panel) and the actual eigenvalue histogram (bottom right panels). Total simulation time was 8000 bins; neurons were modeled as possessing a Poissonian firing rate (mean = 1 spike/bin). The 3 cases depicted differ in the number of neurons that compose the cell assembly. Notice that, for all cases, the number of eigenvalues outside the theoretical limits (dashed lines) matches the number of neurons in the cell assembly. (B) Ratio of the number of eigenvalues outside theoretical limits to the number of cell assembly neurons (ratio = 1 means that the number of significant eigenvalues perfectly corresponds to the number of cell assembly neurons). Different data points denote the mean over 20 simulations for different number of cell assembly neurons (x-axis) and activation firing rates (colored lines), as labeled. Networks were composed of 40 neurons; neurons were simulated as Poissonian processes (background mean = 1 spike/bin). Total simulation time was 8000 bins; assembly activation frequency was set to 1% of the bins. (C) Pseudocolors denote the ratio of the number of eigenvalues outside theoretical limits to the number of cell assembly neurons as a function of the activation firing rate and total time bins. Values represent the mean over 20 simulations. Networks were composed of 40 neurons; the cell assembly was made of 10 neurons set to activate at a frequency of 0.5% of the bins. Notice that for each activation firing rate, a perfect estimation of the number of cell assembly neurons (ratio = 1) is achieved if the number of bins analyzed is large enough. (D) Minimal activation firing rate required for a perfect match between the number of eigenvalues outside predicted limits and the number of cell assembly neurons as a function of the number of analyzed bins. Different lines represent different cases varying in the number of neurons in the assembly and in the frequency of cell assembly activation, as labeled.

doi:10.1371/journal.pone.0020996.g005

In conclusion, we observed that the empirical distribution of eigenvalues not only indicates the presence of ensemble activity in the network, but can also be used to estimate the number of cell assemblies present in the network as well as the number of neurons involved in ensemble activity. In the next section we show how this information can be used to identify which neurons belong to each detected assembly.

#### Identification of cell assemblies and time course of their activation

So far we have shown that eigenvalues of autocorrelation matrices that are higher than a well-established statistical threshold

have a strong relation with subsets of correlated neurons. Since these eigenvalues are by definition associated with PCs, it is reasonable to expect that these vectors also carry information about ensemble activity. In order to show how they can be used to identify assemblies in a network (in terms of which neurons compose them) we created a simulated network as an illustrative example. Neurons were again modeled as Poissonian processes, but with different mean spike rates (uniformly distributed between one and five spikes/bin). In addition, we set every neuron to fire 6 times above their mean rate at 0.5% of the bins. Two groups of neurons (cell assembly 1 neurons: #5, #15, #21; cell assembly 2 neurons: #12, #23) had these firing peaks at the same bins,

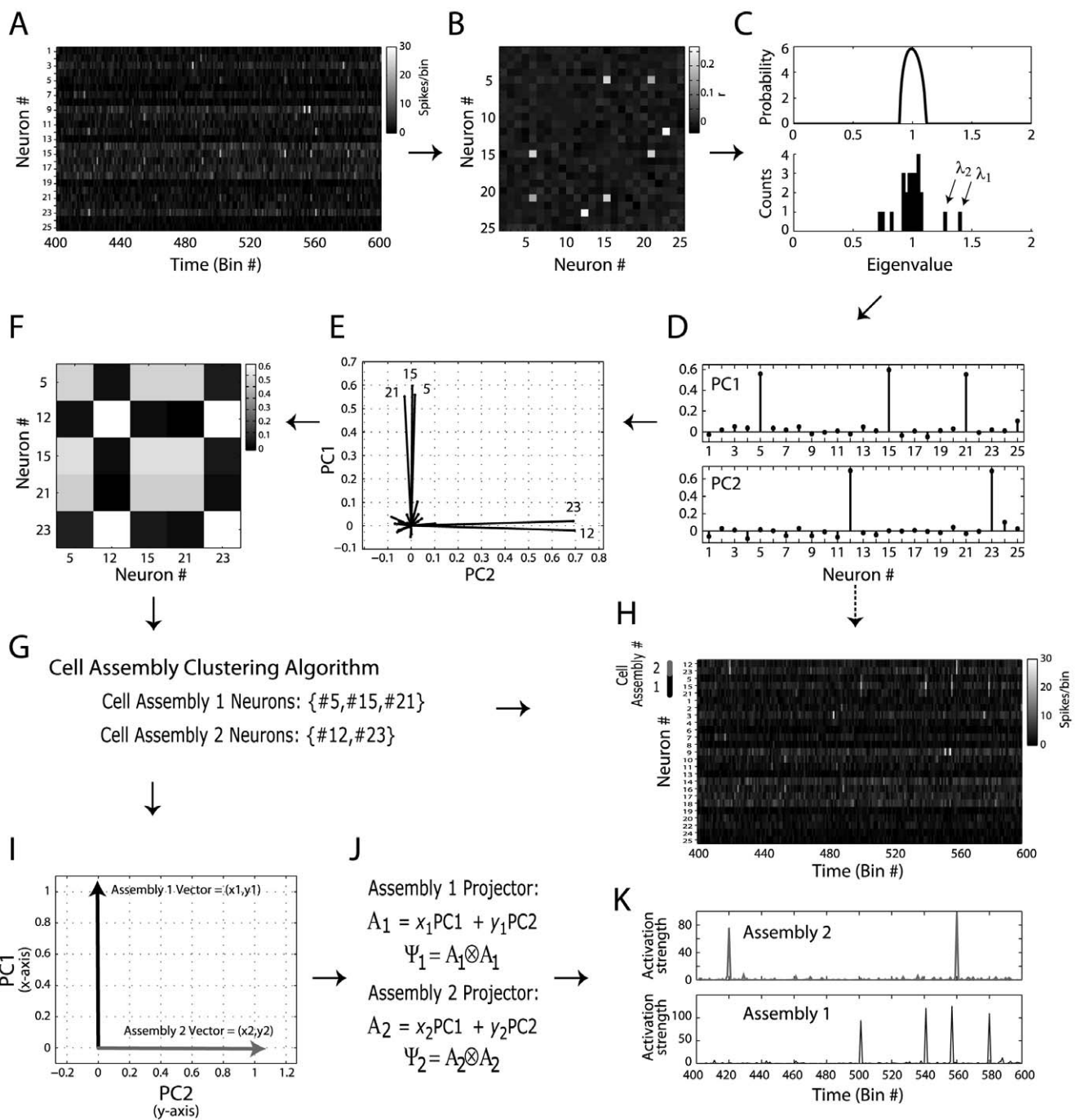


**Figure 6. Principal component-based analysis identifies cell assembly neurons and the time course of their activation.** (A) Binned spiking activity of a network composed of 25 neurons simulated for 8000 bins (200 bins shown). Neurons are modeled as Poissonian processes with random mean rate between 1 and 5 spikes/bin, uniformly distributed across the neurons. In addition, each neuron is set to fire at  $6 \times$  its mean rate at 0.5% of the bins randomly chosen (referred to as activation bins). In order to simulate cell assemblies, we set all activation bins to be independent, except for two groups of neurons which have simultaneous activation bins. (B) Autocorrelation matrix (ACM). (C) Theoretical eigenvalues distribution for independent neuronal activity (top), and the eigenvalues histogram computed from the simulated network (bottom). Note that 2 eigenvalues fall above the theoretical upper limit predicted for random activity, which correspond to the two cell assemblies present in the network. Notice further that three other eigenvalues fall below the lower limit; the number of eigenvalues outside the theoretical limits is therefore 5, which corresponds to the number of neurons participating in cell assemblies. (D) ACM eigenvectors associated with the two eigenvalues above the theoretical limit for random activity. These vectors are referred to as principal components (PCs). (E) Neuronal representations in the subspace spanned by the PCs (referred to as the Assembly Space). Since the PCs are the vectors which best describe strong correlated activity, neurons with larger projections on the Assembly Space are the neurons involved in cell assemblies (the label of these neurons are also shown). (F) Interaction Matrix; the entries of this matrix are measures of correlated activity of cell assembly neurons in the Assembly Space. Higher values denote neuron pairs pertaining to the same cell assembly, whereas lower values denote neurons whose activity is orthogonal. (G) From the Interaction Matrix, a simple clustering algorithm (described in Supplementary Information files) identifies the neurons of each cell assembly. (H) Same binned spiking activity as in A but rearranged in order to show cell assembly neurons on top, as labeled. (I,J) Assembly Vectors are defined as mean vectors in the Assembly Space (I); these vectors

are used to compute projector operators (**J**). (**K**) The projector operators are then applied to the binned spiking activity, revealing the time course of the activation strength of each cell assembly. Note that these results corroborate the activations seen by visual inspection of **H**. Since the cell assemblies were non-overlapping in this example, the identity of cell assembly neurons can be directly inferred by a simple analysis of the PCs (represented by the dashed line from **D** to **H**). However, such straight inference cannot be performed in cases where one or more neurons pertain to two or more assemblies (see Figure 7).

doi:10.1371/journal.pone.0020996.g006

simulating assembly activations; non-assembly neurons had peak firing at independent (randomly chosen) bins.

Figure 6A shows a 200-bin interval of the simulated network; the associated autocorrelation matrix is shown in Figure 6B. Two eigenvalues of this matrix fall above the upper theoretical limit, whereas three eigenvalues lie below the lower bound (Figure 6C). This analysis therefore indicates that two assemblies and a total of five assembly neurons are present in the network, consistent with predefined simulation parameters.

Since eigenvalues above statistical threshold represent ensemble activity, we use the PCs associated with them (Figure 6D) to search for the identity of assembly neurons. The autocorrelation matrix can be seen as 25 vectors in a 25-dimensional space. In this case, PCA roughly means that the detected assembly activity is better described by the subspace spanned by the PCs; in the present work, we refer to this subspace as “Assembly space”. Removing the non-principal components of our analysis is equivalent to filtering the autocorrelation matrix in order to unravel assembly activity.

Figure 6E shows the neuron vectors on the Assembly space, which are obtained straight from the PC entries (see Methods). Note that some neurons present large vector length in this space, indicating that their spike activity is related to the detected assemblies. In fact, the five neurons with large vector length in the Assembly space (labeled in Figure 6E) correspond to the five units participating in assembly activity. Notice further that there are two clusters of neuron vectors in the Assembly space; these clusters are roughly orthogonal to each other, indicating independent activity. Indeed, notice that neurons orthogonal to each other pertain to different assemblies. Thus, we computed the length of the projection of each neuron vector onto the direction of the others and expressed these results in an “Interaction Matrix” (Figure 6F; see Methods). From the Interaction matrix, we used a simple clustering algorithm in order to determine which neurons were in each assembly (Figure 6G). Although the identification of assembly neurons was straightforward in this example from the visual inspection of Figure 6F, we noted that this was not always the case, making the use of a robust algorithm necessary (see Methods and Figures S1 and S2 for details about the algorithm). Figure 6H shows the same binned spike activity as in Figure 6A but with rows reordered with respect to the identified assemblies. Note that neurons within an assembly have firing peaks at the same bins.

The use of PCs was previously proposed in order to create projectors for computing ensemble activity with a single bin resolution [31,32,34,35]. An activity projector can be defined as the outer product of a PC with itself ([34]; see Methods for details). Since each PC represents an activity pattern, it is possible to compute the instantaneous strength of this pattern by multiplying the z-scored binned spike activity with the projector derived from the PC (see Methods). However, as shown in Figure 2, in some cases this method does not represent individual assemblies. To overcome this limitation, we propose another vector to construct the projectors. This vector, called “assembly vector”, is defined as the mean over all neuron vectors in the Assembly space that exclusively pertain to a given assembly (Figure 6I). Notice that the assembly vector is a linear combination of the PCs (Figure 6I,J), which allows obtaining this vector in the 25-dimensional space. By

using this optimal assembly vector to construct the activity projector, we were then able to obtain the time course of the activity of the corresponding cell assembly. Figure 6K shows the results of such approach. For each assembly, the peaks of the time course matched perfectly the assembly activations seen in Figure 6H.

Note that in this example the PC weights directly reveal the neurons composing each assembly (Figure 6D). For instance, PC1 had higher values in dimensions 5, 15 and 21, which correspond to Cell Assembly 1 neurons; by the same token, the high values of PC2 denote Cell Assembly 2 neurons. Consequently, the estimated assembly optimal vectors in Figure 6I are very similar to the PCs and thus the activity projectors computed from the assembly vectors are virtually the same as the ones calculated from the PCs. As already mentioned (see Figure 2), the previous framework is able to track individual assembly activity when there are no overlapping neurons among the assemblies, as is the case of the example shown in Figure 6; therefore, our modified approach is equivalent to the original in these cases (see Figure S3).

In Figure 7 a more complex example is shown. The network activity was modeled as in Figure 6, but with three assemblies present in the network. Moreover, we simulated overlapping neurons between the assemblies (Assembly 1 neurons: #4, #15, #17, #21; Assembly 2 neurons: #6, #12, #15, #21; Assembly 3 neurons: #9, #21, #25). Figure 7C shows that 3 eigenvalues lie above the upper theoretical limit, denoting the three cell assemblies; moreover, the number of eigenvalues outside the theoretical limits matches the number of cell assembly neurons (8 in this example). Note in Figure 7D that it is no longer possible to identify the assemblies (in terms of which neurons compose them) by a visual inspection of the PC weights. Therefore, the estimation of the time course of assembly activity by computing the projectors from the PCs would be misleading in this case (see Figure S3).

As in the former example, projecting the neuron vectors on the Assembly space reveals the cell assembly neurons (Figure 7E). Note that the assembly neurons are not clearly clustered as in the example shown in Figure 6. While neurons that only pertain to the same assembly still tend to cluster together, neurons that participate in more than one assembly cannot be in two clusters simultaneously. For instance, projected neuron #15 is orthogonal to projected neurons #9 and #25. This is because neuron #15 does not compose the assembly in which neurons #9 and #25 participate. Conversely, neuron vector #15 is not orthogonal to any of the other neuron vectors, since they all participate in at least one assembly together with neuron #15. That is, overlapping neurons still have relatively large degree of collinearity with neurons that compose the same assemblies (Figure 7F). In this sense, since neuron #21 is in all assemblies, it is not orthogonal to any other assembly neuron.

As in the former example, pairwise relations between neurons in Assembly space can be inferred from the Interaction matrix. Notice however that in this case it is not straightforward to identify the cell assemblies by visual inspection of the Interaction Matrix (Figure 7F). Nevertheless, the clustering algorithm we developed (see Methods and Figures S1 and S2) was able to identify the precise composition of each assembly (Figure 7G). As before, after

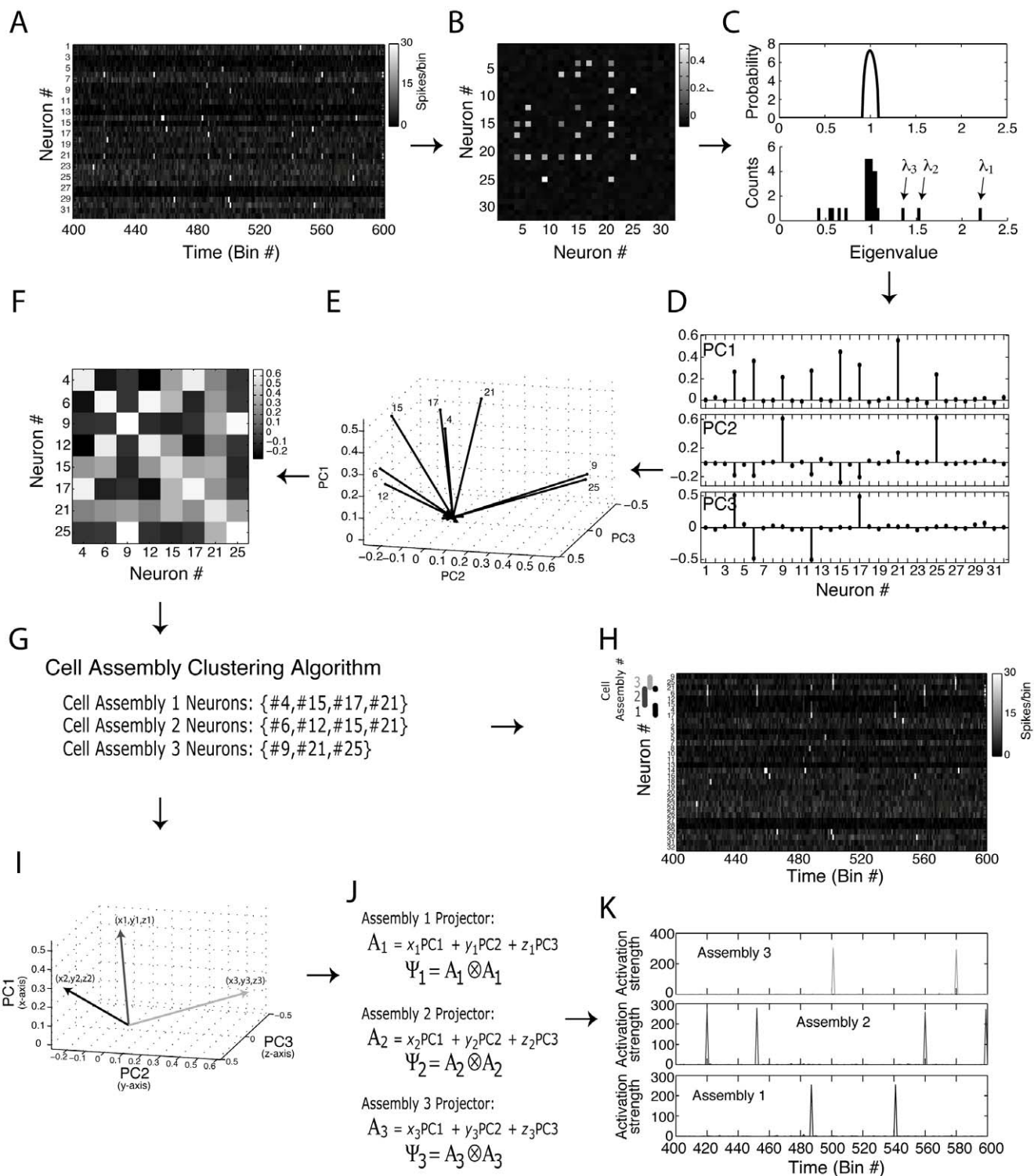


**Figure 7. Identification of cell assemblies with overlapping neurons.** (A–K) Same panels as in Figure 6, but for a network composed of three cell assemblies presenting common neurons. See text for further details.  
doi:10.1371/journal.pone.0020996.g007

identifying the assemblies we computed the optimal assembly vectors (Figure 7I,J) and used them to project the proper time course of assembly activations (Figure 7K; compare with Figure S3). This example therefore shows that the use of assembly vectors instead of PCs is better suited for computing assembly activity.

### Examples of applications to real data

So far we have used simulations to introduce a PCA-based method for cell assembly detection, providing details about how each step worked. In this section we apply the framework to real

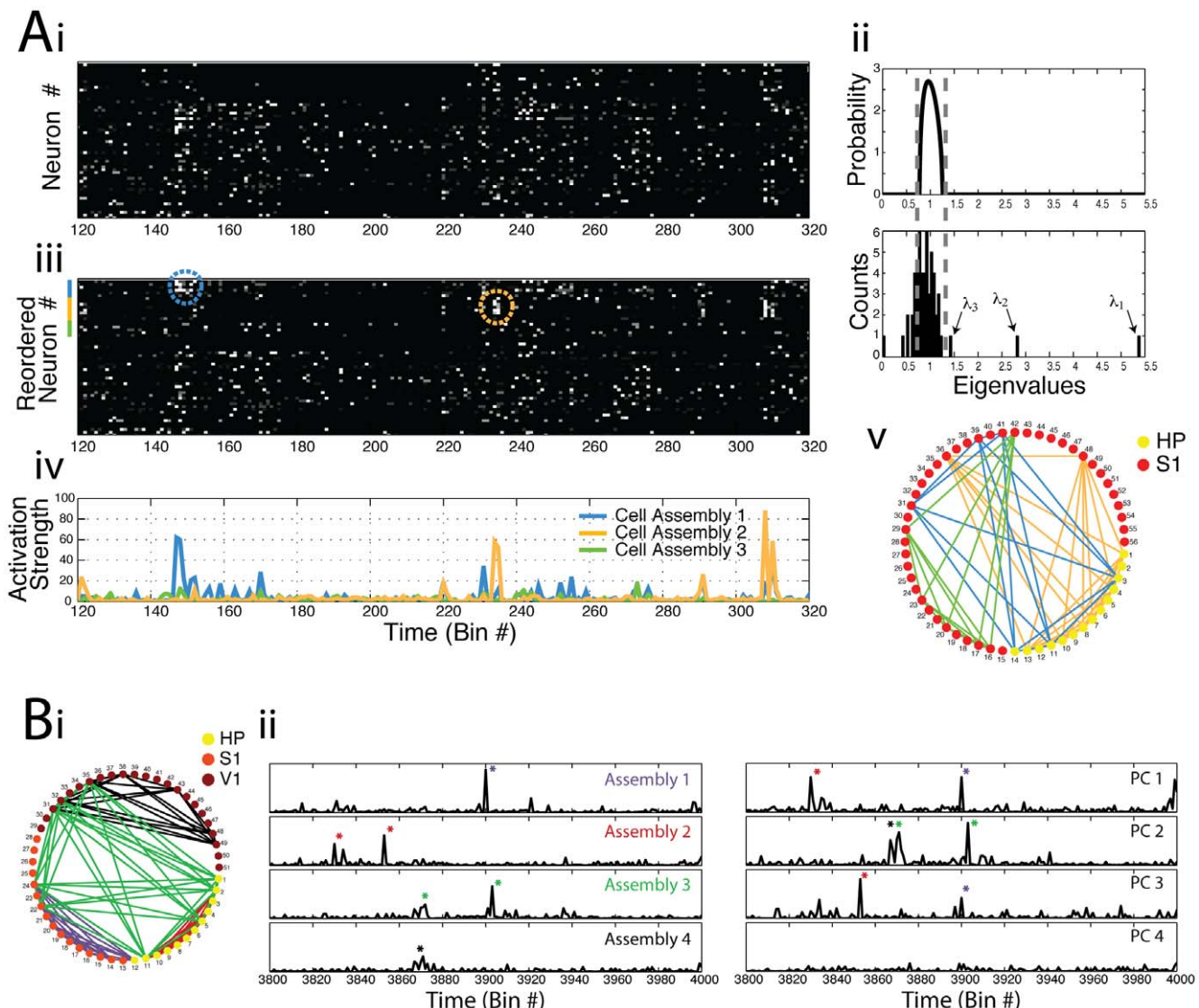


**Figure 8. Example of cell assembly identification using principal components in an experimental data-set.** (A) Ai: Binned spiking activity for 14 hippocampal and 42 S1 neurons obtained from a rat during exploration of a novel object (see Ribeiro et al. [44]). Bin size = 30 ms; total time analyzed: 117.51 s. Aii: Theoretical eigenvalues distribution for independent neuronal activity (top) and the eigenvalues histogram computed from the actual network (bottom) exhibiting 3 eigenvalues above the theoretical upper limit predicted for random activity. Aiii: Same binned spiking activity as above, but with reordered rows such that neurons pertaining to cell assemblies are displayed in the top rows (color bars near the top of the y-axis mark cell assembly neurons; colored dashed circles highlight example periods of assembly activation). Av: Projection analysis yielding the activation time course for the three cell assemblies identified in this network (notice that cell assembly 3 does not activate in the period shown). Av: Graph diagram showing detected cell assemblies (connected neurons). Notice that inter-regional cell assemblies are revealed. (B) Bi: Graph diagram showing four assemblies detected in recordings from S1, V1 and hippocampus (HP) during slow-wave sleep (Bin size = 30 ms; total time analyzed = 124 s). Bii: Time course of ensemble activity as estimated by the original (right) and modified (left) framework.

doi:10.1371/journal.pone.0020996.g008

data and further compare the modifications we propose with the original method.

We analyzed spike activity recorded from rats chronically implanted with multielectrode arrays (see Methods). In the first example (Figure 8A), neuronal activity was obtained from the hippocampus and primary somatosensory cortex (S1) during the exploration of novel objects [44]. In Figure 8Ai, we show a 200-bin period (bin size = 30 ms) of spike activity of this network; Figure 8Aii shows the Marčenko-Pastur distribution along with the empirical eigenvalue distribution computed from the associated autocorrelation matrix. Note the detection of three assemblies in this example. We then applied the framework described above,

and in Figure 8Aiii we plot the reordered spike activity with respect to the assemblies; dashed circles depict two examples of assembly activations occurring in the time period displayed. Figure 8Av shows the time course of activation of the detected assemblies; notice that the activation peaks match the activations seen in Figure 8Aiii. Finally, in Figure 8Av we show all neurons in a circular grid (hippocampal neurons: #1–14; S1 neurons: #15–56) and represent the assemblies by colored lines. Notice that our modified method allows us to infer that two assemblies have neurons in both brain regions.

In the second example (Figure 8B), we analyzed neurons recorded from the hippocampus, S1 and primary visual cortex

(V1) during slow-wave sleep (hippocampal neurons: #1–12; S1 neurons: #13–28; V1 neurons: #29–51). Analysis of the eigenvalues revealed that 4 cell assemblies were present in this network (not shown). We again applied our framework to get to the precise identity of the assembly neurons and depict the four assemblies in Figure 8Bi. Notice in this panel that one assembly was composed by neurons from the three brain areas, whereas three other assemblies were restricted to a single brain region. Notice further in this example that some neurons participate in two assemblies. We then compared the time course of ensemble activity when the PCs were used to build the projectors with projectors derived from assembly optimal vectors. The left and right panels in Figure 8Bii show the activity time course estimated by the assembly vector and by the direct use of the PCs, respectively. Note that the individual assembly activations estimated by the assembly vector approach appear mixed in different PC projections. For instance, the PC1 projection carries mixed activations of Assemblies 1 and 2, whereas PC2 carries information about Assemblies 3 and 4. Based on these results and the simulations presented above, we conclude that the use of assembly vectors to compute the activity time course is well suited for discriminating the activation of individual assemblies, even in the presence of overlapping neurons.

## Discussion

We have presented a mathematical method for the identification of cell assemblies and for computing their activity as a function of time (in units of time bins). The overall algorithm is based on PCA and can be divided in three major steps: **(1)** *Detection of the number of cell assemblies and assembly neurons*; **(2)** *Identification of cell assemblies*; and **(3)** *Computation of assembly activity as a function of time*. The algorithm presented here constitutes an extension of powerful methods introduced previously [31,32,34]. The adaptations and extensions we propose make our framework able to circumvent important limitations present in former methods.

With respect to step 1, Peyrache et al. introduced the use of the Marčenko-Pastur distribution as the null hypothesis to determine the presence of ensemble activity [34]. This is an important achievement in terms of computational cost because most of the previous methods relied on surrogate data analyses to determine statistical significance [26,30,45,46,47,48,49]. Moreover, other methods are only feasible for a small number of neurons [29,30,50,51] or only analyze pairwise correlations [45,52,53], making the analysis of large networks troublesome. The framework presented here inherits the computational advantages of the method envisioned by Peyrache et al. [34]. Additionally, it provides a clear interpretation for the eigenvalues derived from autocorrelation matrices of neuronal spike activity and their relation to the Marčenko-Pastur distribution: we showed that the number of eigenvalues significantly different from the random distribution contain useful information about the number of assemblies and the number of neurons participating in cell assemblies. This constitutes step 2 in our framework, which was not present in previous formulations.

Regarding step 3, the use of PCs in order to construct a time series of ensemble activity had already been introduced by Nicolelis et al. [31,32]. More recently, Peyrache et al. [34] proposed the use of projectors computed from the PC vectors associated with significant eigenvalues to extract *patterns of neural activity* from a defined *template epoch* to be later assessed in a *match epoch*. Peyrache and colleagues used this approach to obtain ensemble activation signatures from spike activity of medial prefrontal cortex (mPfc) neurons during a learning stage (*template*

epoch). Next they used these operators to measure instantaneous similarities (i.e., activations) of mPfc activity during a subsequent slow-wave sleep epoch (*match epoch*). It was found that (re)activations occurred preferentially during sharp wave/ripple complexes in post experience episodes, but not during previous sleep phases [35]. In another recent study, Benchenane et al. [36] reported that Pfc ensemble activations occur preferentially during periods of high theta coherence between the hippocampus and Pfc in a Y-maze task, which tended to occur during the decision point. These remarkable findings demonstrate that the use of PCA to estimate ensemble activity is a powerful tool to study network functioning. However, as illustrated in the present report, the framework applied in previous studies [32,33,35,36] possibly merges the activity of multiple cell assemblies into a single activity pattern. In this sense, the extension of the method now introduced allows for the isolation of the activity patterns of distinct groups of neurons. We believe that sorting out the individual activity of different assemblies will provide important insights in future studies.

While the studies mentioned above have focused on a template matching approach, the results shown in Figure 8 were obtained by first identifying all cell assemblies present in the network and subsequently assessing their activity time course in the same time period used to identify them; notice therefore that the method can be employed in different ways. One should however be cautious to avoid potential spurious results derived from circular analysis [54] when using the template-match approach. For example, it will likely happen that assembly activity during the template epoch (in which the assemblies are defined) is higher than that of any other epoch not used for computing the activity projectors; therefore, we believe one should not make quantitative inferences about assembly activity during the template epoch compared to other epochs.

It is important to emphasize that the PCA-based method is not sensitive to sequences of neuronal activity, such as *synfire chains* [27,55,56]. As pointed in Peyrache et al. [34], the statistical difficulties accompanying methods that look for firing sequences are overwhelming when one needs to analyze larger networks [47,49]. In fact, a common strategy to bypass combinatorial explosion (the number of possible temporal patterns is larger than the number of samples) is to detect ensemble activity disregarding the precise identity of the cell assemblies [57,58,59]. It is also important to note that only a tiny fraction of the neurons in the brain is observable, and therefore synfire chains are likely the effect of underlying sequences of cell assemblies, also known as Hebb's phase sequences [10]. The assessment of assembly sequences can be potentially achieved by the use of our method in combination with methods for detecting sequential activations [26,50,53].

It is also important to consider that the bin size used for the analyses can be critical for the interpretation of the results. As recently noted [12], bin sizes up to 30 ms are potentially well suited to analyze assembly activations. For instance, the typical membrane integration time in the waking cerebral cortex is estimated to vary between 10 and 30 ms [60,61]. Moreover, previous work has shown that neuronal members of a putative cell assembly tend to synchronize transiently in time windows of approximately 25 ms [14,62]. Interestingly, the time window for spike timing dependent plasticity is also consistent with this time-scale [63,64,65]. Finally, this time-scale corresponds to the period of gamma oscillations, which are believed to play a key role in binding representations coded by transiently active cell assemblies [66].

The novel framework described here allows the study of cell assemblies with shared neurons. The importance of this achievement is related to how information is processed and stored in the

brain. Some authors suggest that each neuron would only fire to a specific concept or stimulus (grandmother cells) [67]; therefore, cell assemblies encoding different “things” would not be expected to share neurons. However, a mounting body of work shows that neurons can be very selective (*sparse coding*), but are not grandmother cells [68,69]. The apparent grandmother cells in the human medial temporal lobe [70] may actually respond to between 50 and 150 distinct concepts [71]. Neurons participating in the representation of multiple concepts imply that the processing of information is distributed and occurs through a *multiplexed* code, in which concepts are represented by the activity of partially-overlapping groups of neurons, as postulated by Hebb.

Despite the worldwide acceptance of the cell assembly theory, there is still a paucity of evidence corroborating (or disproving) it. Hebb’s hypotheses not only deal with the formation of assemblies and phase sequences, but also constitute a complete theory describing how learning, fear, hunger, and other complex behaviors emerge from the brain [1]. Most of the difficulty in testing the theory resides in the fact that only a tiny fraction of neurons in the brain can be simultaneously recorded at any given time. However, techniques for massive neuronal recordings are being developed at accelerating rates [22], and while we still lack proper tools for analyzing large quantities of neurons [57,72], much progress is being made to circumvent this limitation. We hope the work presented here constitutes a useful step in this direction.

## Methods

Simulations and data analyses were programmed in MATLAB (The Mathworks, Inc); MATLAB codes for the computation of cell assemblies and their dynamics can be obtained from the authors upon request.

### Analytical formula of the Marčenko-Pastur distribution

The spectrum of eigenvalues of an autocorrelation matrix computed from a random matrix  $\mathbf{M}$  of  $N_{bins}$  columns and  $N_{neurons}$  rows follow the Marčenko-Pastur distribution, which in the limit of  $N_{bins} \rightarrow \infty$  and  $N_{neurons} \rightarrow \infty$ , with  $q = N_{bins}/N_{neurons} \geq 1$  constant, is given by

$$p(\lambda) = \frac{q}{2\pi\sigma^2} \frac{\sqrt{(\lambda_{\max} - \lambda)(\lambda_{\min} - \lambda)}}{\lambda}$$

where  $\sigma$  is the standard deviation of the elements of  $\mathbf{M}$  (in our case, we have  $\sigma = 1$  since we apply the z-score normalization to the binned spike activity);  $\lambda_{\max}$  and  $\lambda_{\min}$  are the upper and lower limits of the Marčenko-Pastur distribution, and they are given by:

$$\lambda_{\min}^{\max} = \sigma^2(1 \pm \sqrt{1/q})^2$$

Notice that  $\lambda_{\max}$  and  $\lambda_{\min}$  converge to 1 when  $q \rightarrow \infty$  and in this limit the theoretical distribution becomes a Dirac delta function at  $\lambda = 1$ . Therefore, the predicted eigenvalues distribution for independent neuronal activity has lower variance when a greater number of time bins are analyzed for a given number of neurons (compare Figure 3A and 3C).

We note that even though the analytical formula for the Marčenko-Pastur distribution was derived in the limit case of large  $N_{bins}$  and  $N_{neurons}$ , this theoretical distribution also approximates the actual distribution in cases of finite matrices, as shown in Plerou et al. [73] and in the present work. Nevertheless, one can

also make use of the bias correction for finite size matrices suggested in [74]. The upper theoretical limit then becomes  $\lambda_{\max} + N_{neurons}^{-2/3}$ . We found however that this correction did not influence the results shown in the present work.

### Outer product and the definition of the activity projector operators

The outer product of two vectors  $\mathbf{u}$  and  $\mathbf{v}$  of length  $N$  is defined as

$$\mathbf{u} \otimes \mathbf{v} = \begin{pmatrix} u_1 v_1 & \dots & u_1 v_N \\ \vdots & \ddots & \vdots \\ u_N v_1 & \dots & u_N v_N \end{pmatrix}$$

The outer product is used to construct the projectors of ensemble activity, as explained in the following. Let  $\mathbf{C}$  be the autocorrelation matrix of a z-scored binned network activity  $\mathbf{Z}$  of dimension  $N_{neurons} \times N_{bins}$ , and let  $\mathbf{p}_i$  ( $i = 1, 2, \dots, N_{neurons}$ ) denote the principal components of  $\mathbf{C}$ . The projector  $\mathbf{P}_i$  associated with  $\mathbf{p}_i$  is given by

$$\mathbf{P}_i = \mathbf{p}_i \otimes \mathbf{p}_i$$

If  $\lambda_i$  is the eigenvalue associated with the principal component  $\mathbf{p}_i$ ,  $\mathbf{C}$  can be decomposed as

$$\mathbf{C} = \lambda_1 \mathbf{P}_1 + \lambda_2 \mathbf{P}_2 + \dots + \lambda_{N_{neurons}} \mathbf{P}_{N_{neurons}} = \sum_{i=1}^{N_{neurons}} \lambda_i \mathbf{P}_i$$

Assuming that each principal component  $\mathbf{p}_i$  represents an ensemble co-activation pattern, the equation above shows that  $\mathbf{C}$  can be represented by a linear combination of the pattern representations encoded in the matrices  $\mathbf{P}_i$ .

### Assembly activity time-course

Peyrache et al. [34] has recently proposed the use of the principal components associated with significant eigenvalues for assessing ensemble activity with a single-bin resolution. The idea is to calculate the instantaneous similarity of the binned spike activity and the ensemble activity pattern as a function of time.

Let  $\mathbf{P}$  be outer product of a significant principal component with itself and  $\mathbf{Z}(b)$  be the  $b$ -th column of the z-scored binned spike activity (in other words, the number of spikes of all neurons in the  $b$ -th bin). The measure of instantaneous similarity of  $\mathbf{P}$  and  $\mathbf{Z}$  as a function of time is given by

$$R(b) = \mathbf{Z}(b)^T \mathbf{P} \mathbf{Z}(b)$$

This equation can be rewritten as

$$R(b) = \sum_{i,j} Z_{ib} P_{ij} Z_{jb}$$

where  $Z_{ib}$  is the normalized firing rate of neuron  $i$  in bin  $b$ , and  $P_{ij}$  is the entry in the  $i$ -th row and  $j$ -th column of  $\mathbf{P}$ . Note that when  $i=j$ , the corresponding term of the summation only takes into account the activity of a single neuron  $i$ . Since our goal is to measure ensemble activity more than single neuron activations, this term can be set to zero and the equation reduces to

$$R(b) = \sum_{i,j, i \neq j} Z_{ib} P_{ij} Z_{jb}$$

which is the equation for computing the time course of ensemble activity used in Peyrache et al. [34].

As we show in the present work (Figure 2 and S3), projectors computed as above are not appropriate to track the activity time course of individual cell assemblies if there are overlapping neurons among assemblies. To overcome this problem, we propose constructing the projectors using the optimal assembly vectors in Assembly space (Figures 6 and 7). This is achieved as follows: The Assembly space is defined as the metric subspace spanned by the principal components  $\mathbf{p}_i$  associated with eigenvalues  $\lambda_i$  that are significantly above chance. Let  $\mathbf{a}_k$  ( $k = 1, \dots, N_{\text{neurons}}$ ) denote the neuron vectors in the Assembly space; each  $\mathbf{a}_k$  is given by (see Figure 6E):

$$\mathbf{a}_k = (\mathbf{p}_1(k), \mathbf{p}_2(k), \dots, \mathbf{p}_n(k))$$

where  $n$  is the number of significant eigenvalues. As we show in the present work, the number of eigenvalues outside the theoretical distribution gives the total number of neurons participating in cell assemblies. Supposing there are  $N_{\text{Cneurons}}$  assembly neurons, they correspond to the  $N_{\text{Cneurons}}$  vectors with largest norm (vector length) in Assembly space (Figures 6E and 7E). Then, the projections of each neuron vector in the Assembly space onto the direction of the other vectors are computed and used to build the Interaction Matrix (Figures 6F and 7F). That is, given two neuron vectors  $\mathbf{a}_i$  and  $\mathbf{a}_j$ , the corresponding  $(i,j)$  entry of the Interaction Matrix is given by  $(\mathbf{a}_i \cdot \mathbf{a}_j) / (\|\mathbf{a}_i\| \|\mathbf{a}_j\|)$ . From the Interaction Matrix, it is possible to determine which neurons compose each assembly by means of a clustering algorithm (see next section). The estimated optimal assembly vector  $\bar{\mathbf{a}}$  is then defined for an assembly A as the mean over  $\mathbf{a}_i$ 's for all neurons  $i$  exclusive to A, normalized to have unitary norm:

$$\bar{\mathbf{a}} = \frac{\sum_i \mathbf{a}_i}{\|\sum_i \mathbf{a}_i\|}$$

Next,  $\bar{\mathbf{a}}$  is expressed as a linear combination of the significant principal components:

$$\alpha = \sum_{i=1}^n (\bar{\mathbf{a}} \cdot \mathbf{p}_i) \mathbf{p}_i$$

A projector  $\Psi$  is then calculated as the outer product of  $\alpha$  with itself ( $\Psi = \alpha \otimes \alpha$ ). Finally, we use  $\Psi$  to compute the activity time course of assembly A as follows:

$$R_A(b) = \sum_{i,j, i \neq j} Z_{ib} \Psi_{ij} Z_{jb}$$

### Binary Interaction Matrix and clustering algorithm

The algorithm identifies the neurons pertaining to each cell assembly based on the analysis of the Interaction Matrix. The entries of the Interaction Matrix are a measure of correlation between two neuron vectors in Assembly space (taking into account only cell assembly neurons). As we have shown in Figures 6 and 7, neurons that pertain to different assemblies are orthogonal to each other, while high collinearity levels indicate that neurons are correlated in the Assembly space. Therefore, it is expected that the distribution of Interaction Matrix entries is bimodal, having sets of low and high values (see Figure S1). We then apply a uni-dimensional version of the K-means clustering algorithm [75] in order to find a threshold that best separate these groups. We use this threshold to create a binary Interaction

Matrix; that is, we transform all matrix values in 0's (values below a threshold) and 1's (values above the threshold). This binary matrix is the input to the clustering algorithm which is then able to sort apart the neurons of different assemblies. In Figure S1 we provide an overview of the thresholding procedure and in Figure S2 we describe the clustering algorithm.

### Electrophysiological recordings

Male Long-Evans rats were chronically implanted with tungsten microelectrode arrays aimed at the hippocampus, primary visual cortex and primary somatosensory cortex. Data recorded from these animals were described in a previous study [44], in which a detailed description of surgery, data collection, behavior and histology can be found.

### Supporting Information

**Figure S1** Interaction Matrix thresholding. **(A)** Ai: Interaction Matrix of the example shown in Figure 7. Aii: Histogram of the entries of the Interaction Matrix shown in Ai. Dashed red line indicates the threshold found by a K-means algorithm. The threshold is the mean between the borders of the clusters. Aiii: Binary Interaction Matrix. Values lower and higher than the threshold are set to 0 and 1, respectively. This matrix is later used as input to the clustering algorithm described in Figure S2. **(B)** Same as **(A)** but for the real data shown in Figure 8B. Note that the threshold found separates the bimodal distribution. (TIF)

**Figure S2** Description of the assembly clustering algorithm. **(A,B)** Flux diagram representing the three main steps of the algorithm **(A)** and an example using simulated data of nine neurons **(B)**. The algorithm receives as input a Binary Interaction Matrix (BIM; depicted in **B** top panel), which is obtained by thresholding the Interaction Matrix (see Figure S1), and provides as output the assembly label(s) for each neuron **(B** bottom panel). Step 1 involves re-organizing the BIM according to the number of interactions in each row and also removing repeated rows; we denote the resulting matrix as the OBIM **(B** second panel from top). Notice in **B** that row #8 does not appear in the OBIM since it was equal to row #5. In Step 2 assembly labels are created and assigned to the neurons. This is achieved based on sequentially examining each row of OBIM and identifying for each neuron (row) all other neurons that interact with it; a common assembly label is ascribed to all interacting neurons. New assembly labels are created whenever the neuron (row) being processed has not been previously assigned to any of the existing assembly labels. This step generates the Assembly Label Matrix (ALM), which entry  $(i,j)$  informs the assemblies shared by neurons  $\#i$  and  $\#j$ . Notice that neuron #8 automatically appears in ALM under this procedure **(B** third panel from top). Finally, in Step 3 the assembly labels in the diagonal of ALM are extracted; they indicate the assemblies in which each neuron participates. (TIF)

**Figure S3** Estimation of time course of cell assembly activity based on individual PCs for the examples shown in Figures 6 **(A)** and 7 **(B)**. The estimation of assembly activity based on assembly vectors is also reproduced from Figures 6 and 7 for comparison. (TIF)

### Author Contributions

Conceived and designed the experiments: ABLT. Performed the experiments: VL-d-S SC-O. Analyzed the data: VL-d-S SC-O ABLT STR MALN. Wrote the paper: ABLT VL-d-S STR.

## References

- Hebb DO (1949) *The Organization of Behavior*. New York: John Wiley & Sons.
- Wang Q, Chen G, Perc M (2011) Synchronous bursts on scale-free neuronal networks with attractive and repulsive coupling. *PLoS One* 6: e15851.
- Wang Q, Perc M, Duan Z, Chen G (2009) Synchronization transitions on scale-free neuronal networks due to finite information transmission delays. *Phys Rev E Stat Nonlin Soft Matter Phys* 80: 026206.
- Pikovsky A, Rosenblum M, Kurths J (2001) *Synchronization, A Universal Concept in Nonlinear Sciences* Cambridge University Press.
- Singer W (1993) Synchronization of cortical activity and its putative role in information processing and learning. *Annu Rev Physiol* 55: 349–374.
- Freiwald WA, Kreiter AK, Singer W (2001) Synchronization and assembly formation in the visual cortex. *Prog Brain Res* 130: 111–140.
- Volman V, Perc M (2010) Fast random rewiring and strong connectivity impair subthreshold signal detection in excitable networks. *New J Phys* 12.
- Mari D (1971) Simple memory: a theory for archicortex. *Philos Trans R Soc Lond B Biol Sci* 262: 23–81.
- Wallenstein GV, Eichenbaum H, Hasselmo ME (1998) The hippocampus as an associator of discontiguous events. *Trends Neurosci* 21: 317–323.
- Harris KD (2005) Neural signatures of cell assembly organization. *Nature Reviews Neuroscience* 6: 399–407.
- Pastalkova E, Itskov V, Amarasingham A, Buzsaki G (2008) Internally generated cell assembly sequences in the rat hippocampus. *Science* 321: 1322–1327.
- Buzsaki G (2010) Neural syntax: cell assemblies, synapsembles, and readers. *Neuron* 68: 362–385.
- Wilson MA, McNaughton BL (1993) Dynamics of the hippocampal ensemble code for space. *Science* 261: 1055–1058.
- Harris KD, Csicsvari J, Hirase H, Dragoi G, Buzsaki G (2003) Organization of cell assemblies in the hippocampus. *Nature* 424: 552–556.
- Carmena JM, Lebedev MA, Crist RE, O'Doherty JE, Santucci DM, et al. (2003) Learning to control a brain-machine interface for reaching and grasping by primates. *Plos Biology* 1: 193–208.
- Hung CP, Kreiman G, Poggio T, DiCarlo JJ (2005) Fast readout of object identity from macaque inferior temporal cortex. *Science* 310: 863–866.
- Nicolelis MA, Ghazanfar AA, Stambaugh CR, Oliveira LM, Laubach M, et al. (1998) Simultaneous encoding of tactile information by three primate cortical areas. *Nat Neurosci* 1: 621–630.
- Wessberg J, Stambaugh CR, Kralik JD, Beck PD, Laubach M, et al. (2000) Real-time prediction of hand trajectory by ensembles of cortical neurons in primates. *Nature* 408: 361–365.
- Nicolelis MA, Fanselow EE, Ghazanfar AA (1997) Hebb's dream: the resurgence of cell assemblies. *Neuron* 19: 219–221.
- Nicolelis MAL, De Schutter E (1999) Methods for recording and analyzing neuronal ensemble activity. *Journal of Neuroscience Methods* 94: 3–4.
- Buzsaki G (2004) Large-scale recording of neuronal ensembles. *Nature Neuroscience* 7: 446–451.
- Stevenson IH, Kording KP (2011) How advances in neural recording affect data analysis. *Nat Neurosci* 14: 139–142.
- Lee AK, Wilson MA (2002) Memory of sequential experience in the hippocampus during slow wave sleep. *Neuron* 36: 1183–1194.
- Ribeiro S, Gervasoni D, Soares ES, Zhou Y, Lin SC, et al. (2004) Long-lasting novelty-induced neuronal reverberation during slow-wave sleep in multiple forebrain areas. *Plos Biology* 2: 126–137.
- Louie K, Wilson MA (2001) Temporally structured replay of awake hippocampal ensemble activity during rapid eye movement sleep. *Neuron* 29: 145–156.
- Abeles M, Gat I (2001) Detecting precise firing sequences in experimental data. *Journal of Neuroscience Methods* 107: 141–154.
- Ikegaya Y, Aaron G, Cossart R, Aronov D, Lampl I, et al. (2004) Synfire chains and cortical songs: Temporal modules of cortical activity. *Science* 304: 559–564.
- Maldonado P, Babul C, Singer W, Rodriguez E, Berger D, et al. (2008) Synchronization of neuronal responses in primary visual cortex of monkeys viewing natural images. *J Neurophysiol* 100: 1523–1532.
- Grun S, Diesmann M, Aertsen A (2002) Unitary events in multiple single-neuron spiking activity: 1. Detection and significance. *Neural Computation* 14: 43–80.
- Pipa G, Wheeler DW, Singer W, Nikolic D (2008) NeuroXidence: reliable and efficient analysis of an excess or deficiency of joint-spike events. *Journal of Computational Neuroscience* 25: 64–88.
- Chapin JK, Nicolelis MA (1999) Principal component analysis of neuronal ensemble activity reveals multidimensional somatosensory representations. *J Neurosci Methods* 94: 121–140.
- Nicolelis MAL, Baccala LA, Lin RCS, Chapin JK (1995) Sensorimotor encoding by synchronous neural ensemble activity at multiple levels of the somatosensory system. *Science* 268: 1353–1358.
- Humphries MD (2011) Spike-train communities: finding groups of similar spike trains. *J Neurosci* 31: 2321–2336.
- Peyrache A, Benchenane K, Khamassi M, Wiener SI, Battaglia FP (2010) Principal component analysis of ensemble recordings reveals cell assemblies at high temporal resolution. *Journal of Computational Neuroscience* 29: 309–325.
- Peyrache A, Khamassi M, Benchenane K, Wiener SI, Battaglia FP (2009) Replay of rule-learning related neural patterns in the prefrontal cortex during sleep. *Nature Neuroscience* 12: 919–U143.
- Benchenane K, Peyrache A, Khamassi M, Tierney PL, Gioanni Y, et al. (2010) Coherent Theta Oscillations and Reorganization of Spike Timing in the Hippocampal-Prefrontal Network upon Learning. *Neuron* 66: 921–936.
- Theiler J, Eubank S, Longtin A, Galdrikian B, Doyne Farmer J (1992) Testing for nonlinearity in time series: the method of surrogate data. *Physica D: Nonlinear Phenomena* 58: 77–94.
- Schreiber T, Schmitz A (1996) Improved Surrogate Data for Nonlinearity Tests. *Physical Review Letters* 77: 635.
- Perc M, Green AK, Dixon CJ, Marhl M (2008) Establishing the stochastic nature of intracellular calcium oscillations from experimental data. *Biophys Chem* 132: 33–38.
- Pradhan N, Sadasivan PK (1996) Relevance of surrogate-data testing in electroencephalogram analysis. *Phys Rev E Stat Phys Plasmas Fluids Relat Interdiscip Topics* 53: 2684–2692.
- Khoa TQD, Thang HM, Nakagawa M (2008) Testing for Nonlinearity in Functional Near-Infrared Spectroscopy of Brain Activities by Surrogate Data Methods. *The Journal of Physiological Sciences* 58: 47–52.
- Schreiber T (1999) Interdisciplinary application of nonlinear time series methods. *Physics Reports* 308: 1–64.
- Marčenko VA, Pastur LA (1967) Distribution of eigenvalues for some sets of random matrices. *Mathematics of the USSR-Sbornik* 1: 457–483.
- Ribeiro S, Shi X, Engelhard M, Zhou Y, Zhang H, et al. (2007) Novel experience induces persistent sleep-dependent plasticity in the cortex but not in the hippocampus. *Front Neurosci* 1: 43–55.
- Schniedman E, Berry MJ, Segev R, Bialek W (2006) Weak pairwise correlations imply strongly correlated network states in a neural population. *Nature* 440: 1007–1012.
- Berger D, Warren D, Normann R, Arieli A, Grun S (2007) Spatially organized spike correlation in cat visual cortex. *Neurocomputing* 70: 2112–2116.
- Mokeichev A, Okun M, Barak O, Katz Y, Ben-Shahar O, et al. (2007) Stochastic emergence of repeating cortical motifs in spontaneous membrane potential fluctuations in vivo. *Neuron* 53: 413–425.
- Berger D, Borgelt C, Louis S, Morrison A, Grun S (2010) Efficient identification of assembly neurons within massively parallel spike trains. *Comput Intell Neurosci*: 439648.
- Grun S (2009) Data-Driven Significance Estimation for Precise Spike Correlation. *Journal of Neurophysiology* 101: 1126–1140.
- Tetko IV, Villa AEP (2001) A pattern grouping algorithm for analysis of spatiotemporal patterns in neuronal spike trains. 1. Detection of repeated patterns. *Journal of Neuroscience Methods* 105: 1–14.
- Abeles M, Gerstein GL (1988) Detecting spatiotemporal firing patterns among simultaneously recorded single neurons. *Journal of Neurophysiology* 60: 909–924.
- Wilson MA, McNaughton BL (1994) Reactivation of hippocampal ensemble memories during sleep. *Science* 265: 676–679.
- Shmuel T, Drori R, Shmuel O, Ben-Shaul Y, Nadasdy Z, et al. (2006) Temporally precise cortical firing patterns are associated with distinct action segments. *Journal of Neurophysiology* 96: 2645–2652.
- Kriegeskorte N, Simmons WK, Bellgowan PSF, Baker CI (2009) Circular analysis in systems neuroscience: the dangers of double dipping. *Nature Neuroscience* 12: 535–540.
- Prut Y, Vaadia E, Bergman H, Haalman I, Slovin H, et al. (1998) Spatiotemporal structure of cortical activity: Properties and behavioral relevance. *Journal of Neurophysiology* 79: 2857–2874.
- Abeles M (1991) *Corticonics: Neural Circuits of the Cerebral Cortex*: Cambridge University Press, New-York.
- Louis S, Borgelt C, Grun S (2010) Complexity distribution as a measure for assembly size and temporal precision. *Neural Networks* 23: 705–712.
- Staudt B, Rotter S, Grun S (2010) CuBIC: cumulant based inference of higher-order correlations in massively parallel spike trains. *Journal of Computational Neuroscience* 29: 327–350.
- Staudt B, Grun S, Rotter S (2010) Higher-order correlations in non-stationary parallel spike trains: statistical modeling and inference. *Frontiers in Computational Neuroscience* 4.
- Koch C, Rapp M, Segev I (1996) A brief history of time (constants). *Cerebral Cortex* 6: 93–101.
- Leger JF, Stern EA, Aertsen A, Heck D (2005) Synaptic integration in rat frontal cortex shaped by network activity. *Journal of Neurophysiology* 93: 281–293.
- Kelemen E, Fenton AA (2010) Dynamic Grouping of Hippocampal Neural Activity During Cognitive Control of Two Spatial Frames. *Plos Biology* 8.
- Bi GQ, Poo MM (1998) Synaptic modifications in cultured hippocampal neurons: Dependence on spike timing, synaptic strength, and postsynaptic cell type. *Journal of Neuroscience* 18: 10464–10472.
- Markram H, Lubke J, Frotscher M, Sakmann B (1997) Regulation of synaptic efficacy by coincidence of postsynaptic APs and EPSPs. *Science* 275: 213–215.
- Levy WB, Steward O (1983) Temporal contiguity requirements for long-term associative potentiation depression in the hippocampus. *Neuroscience* 8: 791–797.
- Fries P, Nikolic D, Singer W (2007) The gamma cycle. *Trends Neurosci* 30: 309–316.

67. Bowers JS (2009) On the biological plausibility of grandmother cells: implications for neural network theories in psychology and neuroscience. *Psychol Rev* 116: 220–251.
68. Quiroga RQ, Kreiman G, Koch C, Fried I (2008) Sparse but not ‘Grandmother-cell’ coding in the medial temporal lobe. *Trends in Cognitive Sciences* 12: 87–91.
69. Gelbard-Sagiv H, Mukamel R, Harel M, Malach R, Fried I (2008) Internally generated reactivation of single neurons in human hippocampus during free recall. *Science* 322: 96–101.
70. Quiroga RQ, Reddy L, Kreiman G, Koch C, Fried I (2005) Invariant visual representation by single neurons in the human brain. *Nature* 435: 1102–1107.
71. Waydo S, Kraskov A, Quiroga RQ, Fried I, Koch C (2006) Sparse representation in the human medial temporal lobe. *Journal of Neuroscience* 26: 10232–10234.
72. Brown EN, Kass RE, Mitra PP (2004) Multiple neural spike train data analysis: state-of-the-art and future challenges. *Nature Neuroscience* 7: 456–461.
73. Plerou V, Gopikrishnan P, Rosenow B, Amaral LAN, Guhr T, et al. (2002) Random matrix approach to cross correlations in financial data. *Physical Review E* 65: 066126.
74. Tracy CA, Widom H (1994) Level-spacing distributions and the airy kernel. *Communications in Mathematical Physics* 159: 151–174.
75. Lloyd SP (1982) Least-squares quantizatoin in PCM. *Ieee Transactions on Information Theory* 28: 129–137.